Structural and Functional Studies of $G\alpha_q$ Signaling and Regulation

by

Veronica G. Taylor

A dissertation submitted in partial fulfillment
of the requirements for the degree of
Doctor of Philosophy
(Biophysics)
in the University of Michigan
2016

Doctoral Committee:

Professor John J.G. Tesmer, Chair
Assistant Professor Tomasz Cierpicki
Professor Janet L. Smith
Professor John R. Traynor

Dedication

To my family. I would not have come this far without your generosity, support and help.

Acknowledgements

I would like to thank all the people I have worked with in the lab throughout the years. They have been a great team and an invaluable part of my graduate school experience. In particular, I would like to thank Dr. Alisa Glukhova for the many years we worked together in the lab. Your enthusiasm for science was infectious. I would also like to thank Dr. Jennifer Cash for all the advice and discussions. You will make an excellent PI someday.

I am thankful to my mentor, Dr. John Tesmer, for allowing me to do research in his lab these many years. I have learned a great deal about science throughout my degree. I would also like to acknowledge my doctoral committee for their input and suggestions during our meetings.

Additionally, I would like to thank my collaborators. Dr. Tomasz Cierpicki assisted with the NMR, as well as Dr. George Lund and Dr. Felicia Gray of Dr. Cierpicki's lab. Sarah Graham of Dr. Heather Carlson's lab performed all the molecular dynamics simulations. Dr. Elena Kondrashkina assisted in performing the SAXS data collection and analysis. I would also like to acknowledge the staff at LS-CAT and DND-CAT at the Advanced Photon Source for their assistance in x-ray and SAXS data collection.

Table of Contents

DEDICATION	ii
ACKNOWLEDGEMENTS	iii
LIST OF FIGURES	v
LIST OF TABLES	vi
LIST OF APPENDICES	vii
LIST OF ABBREVIATIONS	viii
ABSTRACT	ix
CHAPTER	
1. Introduction	**1**
2. Structure of the Regulator of G Protein Signaling 8 (RGS8)-Gα_q Complex	**10**
Introduction	10
Methods	16
Results	24
Conclusions	28
3. Structure and Function of the Gα_q Effector p63RhoGEF	**32**
Introduction	32
Methods	39
Results	51
Conclusions	64
4. Conclusion	**69**
APPENDICES	74
REFERENCES	84

List of Figures

Figure 1.1 The GTPase cycle 2
Figure 1.2 Small GTPases and G proteins share structural features 3
Figure 1.3 $G\alpha_q$ signaling through p63RhoGEF and inactivation by RGS proteins 8
Figure 2.1 Domain structure of the R4, R7, R12 and RZ subfamilies of RGS proteins 11
Figure 2.2 Selectivity of RGS family members for $G\alpha_{i/o}$ or $G\alpha_{q/11}$ subunits 13
Figure 2.3 Structure of the RGS domain 14
Figure 2.4 Purification of His-tagged RGS8 17
Figure 2.5 Purification of His-tagged RGS10 18
Figure 2.6 Isolation of RGS8- $G\alpha_q$ complex by size exclusion column chromatography 20
Figure 2.7 Structure of RGS8 in complex with $G\alpha_q$ reveals a canonical tilt 23
Figure 2.8 Sequence conservation of RGS8 residues in α6 and α7 suggests selectivity mechanisms 25
Figure 2.9 Structural models of interactions between RGS α7 and the α-helical domain of $G\alpha$ 26
Figure 2.10 Single turnover GAP assays of RGS variants reveal modulation by contacts with the α-helical domain 27
Figure 3.1 Dbl RhoGEFs 33
Figure 3.2 Crystal structure of the RhoA–p63RhoGEF–$G\alpha_q$ complex (2RGN) 35
Figure 3.3 Variability in the α6-αN linker among Dbl family RhoGEFs 36
Figure 3.4 Purification of the DH domain of p63RhoGEF 41
Figure 3.5 Purification of the PH domain of p63RhoGEF 43
Figure 3.6 Purification of the DH/PH domain of p63RhoGEF 44
Figure 3.7 Formation of the DH-RhoA complex 47
Figure 3.8 SAXS scattering curve analysis 52
Figure 3.9 Molecular dynamics angle frequency histogram 56
Figure 3.10 HSQC spectrum of the PH domain (residues 334-470) 57
Figure 3.11 Spectra of DH domain (residues 149-338) 58
Figure 3.12 Electrospray ionization mass spectrometry deconvoluted mass 59
Figure 3.13 TROSY spectrum of the DH/PH tandem 60
Figure 3.14 ^{13}C chemical shift variation between assigned PH and DH/PH peaks 61
Figure 3.15 Measurement and calculation of residual dipolar coupling values 62
Figure C.1 Competitive binding assay using $palm^-$ p63RhoGEF variants 82
Figure C.2 Direct binding between $G\alpha_q$ and p63RhoGEF variants 83

List of Tables

Table 2.1 Crystallographic and refinement statistics for the RGS8-Gα_q complex 22
Table 2.2 Single turnover GTPase assays using RGS8 and RGS10 variants 28
Table 3.1 Constructs of p63RhoGEF variants for bacterial and insect cell expression 40
Table 3.2 Analysis of SAXS scattering curves 54
Table 3.3 Comparison of theoretical scattering curves 55
Table 3.4 RDC measurements for the DH/PH domain 64
Table A.1 Chemical shifts of assigned residues for the HSQC experiment of the PH domain of p63RhoGEF (residues 338-470) 74
Table B.1 Chemical shifts of assigned residues for the HSQC-TROSY experiment of p63RhoGEF (residues 149-470) 77

List of Appendices

Appendix A Assignments of the PH domain of p63RhoGEF (residues 338-470) 74
Appendix B Assignments of the DH/PH tandem of p63RhoGEF (residues 149-470) 77
Appendix C The N-terminus of p63RhoGEF in $G\alpha_q$ Binding 81

List of Abbreviations

APS - Advanced Photon Source
βME - β-mercaptoethanol
Dbs - Dbl's big sister
DEP –Dishevelled, Egl-10 and Pleckstrin
DH - Dbl homology
DTT - dithioreitol
EDTA - ethylenediaminetetraacetic acid
ESI - electrospray ionization
GAP - GTPase accelerating protein
GDP - Guanosine diphosphate
GEF - Guanine nucleotide exchange factor
GGL - G protein gamma-like
GPCR - G protein-coupled receptor
GRK - G protein-coupled receptor kinase
GTP - Guanosine-5'-triphosphate
HSQC - heteronuclear single quantum coherence spectroscopy
Ig - immunoglobulin
MD - molecular dynamics
NMR - nuclear magnetic resonance
PMSF - phenylmethane sulfonyl fluoride
PH - pleckstrin homology
RDC - residual dipolar coupling
RGS - regulator of g protein signaling
SAXS - small-angle x-ray scattering
Sw - switch
TCEP - (tris(2-carboxyethyl)phosphine
TROSY - transverse relaxation-optimized spectroscopy
WAXS - wide-angle x-ray scattering

Abstract

Hydrolysis of bound GTP to GDP inactivates a G protein. Regulator of G protein signaling (RGS) proteins interact with heterotrimeric G protein α subunits to increase this hydrolysis rate. The R4 subfamily of RGS proteins generally accepts both $G\alpha_{i/o}$ and $G\alpha_{q/11}$ family subunits as substrates, while the R7 and R12 subfamilies select against $G\alpha_{q/11}$. One RGS protein, RGS2, is known to be selective for $G\alpha_{q/11}$. The molecular basis for this selectivity is not clear. Previously, the crystal structure of the RGS2-$G\alpha_q$ complex revealed a non-canonical interaction due to interfacial differences imposed by RGS2, the Gα subunit, or both. To resolve this ambiguity, the 2.6 Å crystal structure of an R4 subfamily RGS protein, RGS8, was determined in complex with $G\alpha_q$. This structure shows RGS8 and $G\alpha_q$ in a canonical interaction, indicating that the non-canonical interaction of RGS2 with $G\alpha_q$ is due to unique features of RGS2. Based on the RGS8-$G\alpha_q$ structure, residues in RGS8 that contact a unique loop in the α-helical domain of $G\alpha_q$ were converted to residues typically found in R12 subfamily members, and the reverse substitutions were introduced into an R12 subfamily RGS protein. These substitutions perturbed the ability of each RGS to stimulate GTP hydrolysis, but did not reverse selectivity of either. Instead, selectivity for $G\alpha_q$ is likely determined by contacts between α6 of the RGS domain and Switch III of $G\alpha_q$.

RhoA, a key actin cytoskeleton regulator, is activated by GPCRs that couple to $G\alpha_q$. One pathway that links $G\alpha_q$ to RhoA is via p63 Rho guanine nucleotide exchange factor (p63RhoGEF). Although the atomic structure of the $G\alpha_q$-p63RhoGEF-RhoA complex is known, the mechanism of activation is not clear, in part because the structure for the basal conformation of p63RhoGEF has not yet been determined. Work described in this thesis uses nuclear magnetic resonance spectroscopy and small-angle x-ray scattering to determine the solution structure of the p63RhoGEF catalytic core. Successful completion of this work would characterize a $G\alpha_q$ effector in both its basal and activated states, and would reveal the molecular basis for regulation of an important link between heterotrimeric and small molecular weight G proteins.

Chapter 1

Introduction

Cells use signaling cascades to bring about and maintain the complex processes of the body. These cascades involve a chain of messengers and receivers that pass an initial signal along from one protein to the next in order to produce a particular outcome. It is this signaling that allows a cell to respond to its environment. In many cases, the process of extracellular stimuli effecting a response on the inside of the cell follows a similar path; the input signal interacts extracellularly with a membrane spanning protein, which then interacts with a protein on the inside of the cell, thus starting a chain of interacting proteins inside the cell that will eventually lead to the end response. Proteins can signal to multiple other proteins at a time or they can be very selective about which ones they interact with. Furthermore, understanding these signaling interactions at a level that allows for the prediction and mapping of the entire network of interactions produced by any given initial signal would allow for a very deep understanding of cell biology, as well as open the door for manipulation or improvement upon a signaling system by therapeutics.

A recurrent player in signaling networks is a protein known as the GTPase, or "G protein". GTPases act as molecular switches through a circular process of binding and hydrolysis of guanosine triphosphate (GTP) (Fig. 1.1). Binding of GTP alters the GTPase conformation into an active state that is able to carry out signaling. Upon hydrolysis of GTP to GDP, the GTPase reverts to an inactive conformation. By releasing GDP, GTPases can once again bind GTP, and continue the cyclical process that allows for signaling events to quickly be turned on and off within the cell. There are additional proteins that regulate the speed of this cycle. These proteins can accelerate the hydrolysis step, aid in the exchange of GDP for GTP or lock the GTPase in the inactive form(1). The ability of GTPases to essentially work as protein timers makes them useful in diverse processes such as vesicle transport, protein translation and mitosis, in addition to signaling(2-4).

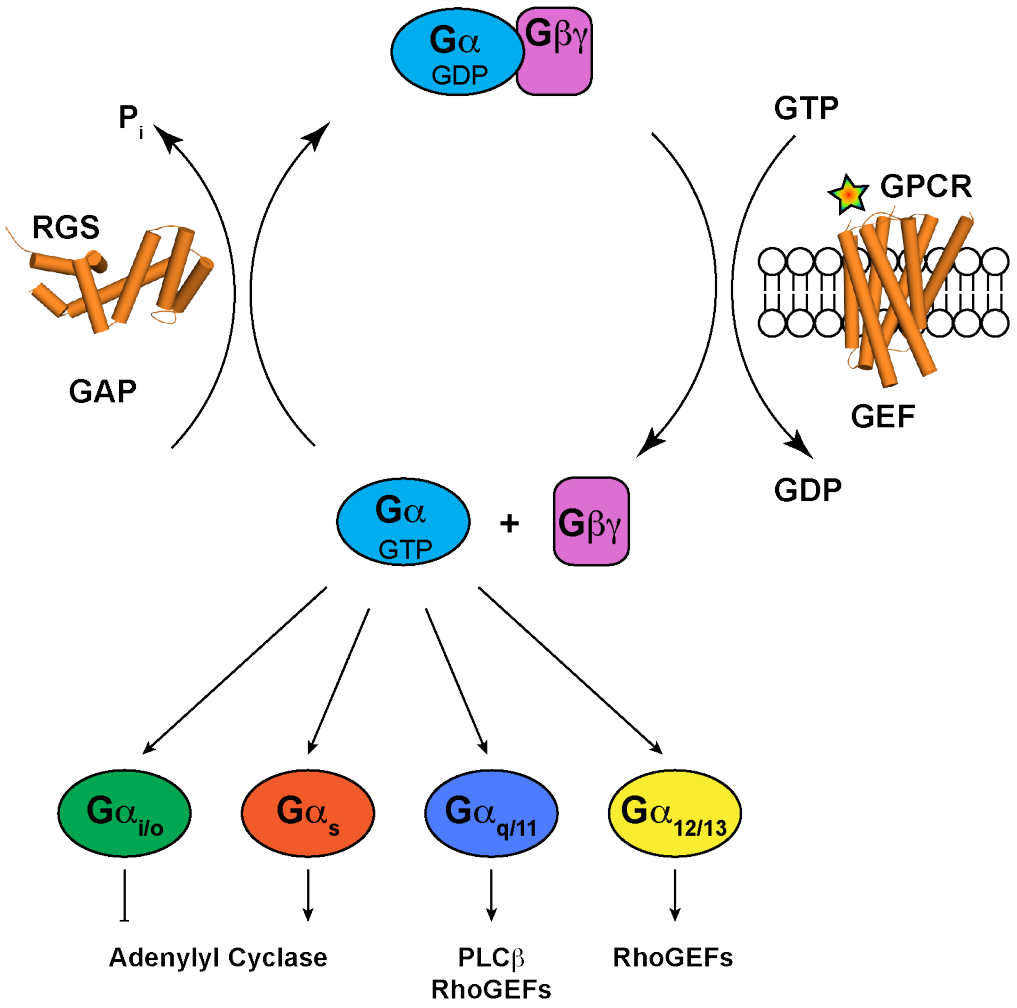

Figure 1.1 The GTPase cycle. G proteins are considered active upon binding of GTP. GPCRs serve as guanine nucleotide exchange factors by exchanging GDP for GTP on the G protein. Gα subunits can then go on to signal through various effectors, such as the canonical ones shown here. RGS proteins serve as GAPs and increase the rate of GTP hydrolysis on some Gα subunits, releasing inorganic phosphate. Another cycle of activation can then continue with exchange of nucleotide.

The small, or monomeric, GTPases are the smallest form of these molecular switches. The Ras superfamily is a well-studied group of small GTPases whose members all share a common core catalytic domain. This superfamily is divided into five families, including Rho, which is further divided into three subfamilies, Rho, Rac and Cdc42. All Rho family members play important roles in the regulation of the actin cytoskeleton and gene transcription, as well as the proliferation, survival and morphology of the cell(5). It is because of these functions that dysregulation of Rho family members occurs in a diverse array of diseases such as cancer, neurological disorders, and cardiovascular disease(6-8).

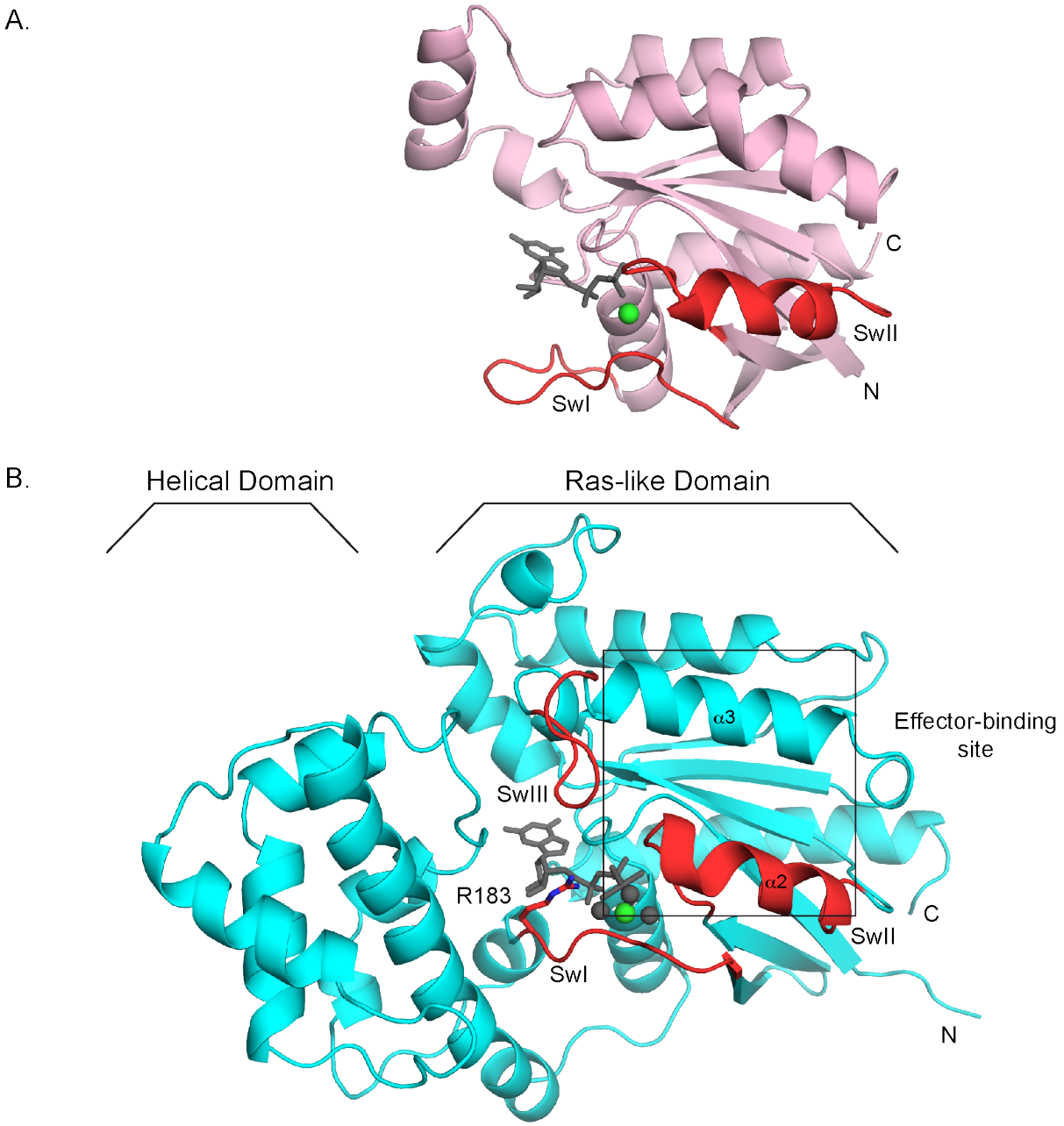

Figure 1.2 Small GTPases and Gα subunits share structural features. *A*, Small GTPases (pink) have one domain that includes two switch domains, SwI and SwII (red). SwI and SwII are directly involved in hexa-coordination of Mg^{2+} (green sphere) and nucleotide binding (gray sticks). *B*, Gα subunits (blue) are GTPases with two domains. The helical domain is completely α-helical, whereas the Ras-like domain shares the same fold found in small GTPases. Gα subunits also have SwI and SwII domains, as well as an additional SwIII domain. The effector-binding site is formed by SwII, α3 and the α3-β5 loop. Gα subunits also possess a catalytic arginine (R183 in $G\alpha_q$) to aid in GTP hydrolysis, a residue not present in small GTPases and instead provided *in trans* by their GAPs.

Rho GTPases contain a single domain comprised of several α helices arranged around a core of 6 β sheets (Fig 1.2). There are several conserved segments, including the phosphate binding loop (P loop), switch I (SwI) and switch II (SwII) (9). The P loop is important for forming contacts with the α and β phosphates of the bound nucleotide and undergoes little conformational change between the active (GTP) and inactive (GDP) states (10). The switch regions are important for the coordination of Mg^{2+} and the β and γ phosphates of the nucleotide, and, as their name suggests, they exhibit large conformational changes based on whether GDP or GTP is bound(9). The switch regions appear to be quite mobile until hexa-coordination of the Mg^{2+} ion and binding of GTP, both of which stabilize the switch regions into their active conformations (9).

Intrinsic small GTPase hydrolysis rates are very low, with kcat values of ~0.2 to 0.03 min^{-1} (11). Therefore, regulatory proteins called GTPase activating proteins (GAPs) are used to stimulate the hydrolysis of GTP to GDP. Rho GAPs catalyze hydrolysis using an arginine residue, also referred to as the arginine finger, that is inserted near the GTPase active site to interact with the negative charge developed by the nucleotide phosphate groups during hydrolysis and thereby stabilize the transition state of the reaction(11). The GTPase can then hydrolyze the GTP, releasing inorganic phosphate and leaving GDP in the active site.

Small GTPases have high affinity for both GTP and GDP and so do not often exist in a nucleotide free state within the cell(11). While GTP is in excess in the cell and can rapidly populate an empty active site, it requires GDP to be removed first. Guanine nucleotide exchange factors (GEFs) can be used to bind and induce a conformation that will release the GDP and allow for GTP to bind. For Rho family GTPases, there are two known families of RhoGEFs, the Dock family and the Dbl family. Both are found in humans, but the Dbl family has been shown to interact with all three major Rho GTPases (Rho, Rac and Cdc42), while the Dock family is limited to Rac and Cdc42(12). The Dbl family is named for its founding member, Dbl, which was originally observed in diffuse B-cell-lymphoma cells (13). Dbl and the rest of its family members share a homologous domain thus termed the Dbl homology (DH) domain, which is responsible for the catalytic activity of these RhoGEFs. In addition, Dbl family members almost always contain a pleckstrin homology (PH) domain immediately following the DH domain to form their signature DH/PH tandem. The overall fold and function of the DH domain is conserved, whereas the PH domain fold is conserved but its function is variable among Dbl

family members. The PH domain commonly regulates the activity of the DH domain, but this can occur in either a positive or negative manner. In conjunction with various other domains present in these RhoGEFs, Dbl family members are able to respond to signals in diverse ways. One particular subset of Dbl family RhoGEFs links Rho family GTPases to heterotrimeric G proteins (14).

Heterotrimeric G proteins are GTPases that become activated by the seven transmembrane helix receptors called G protein-coupled receptors (GPCRs). There are approximately 800 known GPCRs that comprise this group of proteins that are able to translate extracellular stimuli into intracellular responses (15). GPCRs are the target of ~30% of today's pharmaceuticals, which emphasizes their relevance to human health as well as their prospects as successful drug targets (16). As the name suggests, GPCRs canonically bind heterotrimeric G proteins on their intracellular face as one way of transducing an extracellular signal to the inside of the cell. Signaling through other proteins such as β-arrestins and GPCR kinases (GRKs) also occurs (17).

The heterotrimeric G protein is a ternary complex formed by three separate subunits: α, β and γ, of which the α subunit is a GTPase. In comparison to the number of GPCRs that exist, there are relatively few heterotrimer subunit isoforms, but their ability to associate in various combinations in the heterotrimer provides more complexity. The Gβ and Gγ subunits are tightly associated into the Gβγ dimer, but the Gα subunit is able to separate from the complex in a GTP-dependent manner and function separately. Although there is evidence for RhoGEFs interacting with both Gα and Gβγ, regulation by Gα has been most extensively studied of the two.

The Gα subunit is a multi-domain GTPase. One domain shares the conserved fold of the small GTPases and is therefore often referred to as the Ras-like domain (Fig. 1.2). This domain is ~220 residues and contains an alternating mix of β sheets and α helices termed αN, β1-6, α1-5 and αG. The αN helix, important for heterotrimer formation, is disordered when not in complex with Gβγ (18). Additionally, the Gα N-terminus contains lipid modifications such as palmitoyl groups that help target it to the membrane (19). The second domain is ~120 residues encompassing six α helices and known accordingly as the helical domain. In the primary sequence, the helical domain is inserted between the first α helix and second β strand of the Ras-like domain and the helices are lettered A-F.

Gα subunits use a similar cycle of activation and deactivation to that of the small GTPases. They bind GTP to become activated and become inactive after they hydrolyze the GTP to GDP. GDP-bound Gα subunits associate with the Gβγ dimer to form an inert ternary complex. When a GPCR receives an agonist signal outside the cell, it employs allostery to act as a GEF for the G protein on the intracellular side of the membrane by catalyzing the exchange of GDP for GTP (20). This activates the heterotrimeric G protein, which dissociates from the GPCR and separates into two parts: the Gα subunit alone and the Gβ and Gγ subunits still tightly engaged as a dimer. Both Gα and Gβγ are able to signal at this point to their own specific set of effector proteins. Inactivation of the heterotrimeric G protein occurs with the hydrolysis of GTP to GDP on Gα, which allows for subsequent reassociation of the Gα and Gβγ subunits. The heterotrimer is then ready to bind an activated GPCR to start another cycle of signaling. Because the Gα subunit effectively dictates the activation and deactivation of heterotrimers, it is a key aspect of understanding this signaling cycle.

Like the small GTPases, Gα subunits contain SwI and SwII sites, located in the αF-β2 loop and α2 helix, respectively. Gα subunits also include a third switch region, SwIII, located in the β4-α3 loop. While SwIII does not make direct contacts with the nucleotide or Mg^{2+} in the active site, it does interact with SwII as well as precede the α3 helix of the effector-binding site. It therefore plays a role in the coupling of the active site state to effector interactions (21). In contrast to the small GTPases, most Gα subunits bind GDP with lower affinity than GTP (9). In addition, the binding of nucleotide appears to be less coupled to the binding of Mg^{2+} than the small GTPases, meaning that GDP release does not depend on Mg^{2+} and GTP can be bound into the active site without Mg^{2+} present (9, 22). Hydrolysis of GTP however cannot proceed until the hexa-coordination of Mg^{2+}, provided by the nucleotide β and γ phosphate groups, a conserved serine in the P loop, a conserved threonine in SwI and two water molecules.

Not all Gα subunit isoforms interact with all effectors, and so not all Gα subunits directly interact with Dbl family RhoGEFs. The Gα subunits have been subdivided into four classes based on similarity of their primary sequence: $G\alpha_{i/o}$, $G\alpha_{s}$, $G\alpha_{q/11}$ and $G\alpha_{12/13}$. The members of each class generally exhibit similarities in the types of effectors they engage (Fig. 1.1). The $G\alpha_{i/o}$ ($G\alpha_{i}$, $G\alpha_{o}$, $G\alpha_{t}$, $G\alpha_{z}$) and $G\alpha_{s}$ classes are most well known for their ability to inhibit or stimulate adenylyl cyclase, respectively. Adenylyl cyclase in turn regulates levels of the second messenger

cAMP. The $G\alpha_{12/13}$ ($G\alpha_{12}$, $G\alpha_{13}$) family signals through three known Dbl RhoGEFs to regulate the actin cytoskeleton. The $G\alpha_{q/11}$ ($G\alpha_{q}$, $G\alpha_{11}$, $G\alpha_{14}$, $G\alpha_{15/16}$) class signals through three other Dbl RhoGEFs (Fig. 1.3), but is more commonly known for its canonical signaling through PLCβ. PLCβ catalyzes the breakdown of membrane phospholipids into the second messengers IP_3 and diacylglcyerol (DAG) that regulate calcium and protein kinase C, respectively. These aforementioned effectors, as well as Gβγ, all make use of a similar binding site on Gα. This effector-binding site encompasses SwII, α3 and the α3-β5 loop of Gα and is located adjacent to the other switch regions. Through the use of the switch regions, the effector-binding site changes conformation based on the state of the bound nucleotide and therefore regulates whether Gβγ binding or effector interaction and signaling may occur (23).

To terminate downstream signaling, some Gα subunits employ GAP proteins to increase the rate of hydrolysis, like their monomeric counterparts (Fig. 1.3). Gα is able to hydrolyze GTP inherently at ~2 min^{-1}, but faster rates are often required for physiological processes such as eyesight (24). Proteins exhibiting GAP activity have been found to work on members of all the Gα classes except $G\alpha_s$. GAP activity on the $G\alpha_{12/13}$ members has been shown to be carried out by their canonical RhoGEF effectors (14, 25). Additionally, PLCβ exhibits GAP activity on $G\alpha_q$ (26). There also exists a separate family of GAP proteins that interact with the $G\alpha_{i/o}$ and $G\alpha_{q/11}$ subunit classes, termed the Regulators of G Protein Signaling (RGS) family. RGS family members all contain a conserved RGS domain. Because Gα subunits already contain an arginine finger *in cis*, the mechanism by which their GAPs catalyze GTP hydrolysis differs. Instead, association between the RGS protein and Gα subunit stabilizes the Gα switch regions in their transition state conformation (27). RGS proteins are able to bind Gα at a site distinct from its effector-binding site and biochemical evidence accordingly supports that ternary complexes of Gα subunits, effectors and RGS proteins do form (28, 29). Interestingly, some RGS family members can show selectivity for either the $G\alpha_{i/o}$ or $G\alpha_{q/11}$ family, while others will interact with both families. Only one RGS protein, RGS2, shows a preference for $G\alpha_{q/11}$. The mechanism that dictates this selectivity is poorly understood, and it is therefore difficult to predict selectivity based on the structure or sequence of a particular RGS domain. Chapter 2 of this thesis describes the use of x-ray crystallography to visualize a complex between $G\alpha_q$ and an RGS protein that is

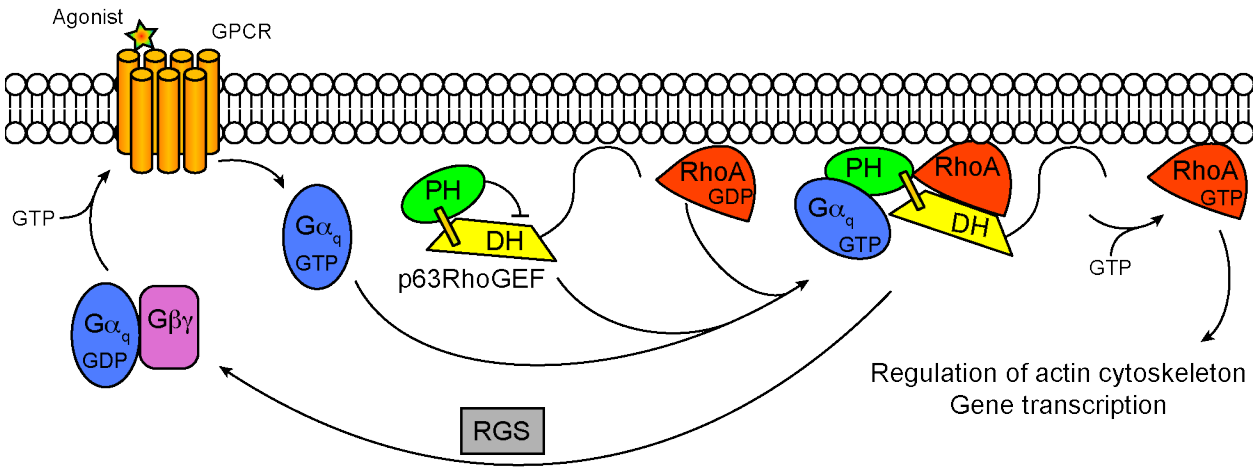

Figure 1.3 $G\alpha_q$ signaling through p63RhoGEF and inactivation by RGS proteins. $G\alpha_q$ is activated at the membrane by a GPCR. It can then activate the otherwise autoinhibited effector p63RhoGEF. GDP is exchanged for GTP on RhoA by activated p63RhoGEF. RhoA is then able to continue the signaling cascade through regulation of the actin cytoskeleton and gene transcription. To inactivate $G\alpha_q$ and end effector signaling, RGS proteins are able to catalyze the hydrolysis of GTP to GDP through release of inorganic phosphate.

selective for $G\alpha_{q/11}$ and $G\alpha_{i/o}$ subunit families. This structure allows for comparison of the same RGS protein in complex with either $G\alpha_q$ or $G\alpha_i$ for the first time. Observations from structural work paired with biochemical assays allow for a clearer model of how RGS selectivity is determined.

The types of proteins described above can all be studied in a signaling system that revolves around the $G\alpha_q$ subunit and its ability to modulate the actin cytoskeleton (Fig. 1.3). After activation by a GPCR such as the angiotensin II type 1 receptor, activated $G\alpha_q$ interacts with p63RhoGEF to relieve an autoinhibitory mechanism propagated through an unknown mechanism by its PH domain. This in turn leads to activation of the small GTPase RhoA. To end activation of RhoA, a subset of RGS proteins with selectivity for $G\alpha_q$ are able to accelerate GTP hydrolysis on the G protein. $G\alpha_q$ then reassociates with $G\beta\gamma$ until activation by another $G\alpha_q$-coupled GPCR occurs again.

The crystal structure of the DH/PH tandem of p63RhoGEF in complex with both $G\alpha_q$ and RhoA shows the activated conformation of this GEF, but no structure yet exists of the basal, inactive structure of p63RhoGEF. Chapter 3 focuses on understanding how the PH domain of p63RhoGEF inhibits the DH domain, and what role dynamics play in this mechanism. To do this, a combination of structural and biophysical methods were used. Nuclear magnetic

resonance (NMR) and small-angle x-ray scattering (SAXS) were employed to describe the orientation of the DH and PH domains in their inactive state, while molecular dynamics (MD) simulations were used to give insight into the flexibility and potential movement patterns of the helix connecting the two domains. We hope to combine these methods to determine the mechanism behind autoinhibition and how $G\alpha_q$ may be relieving it.

Chapter 2

Structure of the Regulator of G Protein Signaling 9 (RGS8)-$G\alpha_q$ Complex

Introduction

The first suggestion of GAP protein existence was in 1987 with the discovery that a protein accelerated GTP hydrolysis on wild-type Ras *in vivo*, but not on oncogenic variants of Ras (30). This discovery helped explain why oncogenic mutations did not need to decrease the *in vitro* hydrolase activity of Ras to affect the ability of Ras to transform cells (31, 32). In heterotrimeric G proteins, it had also been noticed that *in vitro* and *in vivo* hydrolysis rates do not always coincide. Deactivation of $G\alpha_t$ in the visual system had been observed at much faster rates *in vivo* than those measured for isolated $G\alpha_t$ subunits *in vitro*, but the reason for this acceleration was not specifically attributed to another protein at the time (33, 34).

It was not until a 1995 budding yeast mating study that the discrepancy between *in vitro* and *in vivo* GTP hydrolysis rates was attributed to a GAP protein (35). In yeast, pheromones can act on GPCRs at the cell surface and induce growth arrest via $G\beta\gamma$ downstream signaling. The protein Sst2 acts to attenuate this G protein-mediated signaling pathway, thereby allowing for growth recovery. Expression of dominant negative Sst2 mutants results in a loss of growth recovery. Furthermore, overexpression of either $G\beta\gamma$ or $G\alpha$ is able to rescue growth recovery (35). Dohlman et al. concluded that Sst2 inactivates the $G\alpha$ subunit Gpa1 by directly interacting with it. After several other proteins, including 9 mammalian ones, were found to share a region found in Sst2, this domain was named the regulator of G protein signaling (RGS) domain (36).

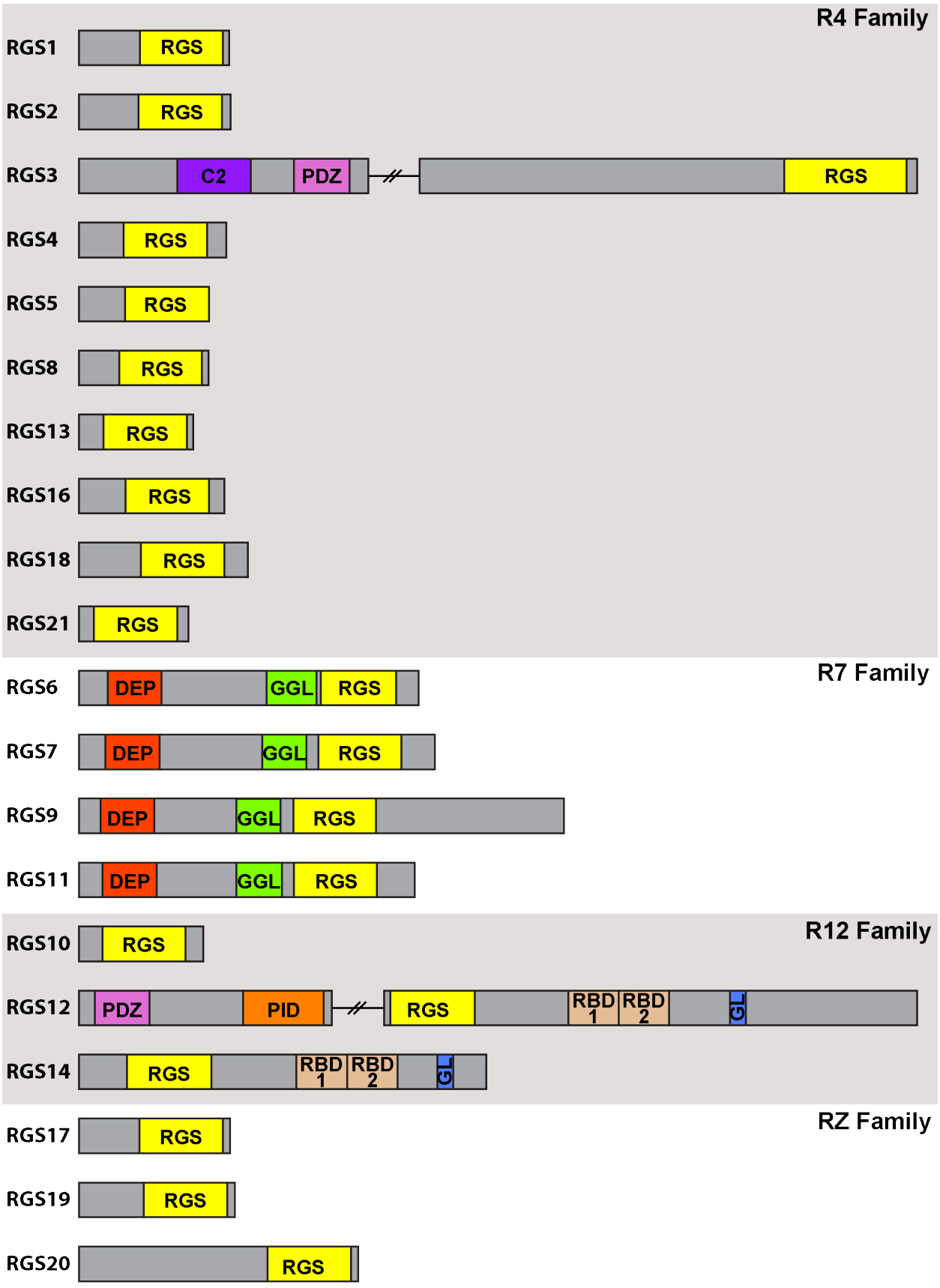
R4 Family
RGS1
RGS
RGS2
RGS
RGS3
C2
PDZ
RGS
RGS4
RGS
RGS5
RGS
RGS8
RGS
RGS13
RGS
RGS16
RGS
RGS18
RGS
RGS21
RGS
R7 Family
RGS6
DEP
GGL
RGS
RGS7
DEP
GGL
RGS
RGS9
DEP
GGL
RGS
RGS11
DEP
GGL
RGS
R12 Family
RGS10
RGS
RGS12
PDZ
PID
RGS
RBD 1
RBD 2
GL
RGS14
RGS
RBD 1
RBD 2
GL
RZ Family
RGS17
RGS
RGS19
RGS
RGS20
RGS

Figure. 2.1 Domain structure of the R4, R7, R12 and RZ subfamilies of RGS. All RGS family members contain a RGS homology domain (yellow). Other domains include PDZ, C2, DEP, GGL, PID (phosphotyrosine interaction domain), RBD (Raf-like Ras-binding domain) and GL (GoLoco). RGS17 is also known as RGSZ2, RGS19 also as GAIP, and RGS20 also as RGSZ1.

Today, the mammalian RGS family contains more than 20 members and is further divided into several subfamilies based on sequence homology in the RGS domain (Fig. 2.1). There are four main subfamilies of RGS proteins (R4, R7, R12, RZ). There are also several additional, yet more distantly related, proteins that contain RGS-like domains [e.g. GPCR kinases (GRKs), $G\alpha_{12/13}$-regulated RhoGEFs]. Each subfamily tends to share a similar overall modular structure. For instance, the R7 subfamily members all contain DEP (Dishevelled, Egl-10 and Pleckstrin) and GGL (G protein gamma-like) domains, while the R4 and RZ subfamily members typically contain no additional structural domains besides their RGS domain.

Each RGS protein does not interact equally with all Gα subunits and selectivity for certain Gα types over others tends to be shared within RGS subfamilies (Fig. 2.2). All four subfamilies utilize $G\alpha_{i/o}$ subunits as substrates. A surface plasmon resonance study indicated that R7 and R12 subfamily members bind weakly or not at all to $G\alpha_q$, whereas most RZ and R4 subfamily members interact with both $G\alpha_i$ and $G\alpha_q$ (37). One exception is RGS2, an R4 subfamily member that is uniquely selective for $G\alpha_{q/11}$ subunits (38). Varying preferences of RGS proteins for individual Gα subfamily members has also been shown, for example the RZ family member RGS20 (RGSZ1) seems selective for $G\alpha_z$ subunits, whereas RGS19 (GAIP) prefers $G\alpha_{i1}$, $G\alpha_{i3}$ and $G\alpha_o$ (39, 40). No RGS protein has been found to have selectivity for $G\alpha_s$, but a single point mutation in the SwII region of $G\alpha_s$ (D229S) to the residue found at the equivalent position in $G\alpha_t$ allowed for RGS interaction (41). Interestingly, while D229 of $G\alpha_s$ was identified as a residue that prohibited association with RGS proteins, mutation of RGS residues at the interface near D229 in an attempt to allow for interaction with $G\alpha_s$ was unsuccessful (41).

The first structure of an RGS protein was especially informative because it was determined in complex with $G\alpha_{i1}$ (42). It demonstrated that the RGS domain is comprised of nine helices (α1-α9) arranged into two subdomains (Fig. 2.3). The helices α1-α3 and α8-α9 make up the terminal subdomain while helices α4-α7 form the second subdomain, a right-

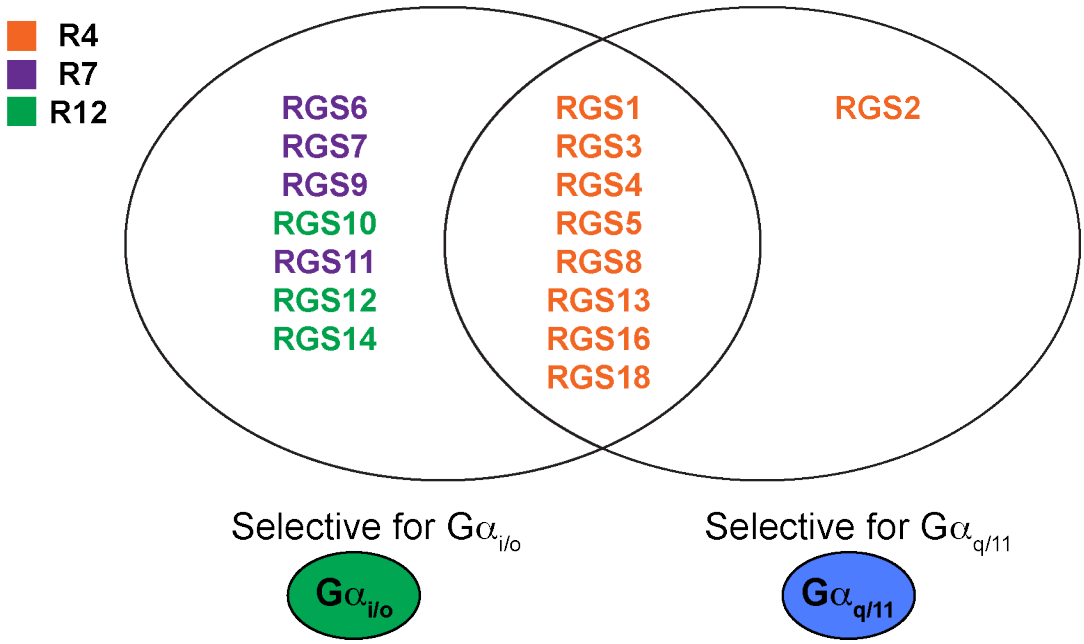

Figure 2.2 Selectivity of RGS family members for $G\alpha_{i/o}$ or $G\alpha_{q/11}$ subunits. RGS subfamilies are colored orange for R4, green for R12 and purple for R7. RGS2 is the only RGS family member shown with high selectivity for $G\alpha_{q/11}$ over $G\alpha_{i/o}$, while the R7 and R12 subfamily members show high selectivity for $G\alpha_{i/o}$.

handed four-helix bundle. The RGS domain is the minimal unit required for GAP activity and further truncation results in loss of activity, as may be predicted based on the degree of sequence conservation seen even at the N- and C-termini (36, 43). Although this first structure used a full-length variant of RGS4, only the RGS domain was found to be ordered (42).

While generally the same, there do exist sequence and structural differences among RGS family members. The α1-α2, α4-α5, and α6-α7 loops are variable in length between the subfamilies. The R12 members have a 1-residue extension in their α5-α6 loop which is in close proximity to SwIII of Gα in complexes, and the α6 helices of R12 members are poorly formed compared to the R4, R7 and RZ members (37). In their apo conformation, the R12 subfamily α6 region is pseudohelical until the last ~2 turns. The R12 family member RGS10 has also been crystallized in complex with $G\alpha_{i3}$ (2IHB), where the α6 helix is completely disordered (37). Therefore it is likely that a more helical secondary structure does not occur upon complex formation.

Although RGS domains largely superimpose very well upon each other, some flexibility of the domain has been noted. An apo-RGS4 structure determined by NMR showed that the kink

that marks the transition from helix 7 to helix 8 shifts its location towards the N-terminus upon the binding of $G\alpha_{i1}$, resulting in a longer α8 helix and a shorter α7 helix (44). The α6 helix of RGS10 is highly flexible based on solution NMR data, and comparison of crystal structures of RGS2 in complex and by itself also shows a flexible α6 (37, 45).

Investigations into molecular determinants of selectivity could be grouped into two categories, the first of which being centered on the switch regions of Gα. As seen in the RGS4–$G\alpha_{i1}$ complex, the major binding interface of the complex is near the Gα switch regions. This interface is mostly comprised of interactions with SwI and SwII, but also involves SwIII of Gα, and they are used in a tripod-like arrangement to contact the RGS domain. The α3-α4 loop of the RGS contacts Sw I and Sw II of the G protein, the α5-α6 loop predominantly contacts Sw II and Sw III, and α8 and its preceding loop interact with SwI. Three highly conserved residues in the switch regions (S85, D163 and K170 in RGS4) have been shown to be important for GAP activity with $G\alpha_{i/o}$ subunits (38, 46). The serine and aspartate are invariable among all RGS proteins except RGS2, which instead has a cysteine and asparagine at these positions,

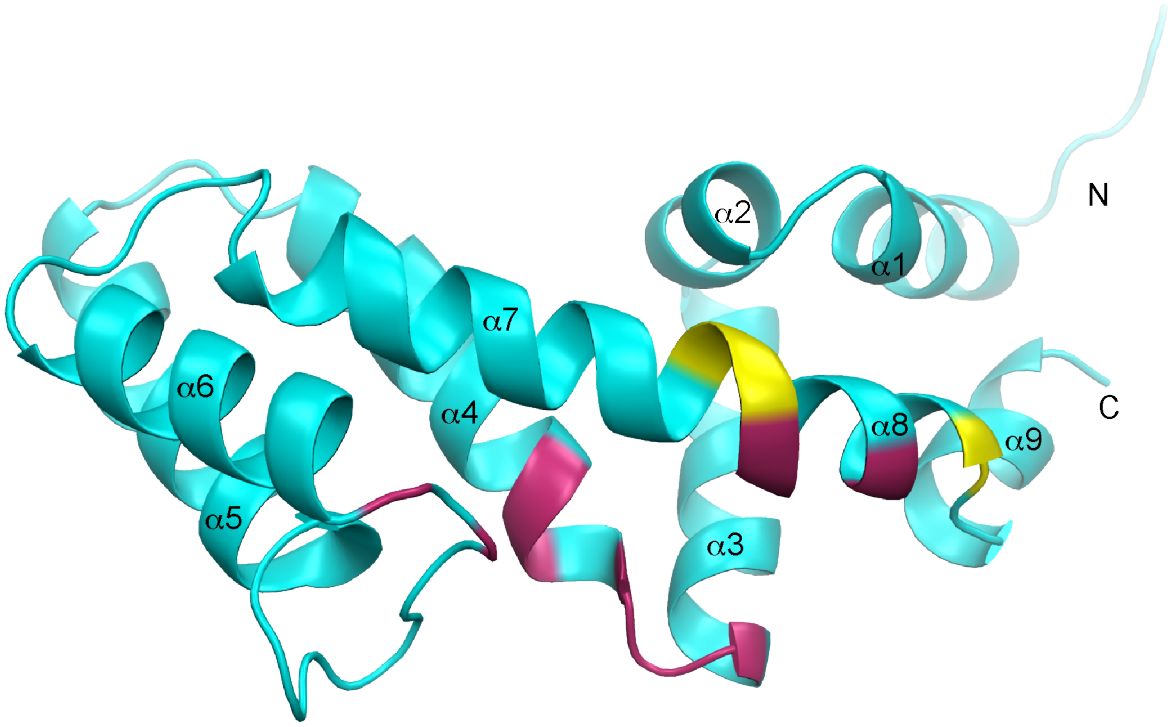

Figure 2.3 Structure of the RGS domain. The structure of RGS8 (5DO9) is shown. The N- and C-termini are denoted by N and C, respectively. Regions contacting the Ras-like domain of Gα are shown in magenta and the α-helical domain are shown in yellow.

respectively. The third position is not as well conserved, but tends to be a positively charged residue (lysine or arginine) in most RGS members, while being negatively charged in RGS2 (glutamate). Mutation of these residue positions in RGS2 to what is found in RGS4 (C106S, N184D, E191K) results in an RGS2 triple-mutant ($RGS2^{SDK}$) with improved GAP activity on $G\alpha_{i1}$ or $G\alpha_o$, while retaining activity on $G\alpha_q$ (38, 46). The cognate RGS4 triple mutant (S85C, D163N, K170E) loses GAP activity on $G\alpha_o$, while also still retaining activity on $G\alpha_q$. These three residues thus appear to dictate selectivity for the $G\alpha_{i/o}$ subfamily, but not for $G\alpha_{q/11}$, as GAP activity of RGS2 and RGS4 triple-mutants on $G\alpha_q$ did not differ from wild-type. Thus the molecular basis for how RGS domains are selective for or against $G\alpha_{q/11}$ is more elusive.

Additional selectivity studies have probed the more variable RGS interaction with the Gα α-helical domain as another possible selectivity determinant. Interactions between the RGS α8 N-terminus and the G protein αA helix have been most frequently observed, but residues in the RGS α8 helix or G protein αB-αC loop have also been observed to make interactions (37). One of the earliest of these studies showed that a region of $G\alpha_t$ (residues 56-173) containing the α-helical domain but not the switch regions was responsible for RGS9 selectivity for $G\alpha_t$ over $G\alpha_i$ (47). The structure of wild-type RGS2 in complex with $G\alpha_q$ also implicated the α-helical domain (45). Superposition of the Gα subunits in the $RGS2^{SDK}$–$G\alpha_{i3}$ and RGS2–$G\alpha_q$ complexes shows a distinct difference between the αB-αC loops of $G\alpha_i$ and $G\alpha_q$ when in complex with an RGS protein. This αB-αC loop is also one of only two regions that change structure in $G\alpha_q$ complexes with various targets. The loop of $G\alpha_q$ is less ordered and protrudes out farther towards α7 of the RGS protein compared to $G\alpha_i$. The RGS2–$G\alpha_q$ complex revealed α-helical domain interactions that involved two residues not unique to RGS2 (K175 and E182) and three residues unique to $G\alpha_q$ (L78, Q81 and E119). Both L78 and Q81 are also conserved across all $G\alpha_{q/11}$ subfamily members. One or more of these interactions might therefore account for ways in which several RGS proteins can select for $G\alpha_q$, but the lack of high sequence conservation in RGS proteins at these positions of interaction and the lack of any close contacts observed in complexes between RGS1 or RGS16 with the α-helical domain of $G\alpha_{i1}$ suggests that this will not be a comprehensive explanation of selectivity. Furthermore, mutation of some of these interacting RGS2 residues resulted in either no change in GAP activity (E182A) or slightly increased GAP activity (K175A) (45). Mutation of $G\alpha_q$ residues to their analogous residues in $G\alpha_i$ did not

decrease GAP activity either, except for the E119A/K120A double mutant (45). Because single point mutants were not tested as well, it is unclear whether only one of the of mutations is required for this increase or if they are needed in combination. It is particularly interesting because K120 of $G\alpha_q$ was not indicated to be making contact with the RGS protein.

The structure of RGS2 in complex with $G\alpha_q$ also revealed a distinct binding mode for an RGS protein in complex with Gα. Superposition of the Gα subunits in the $RGS2^{SDK}$–$G\alpha_{i3}$ and RGS2–$G\alpha_q$ complexes reveals a 7˚ lean of RGS2 (45). This is notable because all previous complexes showed a "canonical" pose similar to that of $RGS2^{SDK}$ in complex with $G\alpha_{i3}$. Because this was also the first RGS domain–$G\alpha_q$ complex to be structurally characterized, it was unclear if the significant tilt in the orientation of the RGS domain with respect to other RGS domains in complex with Gα was due to sequence differences in either RGS2 or $G\alpha_q$. Therefore, before one can address the molecular basis for why some RGS proteins select against $G\alpha_{q/11}$ subfamily members, structures of conventional R4 subfamily members in complex with $G\alpha_q$ need to be determined.

To this end, the RGS domain of another R4 family member in complex with $G\alpha_q$ was crystallized. The structure was solved by x-ray crystallography and compared to the existing structures of Gα–RGS complexes. Residues that were identified as possible determinants of selectivity were mutated in both an R4 and R12 subfamily member in an attempt to alter the selectivity of the RGS domains. The GAP activities on $G\alpha_q$ and $G\alpha_i$ of these mutants were tested and compared to their wild-type counterparts using a single-turnover GAP assay. These studies produced a refined model for how selectivity is achieved between RGS domains and Gα subunits (48).

Methods

Protein expression and purification

All constructs encoding RGS variants were confirmed by sequencing on both strands. Residues 42-173 spanning the RGS domain of RGS8 were expressed using the pQTEV vector (a kind gift from Dr. R. Neubig, Michigan State University). Residues 22-157 spanning the RGS domain of RGS10 were expressed using a pLIC-SGC1 vector obtained from the Structural Genomics Consortium (37). After cleaving the N-terminal 6x His-tag with tobacco etch virus

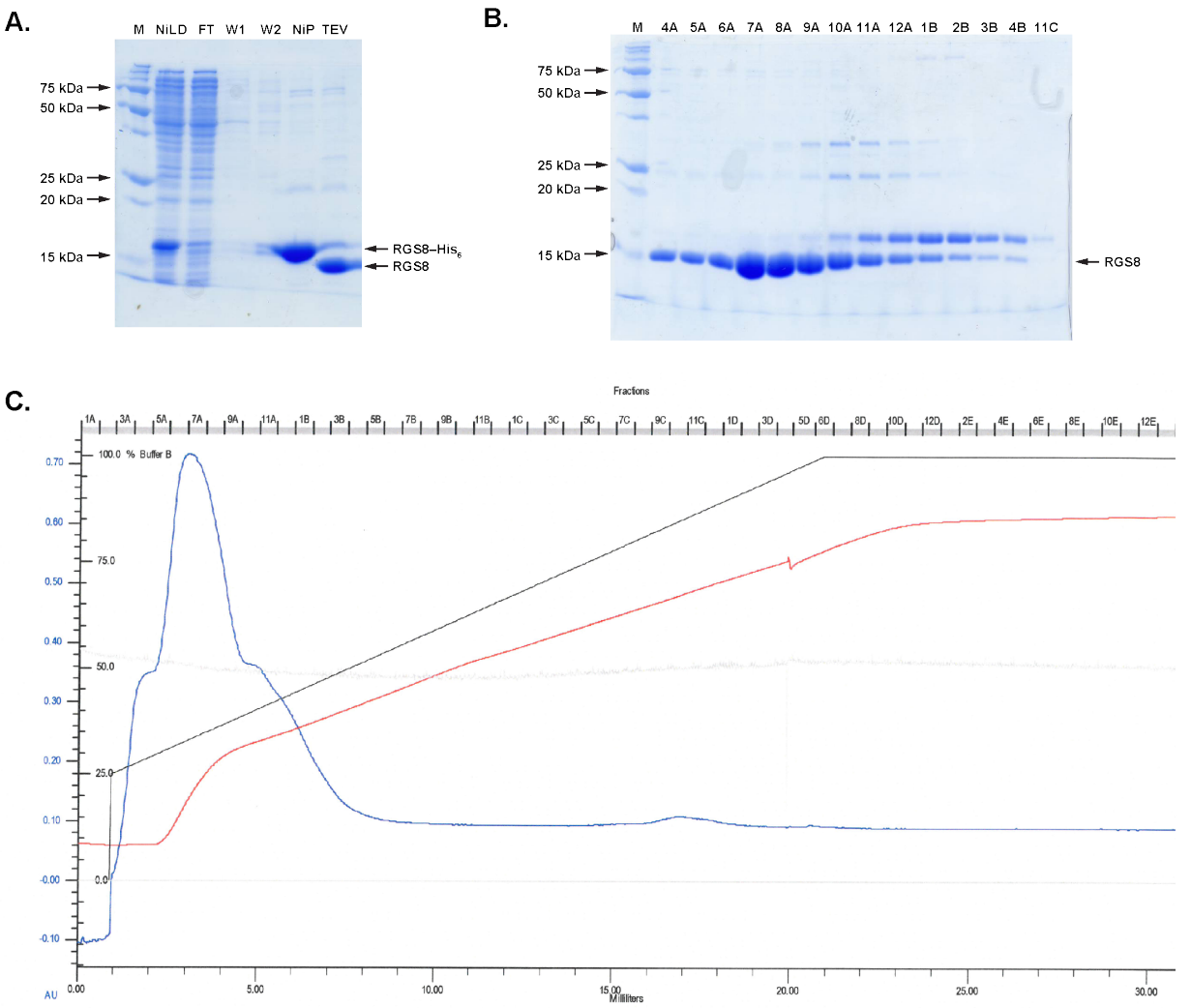

Figure 2.4 Purification of His-tagged RGS8. *A*, SDS-PAGE gel showing fractions taken from the isolation of His-tagged RGS8 and subsequent TEV-cleavage. M denotes the size marker, NiLD is the supernatant loaded onto the Ni-NTA column, FT is the flow-through upon loading the Ni-NTA column, W1 and W2 are the elutions after the first and second washes of the Ni-NTA column, respectively, NiP is the final collected elution from the Ni-NTA column, TEV is the protein after cleavage of the His-tag using TEV protease. *B*, SDS-PAGE gel showing selected fractions from the UnoS ion-exchange column chromatography. M denotes size marker, numbers above lanes correspond to chromatogram fractions. *C*, Chromatogram of UnoS ion-exchange column purification. In red is the conductivity, in blue is the UV absorbance, in black is the buffer gradient.

(TEV) protease from RGS8 and RGS10, the exogenous sequence QSM is left on the N-terminus.

For RGS8 variants (Fig. 2.4A-C), 1 L of BL21 Rosetta cells grown in Terrific Broth were induced with 100 mM IPTG at 20 ˚C. The cells were pelleted by centrifugation at 3500 *g* for 15 min and then resuspended in Buffer A (20 mM HEPES pH 8.0, 500 mM NaCl, 10 mM β-

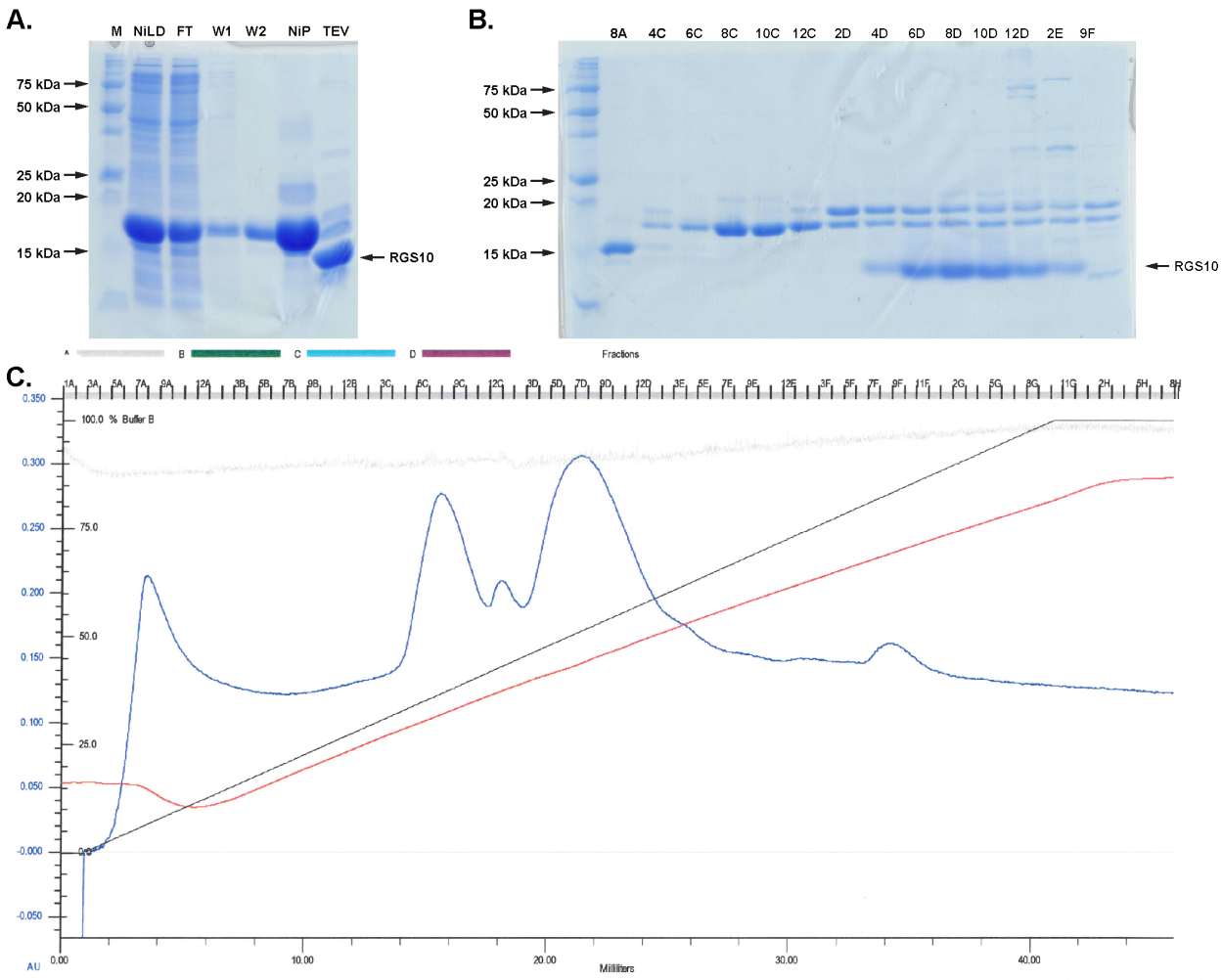

Figure 2.5 Purification of His-tagged RGS10. *A*, SDS-PAGE gel showing fractions taken from the isolation of His-tagged RGS10 and subsequent TEV-cleavage. Abbreviations are as in Fig. 2.4. *B*, SDS-PAGE gel showing selected fractions from size exclusion column chromatography. M denotes size marker, numbers above lanes correspond to chromatogram fractions. *C*, Chromatogram of size exclusion column purification. In red is the conductivity, in blue is the UV absorbance.

mercaptoethanol [βME]), supplemented with 7.6 µM leupeptin, 360 nM lima bean trypsin inhibitor, 1 mM PMSF and 0.1 mM EDTA before douncing to homogeneity. Cells were then lysed using an EmulsiFlex-C3 homogenizer (Avestin). Cell debris was pelleted by centrifugation at 40,000 rpm (185,500 *g*) in a Type 45 Ti fixed angle rotor (Beckman-Coulter). The supernatant was passed over a 5 mL Ni-NTA affinity column pre-equilibrated with Buffer A. The column was then washed with 100 mL Buffer A, followed by 100 ml of Buffer A with 10 mM imidazole pH 8.0. RGS8 was eluted from the affinity column using 25 mL of Buffer A with 150 mM imidazole pH 8.0, and then dialyzed into 20 mM Na acetate pH 5.5, 0.5 M NaCl and 10 mM

βME (Fig. 2.4A). The salt concentration was reduced by diluting 4-fold into Buffer B (20 mM Na acetate pH 5.5 and 2 mM DTT) and the protein was loaded onto an UnoS ion-exchange column (Bio-Rad) and eluted using Buffer B in a NaCl gradient increasing from 125 mM to 1 M (Fig. 2.4C). Fractions absorbing at 280 nm were verified using SDS-PAGE (Fig. 2.4B) and pooled and concentrated to 4-9.5 mg/mL. For cleavage of the His-tag, 2% (w/w) TEV protease was added during a final dialysis into Buffer A.

RGS10 variants were expressed and purified (Fig. 2.5A-C) similarly to RGS8 until after elution from the Ni-NTA affinity column. Cleavage of the His-tag was then performed as described for RGS8, followed by passage over a second Ni-NTA affinity column to remove the cleaved tag and His-tagged protease (Fig. 2.5A). The flow-through was collected, concentrated to ~7.5 mg/mL, and then buffer-exchanged on tandem Superdex 200 10/300 GL (GE Life Sciences) gel filtration columns into Buffer A with 5 mM DTT instead of βME (Fig. 2.5C). Fractions absorbing at 280 nm were verified using SDS-PAGE (Fig. 2.5B), then pooled and concentrated to 7.5-9 mg/mL.

The insect cell vector pFastBacHT expressing an N-terminally truncated variant of *Mus musculus* $G\alpha_q$ spanning residues 35-359 (ΔN-$G\alpha_q$) was described previously.(45) For purification, 6 L of High Five™ cells (BTI-TN-5B1-4) expressing ΔN-$G\alpha_q$ were pelleted at 3000 *g* for 20 min. The pellet was then resuspended in Buffer A (20 mM HEPES pH 8.0, 100 mM NaCl, 10 mM βME, and 10 μM GDP pH 8.0), 7.6 μM leupeptin, 360 nM lima bean trypsin inhibitor, 1 mM PMSF, 0.1 mM EDTA, and 3 mM $MgCl_2$. Cells were then dounced, lysed and pelleted as described for RGS8. The supernatant was then passed through a Ni-NTA agarose affinity column pre-equilibrated with Buffer A supplemented with 1 mM $MgCl_2$. The column was washed with 100 mL of Buffer A plus 1 mM $MgCl_2$, followed by 100 mL of Buffer A plus 1 mM $MgCl_2$ and 10 mM imidazole pH 8.0, and then eluted with 25 mL of Elution Buffer (Buffer A with 1 mM $MgCl_2$ and 150 mM imidazole pH 8.0). $G\alpha_{i/q}$-R183C was produced as described previously (29).

The *E. coli* vector pQE60 expressing a C-terminal, 6x His-tagged $G\alpha_{i1}$ spanning residues 1-354 was provided courtesy of Dr. Barry Kreutz (U. of Illinois at Chicago). Expression was carried out as described previously (49). Purification was similar to RGS8, with the following exceptions. The Lysis Buffer was 50 mM HEPES pH 8.0, 1 mM EDTA, 2 mM DTT, 0.1 mM PMSF, 7.6 uM leupeptin, 360 nM lima bean trypsin inhibitor. Buffer A was 50 mM HEPES pH

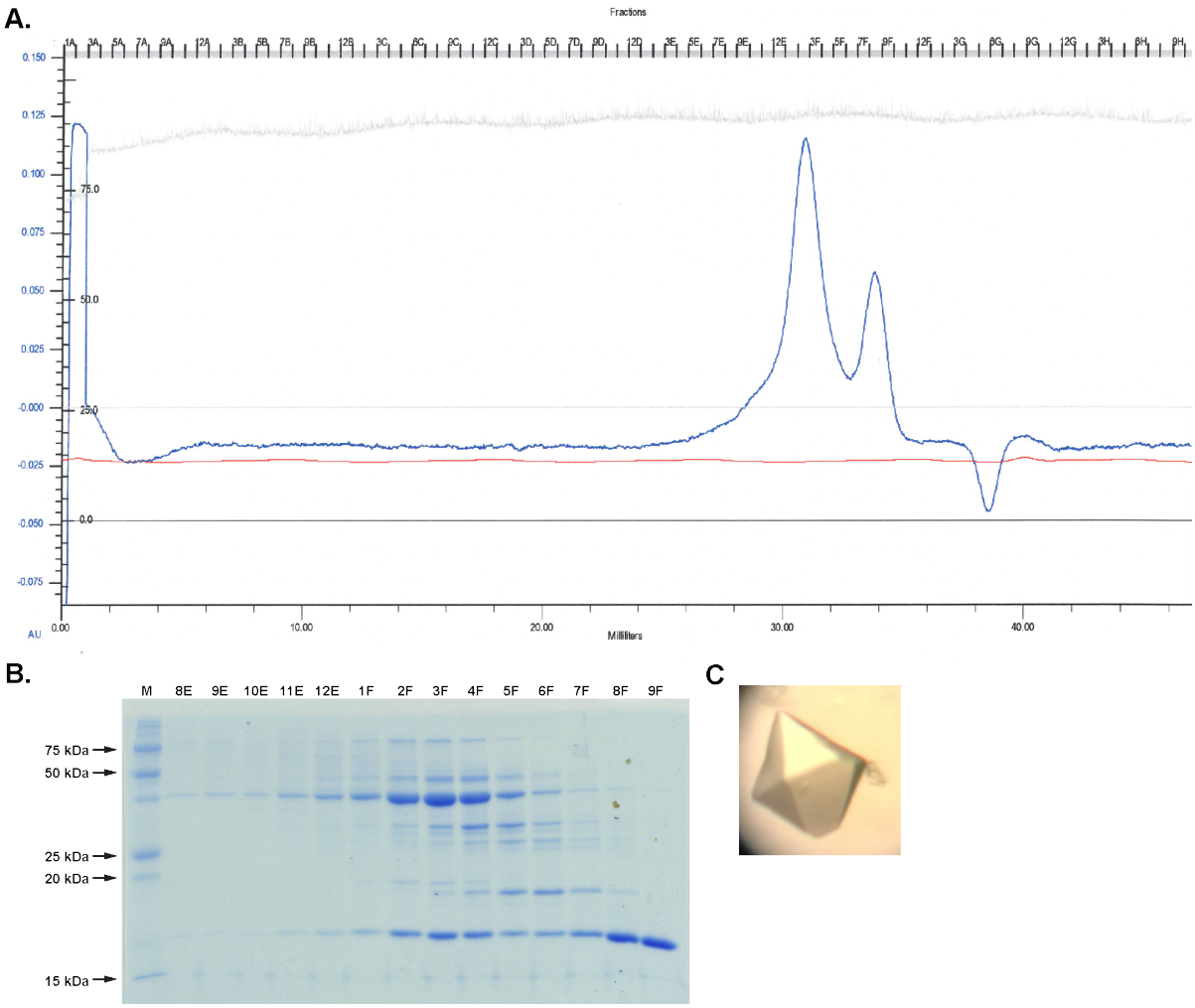

Figure 2.6 Isolation of RGS8- Gα_q complex by size exclusion column chromatography. *A*, Chromatogram of size exclusion column purification. *B*, SDS-PAGE gel showing fractions from chromatogram. M denotes size marker, numbered labels correspond to fractions on chromatogram. *C*, RGS8-Gα_q crystal.

8.0, 2 mM DTT. After washing the Ni-NTA affinity column with Buffer A, the elution step was performed using Elution Buffer (50 mM HEPES pH 8.0, 2 mM DTT, 150 mM imidazole pH 8.0). The eluate was then loaded onto an UnoQ anion exchange chromatography column (Bio-Rad) prequilibrated with Buffer A, and eluted using a gradient of 0 mM to 250 mM NaCl in Buffer A. Integrity of Gα_{i1} was confirmed by visualizing trypsin digests on SDS-PAGE as described previously (50).

Purification of the RGS8–ΔN-Gα_q Complex

Purified ΔN-Gα_q was incubated with 30 μM $AlCl_3$, 10 mM NaF and 1 mM $MgCl_2$ in a buffer also containing 10 μM GDP pH 8.0, 20 mM HEPES pH 8, 100 mM NaCl and 2 mM DTT. It was then mixed with purified RGS8 in a 1:1 molar ratio based on the RGS8 concentration determined using a NanoDrop^{TM} ND-1000 spectrophotometer, and the ΔN-Gα_q concentration determined using Bradford Reagent. The proteins were incubated together for 30 min on ice before loading onto tandem Superdex 200 10/300 GL (GE Life Sciences) gel filtration columns equilibrated with 20 mM HEPES pH 8.0, 100 mM NaCl, 2 mM DTT, 10 μM GDP pH 8.0, and 1 mM $MgCl_2$ (Fig. 2.6A). Fractions shown to contain 1:1 complex by SDS-PAGE (Fig. 2.6B) were then concentrated to 5-7 mg/mL.

Crystallization and cryoprotection

Crystals were grown in VDX plates (Hampton) using hanging drop vapor diffusion on glass cover slides. The RGS8–ΔN-Gα_q complex (6.6 mg/mL) was mixed 1:1 with well solution to a final volume of 1 μL and suspended over 1 ml of well solution. Octahedral crystal (Fig. 2.6C) grew in 2 weeks at 4 ˚C using a well solution containing 0.1 M ammonium acetate, 0.1 M BisTris pH 5.5, and 11% PEG 8000. Crystals were harvested by adding several μL of cryoprotectant (20 mM HEPES pH 8.0, 100 mM BisTris pH 5.4, 200 mM ammonium acetate, 15% PEG 8000, 200 mM NaCl, 1 mM DTT, 50 μM GDP pH 8.0, 20 μM $AlCl_3$, 10 mM NaF, and 5 mM $MgCl_2$) in 0.5 μL increments to the drop containing the crystal. The crystal was then transferred into 100% cryoprotectant and moved stepwise through mixtures of cryoprotectant plus glycerol until a final glycerol concentration of 24% (v/v). The crystal was then suspended in a nylon loop and frozen in liquid nitrogen.

Data collection, processing, and model building

X-ray diffraction data was collected at the Life Sciences Collaborative Access Team (LS-CAT) beamline 21-ID-D at the Advanced Photon Source (APS). Reflection intensities were integrated and scaled using HKL2000, and initial phases determined by molecular replacement using PHASER and structures of DN-Gα_q from PDB entry 4EKD and RGS8 from PDB entry 2ODE as search models. Manual model building in Coot was alternated with TLS refinement with local NCS restraints in REFMAC5. Coordinates and structure factors are deposited with the

Data Collection	RGS8–ΔN-Gα$_q$
X-ray source	APS 21 ID-D
Wavelength (Å)	1.0383
D_{min} (Å)	112.58-2.60 (2.64-2.60)
Space group	*C*121
Cell dimensions	
a,b,c (Å)	174.0, 95.9, 112.9
β (˚)	94.3
Total reflections	211145
Unique reflections	56869
R_{sym} (%)	12.5 (58.5)
Completeness (%)	99.27 (92.33)
$\langle I \rangle / \langle \sigma_I \rangle$	7.6 (4.1)
Redundancy	3.7 (3.6)
$CC_{1/2}$	(71.5)
Refinement	
Refinement resolution (Å)	30.0-2.60 (2.66-2.60)
Total reflections used	54036 (3705)
RMSD bond lengths (Å)	0.013
RMSD bond angles (˚)	1.584
Est. coordinate error (Å)	0.219
Ramachandran plot	
favored, outliers (%)	98.35, 0.00
R_{work}/R_{free} (%)	17.8/22.5 (27.0/31.0)
Protein atoms	11092
Ligand atoms	102
Solvent molecules	231
Average B-factor (Å^2):	47.82
Protein	48.22
Ligand	27.12
Solvent	37.71
Wilson B factor (Å^2)	37.5
MolProbity score	1.39 (100th percentile)
PDB Entry	5DO9

Table 2.1 Crystallographic and refinement statistics for the RGS8-Gα$_q$ complex. Values in parentheses correspond to the highest resolution shell of data. [a] $CC_{1/2}$, Pearson correlation coefficient.

Protein Data Bank as entry 5DO9. Figures were generated using The PyMol Molecular Graphics System, Version 1.5.0.4 (Schrödinger, LLC).

GAP assays

3 mg/mL and 4 mg/mL stocks of Gα$_{i/q}$-R183C and Gα$_{i1}$, respectively, were incubated for 10 min with 10 mM EDTA, and then diluted to 0.3 μM final concentration in 300 μL Incubation Buffer (50 mM HEPES pH 8.0, 1 mM DTT, 1 mM EDTA, 100 μg/mL albumin, 5.5 mM CHAPS, 5% glycerol, 37.5 μM ammonium sulfate) plus 33.3 μCi/mL [^{32}P]-g-GTP (Perkin-Elmer, Easytides) and enough cold GTP pH 8.0 to make the total GTP concentration 6.25 μM. The reaction was then incubated at room temperature for 3 hr (Gα$_{i/q}$-R183C) or 30 min (Gα$_{i1}$). Samples were buffer exchanged into fresh Incubation Buffer using a pre-equilibrated Micro Bio-Spin™ chromatography column (Bio-Rad) and stored on ice for the duration of the assay. Each assay was initiated by adding 20 μL of the buffer-exchanged Gα subunit to a tube containing 100 nM RGS protein in 180 μL Assay Buffer (20 mM HEPES pH 8.0, 80 mM NaCl, 1 mM DTT, 1 mM EDTA, 0.9 mM $MgCl_2$, 1 mM cold GTP pH 8.0, 10 μg/mL albumin, and 0.20% w/v cholate) on ice. 40 μL aliquots of the reaction were quenched at various time points by vortexing with 750 μL ice cold Quenching Buffer (10 mM Na phosphate

pH 2.0, 5% (w/v) activated charcoal). The quenched reaction was spun for 25 min at 6500 *g* at 4 ˚C. Afterwards, 200 µL of the supernatant was added to 3 mL of Microscint^{TM} 40 scintillation cocktail (Perkin-Elmer) and read on a liquid scintillation counter instrument measuring ^{32}P cpm. Each RGS variant was tested in triplicate in three separate experiments. Data was processed in Prism 6 using a nonlinear exponential fit with a time lag for $G\alpha_{i1}$ or a straight line fit for $G\alpha_{i/q}$-R183C.

Sequence alignment and structure comparisons

Human RGS sequences from UniProt were aligned using Clustal Omega at EMBL-EBI (51). RMSD calculations were performed using Superpose from the CCP4 software suite (52,

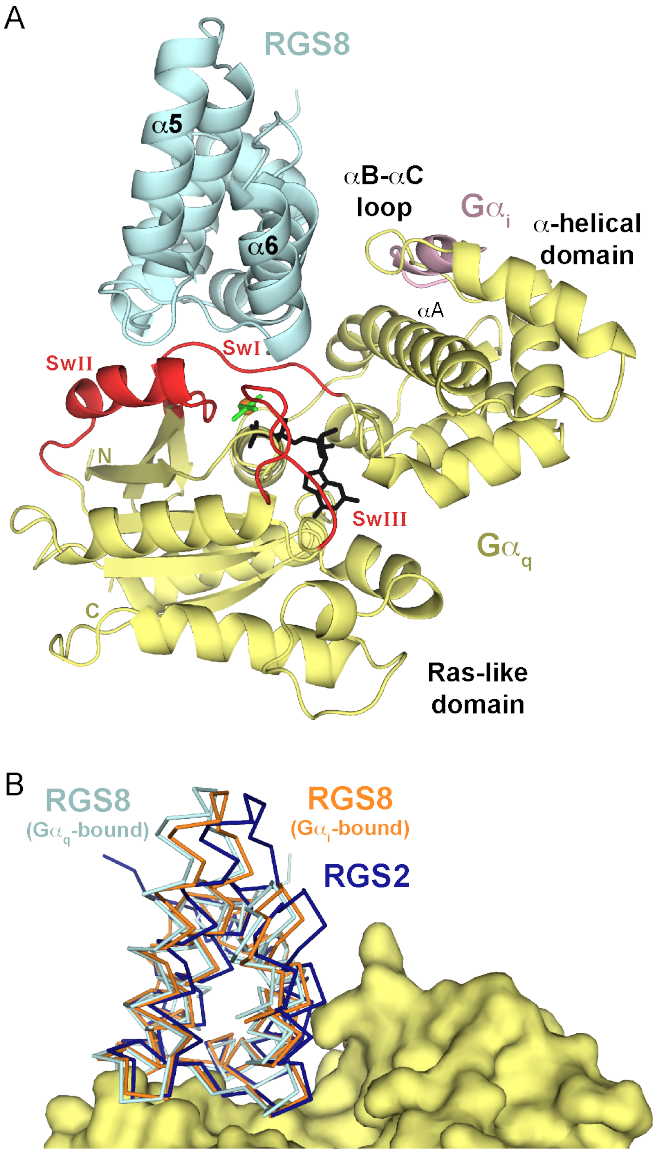

Figure 2.7 Structure of RGS8 in complex with $G\alpha_q$ reveals a canonical tilt. *A*, The 2.6 Å crystal structure of the RGS8 GAP domain in complex with ΔN-$G\alpha_q$. The αB-αC loop exhibits structural differences between $G\alpha_i$ and $G\alpha_q$ that could dictate the selectivity of RGS proteins. RGS8 is cyan, $G\alpha_q$ is yellow, the three switch regions are red, GDP is black, AlF_4^- is green, Mg^{2+} is orange, and the αB-αC loop of $G\alpha_i$ is shown in pink (PDB code 2ODE). *B*, RGS2 adopts a unique tilt when bound to $G\alpha_q$. The G subunits of the RGS2-$G\alpha_q$ complex (PDB code 4EKD), RGS8-$G\alpha_i$ complex (PDB code 2ODE), and RGS8-$G\alpha_q$ complex (PDB code 5DO9) were superimposed to compare the position of the RGS domain in each complex. $G\alpha_q$ is shown in yellow, $G\alpha_q$-bound RGS8 is shown in *pale cyan*, $G\alpha_i$-bound RGS8 is shown in orange, and RGS2 is shown in dark blue.

53). Calculation of buried surface area for complexes was performed using PISA at EMBL-EBI (54).

Results

Crystal structure of the RGS8–Gα$_q$ complex

To determine whether the altered pose of RGS2 on Gα$_q$ was due to the unique switch interface residues Cys106, Asn184 and Glu191 of RGS2 or to unique residues in the switch regions of Gα$_q$ relative to Gα$_i$, the crystal structure of the RGS domain of RGS8, an R4 subfamily member selective for both Gα$_q$ and Gα$_i$, was determined in complex with an N-terminally truncated Gα$_q$. RGS8 was used because it readily crystallizes and the structure of its complex with Gαi3 was previously reported (37). The final structure was refined to 2.6 Å spacings (Table 2.1, Fig. 2.7A). Residues 42-173 of RGS8 with two N-terminal exogenous residues are visible in all complexes, as well as residues 38-350 of ΔN-Gα$_q$. Three complexes of RGS8–Gα$_q$ exist in the asymmetric unit, with their overall RMSD in Cα positions varying by less than 0.6 Å. Comparisons with the RGS8–Gα$_{i3}$ and RGS2^{SDK}–Gα$_{i3}$ complexes give RMSD values of 0.9 Å for 432 and 426 Cα atoms, respectively, while comparison with the RGS2–Gα$_q$ complex gives an RMSD of 1.2 Å for 439 Cα atoms. This indicates that RGS8 binds Gα$_q$ in a manner most similar to how RGS proteins have previously been shown to bind Gα$_{i/o}$ subfamily members (Fig. 2.7B). Thus, the unique substitutions (Fig. 2.8A) in the Gα-binding interface of RGS2 are primarily responsible for its altered pose when bound to Gα$_q$.

Molecular Basis for RGS Subfamily Selectivity

Next, the structures of the RGS8–Gα$_i$ and RGS8–Gα$_q$ complexes were compared to identify RGS domain contacts with Gα that are distinct between the Gα$_{i/o}$ and Gα$_{q/11}$ subfamilies. The structural element that differs most is the αB-αC loop in the α-helical domain. In the RGS8–Gα$_q$ complex, the αB-αC loop is less ordered compared to the RGS8–Gα$_i$ complex based on temperature factors, but extends closer to the RGS protein, which creates additional buried surface area (Fig. 2.7A). In fact, RGS2 seems to exploit this surface to maintain greater buried accessible surface area with Gα$_q$ (2050 Å^2) than does RGS8 (1900 Å^2), or than does RGS8 in complex with Gα$_i$ (1650 Å^2). RGS residues that would contact this loop exhibit

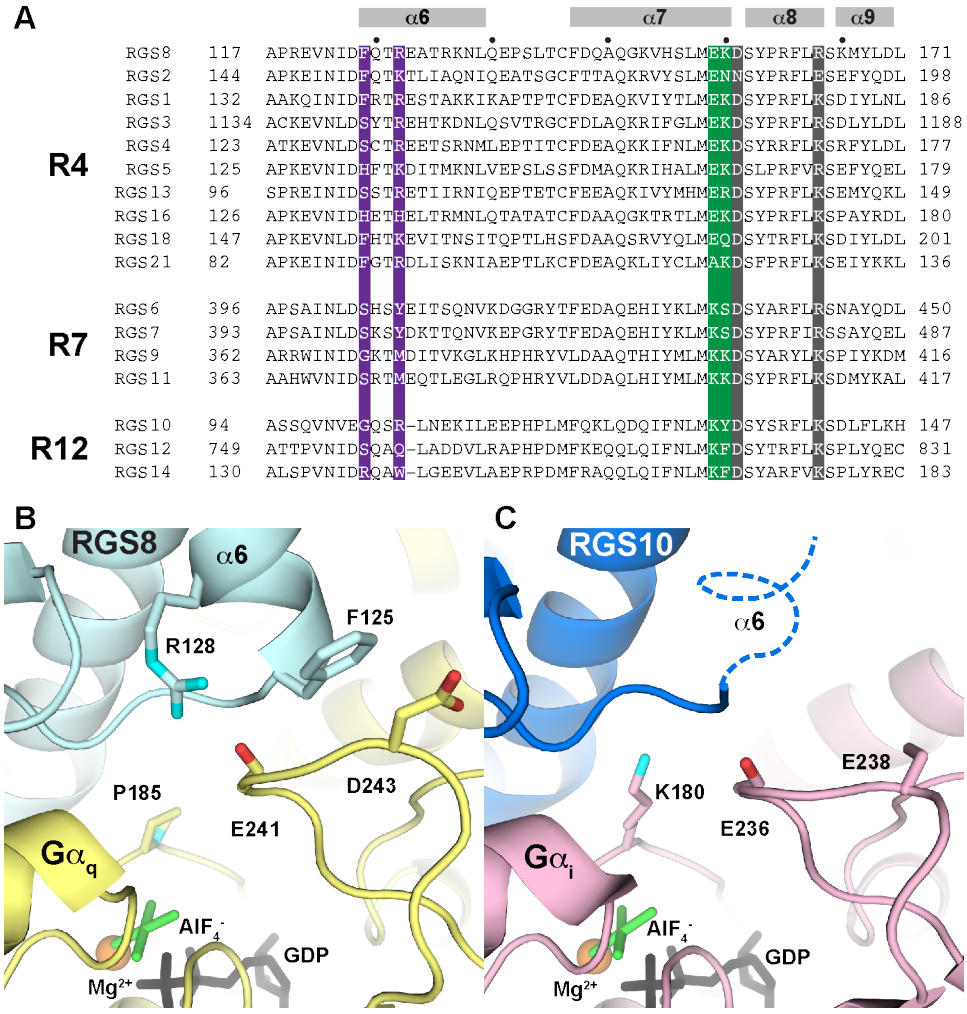

Figure 2.8 Sequence conservation of RGS8 residues in α6 and α7 suggests selectivity mechanisms. *A*, Sequence alignment of the α6-9 regions of the R4, R7, and R12 subfamilies. Alignments were performed with Clustal Omega using human sequences. Residue positions important in $G\alpha_i$ interactions are in dark gray, discussed SwIII interacting residues are in purple, and the dyad that interacts with the α-helical domain is in green. *B*, SwIII interface for the RGS8-$G\alpha_q$ complex (PDB code 5DO9). RGS8 is in cyan, and $G\alpha_q$ is in yellow. *C*, SwIII interface for the RGS10-$G\alpha_i$ complex (PDB code 2IHB). RGS10 is in blue, and $G\alpha_i$ is in pink. The disordered α6 region of RGS10 is depicted as a dashed line.

sequence heterogeneity among the various RGS subfamilies (Fig. 2.8A). The R4 family has a conserved Glu-Lys dyad in the α7 helix (RGS8 residues 155-156) whereas RGS10, an R12 member, has Lys-Tyr (residues 131-132) (Figs. 2.8A, 2.9A-B). Superposition of the Gα subunits in the RGS8–$G\alpha_q$ (Fig. 2.9A) and RGS10–$G\alpha_i$ (Fig. 2.9B) complexes suggests that charge repulsion and/or steric hindrance by this dyad could discourage binding of R12 family members to $G\alpha_q$, as there is a charge reversal in the first position and introduction of a bulkier Tyr residue

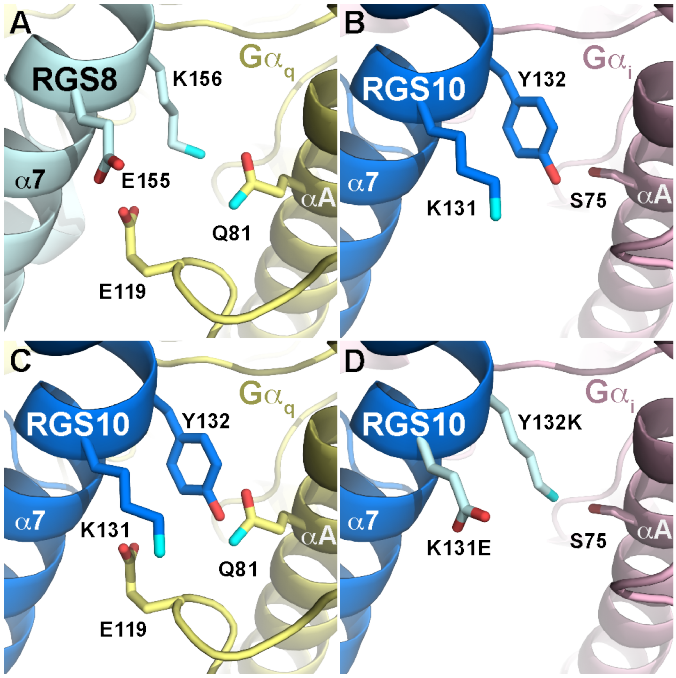

Figure 2.9 Structural models of interactions between RGS α7 and the α-helical domain of Gα. *A*, Contacts of the RGS8 α7 helix with the α-helical domain of $G\alpha_q$. *B*, Contacts of the RGS10 α7 helix with $G\alpha_i$ (PDB entry 2IHB) *C*, Contacts of the RGS10 α7 helix when modeled in complex with $G\alpha_q$. For this model, the Gα subunits of the RGS10 (2IHB) and RGS8 (5DO9) complexes were superimposed to portray RGS10 in complex with $G\alpha_q$. *D*, RGS10 K131E/Y132K double mutant modeled in complex with $G\alpha_i$. RGS10 Lys131 and Tyr132 were mutated to their corresponding residues in RGS8 using PyMOL to show the hypothetical complex. RGS8 is shown in cyan, RGS10 is shown in blue, $G\alpha_q$ is shown in yellow, and $G\alpha_i$ is shown in pink. Oxygens are depicted in red, and nitrogens are depicted in cyan.

for Lys in the second (Fig. 2.9C). In comparison, modeling Glu-Lys for the Lys-Tyr dyad of RGS10 anticipates no overt issues with $G\alpha_i$ binding (Fig. 2.9D). R7 subfamily members instead have a Lys-(Lys/Ser) dyad (Fig. 2.8A). The subfamily-specific sequences of these dyads could therefore contribute to Gα selectivity. In support of this, a previous study found that mutating these positions could effect changes in the GAP activity of two different RGS proteins on a $G\alpha_i$ family member (55).

Functional analysis of the α-helical domain interface

The aforementioned α-helical domain interface was tested by site-directed mutagenesis followed by single turnover GTPase assays using GTP[γ-32P] (Table 2.2, Fig. 2.10). RGS8-

Glu155 and/or Lys156 were converted to their analogous residues in RGS10 (Lys and Tyr, respectively). Complementary mutations were introduced in RGS10, mutating Lys131 and/or Tyr132 to Glu and Lys, respectively. If RGS selectivity for Gα subunits were achieved via ionic repulsion with the α-helical domain of $G\alpha_q$, then mutation at the first position (E155K in RGS8, K131E in RGS10) would result in a selectivity switch. Selectivity achieved through steric pressure would be potentially altered by mutation at the second position (K156Y in RGS8, Y132K in RGS10). If both sterics and charge were necessary to affect a selectivity switch, then both point mutations (E155K/K156Y in RGS8 and K131E/Y132K in RGS10) would be required.

Wild-type $G\alpha_{i1}$ and the slow-hydrolyzing mutant $G\alpha_{i/q}$-R183C were used as substrates for each RGS variant. As expected, wild-type RGS8 showed robust GAP activity on both $G\alpha_{i1}$

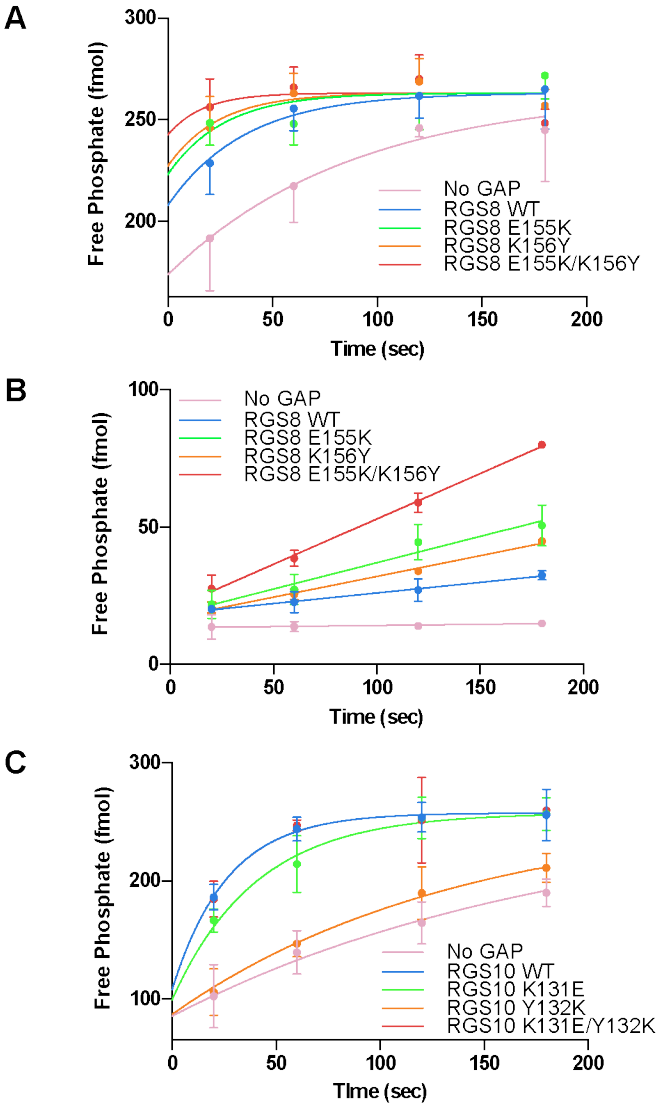

Figure 2.10 Single turnover GAP assays of RGS variants reveal modulation by contacts with the α-helical domain. *A*, Representative data from three experiments performed in triplicate of RGS8 variants using $G\alpha_i$ as a substrate. Points were fit with a non-linear regression using one-phase association with a time lag. *B*, Representative data from RGS8 variants using $G\alpha_q$ as a substrate. Points were fit with a single steady state rate. *C*, Representative data from RGS10 variants using $G\alpha_i$ as a substrate. Error bars correspond to standard deviations. GTPase activity of the Gα subunit alone is indicated in pink, wild-type RGS is indicated in blue, RGS8 E155K or RGS10 K131E is indicated in green, RGS8 K156Y or RGS10 Y132K is indicated in orange, and RGS8 E155K/K156Y or RGS10 K131E/Y132K is indicated in red.

(Fig. 2.10A) and $G\alpha_{i/q}$-R183C (Fig. 2.10B), whereas wild-type RGS10 only showed GAP activity on $G\alpha_{i1}$ (Fig. 2.10C, Table 2.2). All three mutants of RGS8 retained their activity on $G\alpha_{i1}$, but also retained wild-type, if not higher, activity on $G\alpha_{i/q}$-R183C. The RGS10 double mutant and K131E single mutant also retained activity on $G\alpha_{i3}$. Interestingly, the Y132K mutant did not. None of the RGS10 mutants showed GAP activity on $G\alpha_{i/q}$-R183C. These results indicate that the RGS domain dyad that contacts the αB-αC loop is not responsible for RGS10 being inactive on $G\alpha_q$, as RGS10 and RGS8 mutants had no increase or loss, respectively, in selectivity for $G\alpha_{i/q}$-R183C.

	$G\alpha_{i1}$ (s^{-1})	**$G\alpha_{i/q}$ R183C** (fmol/sec)
no GAP	0.013 ± 0.002	<0.01
RGS8 WT	0.042 ± 0.023	0.07 ± 0.018
RGS8 E155K	0.051 ± 0.030	0.19 ± 0.0080
RGS8 K156Y	0.063 ± 0.037	0.15 ± 0.012
RGS8 E155K/K156Y	0.051 ± 0.007	0.29 ± 0.043
no GAP	0.007 ± 0.003	<0.01
RGS10 WT	0.034 ± 0.005	<0.01
RGS10 K131E	0.021 ± 0.004	<0.01
RGS10 Y132K	0.007 ± 0.001	<0.01
RGS10 K131E/Y132K	0.029 ± 0.008	<0.01

Table 2.2 Single turnover GTPase assays using RGS8 and RGS10 variants. Values correspond to three experiments performed in triplicate for each mutant with each Gα subunit S.D. Prism 6 was used to calculate *k* values using one-phase association for $G\alpha_i$ and to calculate steady state rates using a straight line fit for $G\alpha_{i/q}$-R183C.

Conclusions

RGS proteins range from being relatively small proteins with little more than the RGS domain, to complex entities with multiple signaling domains. But even in simple RGS proteins like RGS2, 4, and 8, the regions outside the RGS domain can play important roles such as targeting these enzymes to membranes, GPCRs or effector enzymes (56-59). Thus, when one considers selectivity of an RGS protein for a particular Gα signaling pathway, there are many levels at which this can occur. However, the most fundamental level of selectivity is imposed by the direct interaction of the RGS domain with Gα to promote acceleration of GTP hydrolysis. Consequently, this study focused solely on the interaction of the RGS domain found in RGS proteins with $G\alpha_i$ and $G\alpha_q$ subunits. Moreover, previous studies have shown that isolated RGS domains exhibit selectivity for individual Gα subfamilies (37).

Previous structural analysis of the RGS2 complex with $G\alpha_q$ suggested that RGS2 has a distinct tilt relative to the Gα subunit (Fig. 2.7B) that allows it to bury more surface area with

$G\alpha_q$ than it could with $G\alpha_i$. Moreover, the conformationally flexible α6 helix of RGS2 allows it to maintain optimal contacts with SwIII, despite the unique pose of the RGS domain (45). When the Cys106, Asn184, and Glu191 interface residues are mutated to their equivalents in other RGS proteins in $RGS2^{SDK}$, it can bind to $G\alpha_i$ in a canonical fashion, but does not lose activity against $G\alpha_q$, suggesting that interactions with SwI are not directly responsible for $G\alpha_q$ selectivity (38, 46). It was further demonstrated that altering interactions between the α7 helix of the RGS2 domain and the α-helical domain of Gα can dramatically promote or inhibit GAP activity, but the molecular basis for selectivity against $G\alpha_q$ observed in other RGS subfamilies remained unclear (45).

In this work it was shown that an R4 family member, RGS8, binds to $G\alpha_q$ in a canonical fashion, permitting a more precise comparison of the interactions between RGS proteins and these two Gα subfamilies. The tilt of RGS2 in complex with $G\alpha_q$ can thus be attributed to interfacial differences dictated by unique interfacial residues in RGS2. Two regions, including the αB-αC loop of the α-helical domain, stand out as potential selectivity determinants. The G protein α-helical domain has previously been shown in some instances to be a major determinant of GAP activity, and there are sequence signatures unique to each RGS subfamily that interact with this domain (45, 47). Although a selectivity switch was not achieved in our study, the GAP assay results are consistent with RGS activity being enhanced or inhibited by interactions with the α-helical domain. Interestingly, the RGS10 Y132K mutant, creating a Lys-Lys dyad in α7, did not retain activity for $G\alpha_{i1}$, but could be rescued by addition of the K131E mutation. The disadvantage of having a Lys-Lys dyad may be due to electrostatic repulsion between the adjacent positions or with the α-helical domain. However, it seems clear that the α-helical domain is not a major $G\alpha_q$-selectivity determinant because no substitution in this interface could promote activity on $G\alpha_{i/q}$-R183C by RGS10 (Table 2.2).

Instead, the evidence now points toward the second suggested region, SwIII, which interacts with the N-terminal end of the RGS α6 helix, as being the primary determinant of selectivity (37). In SwIII, the side chain of $G\alpha_q$-Asp243 stacks with the side chain of RGS8-Phe125. The analogous residue in $G\alpha_i$, Glu238, cannot make this interaction because the backbone of its SwIII is positioned differently. Phe is shared by several other R4 family members at this position, but not by any R7 or R12 members (Fig. 2.8A). R4 RGS domains

typically also have a basic residue, e.g. RGS8-Arg128, that is positioned to form a hydrogen bond with a backbone carbonyl of another SwIII residue in $G\alpha_q$, Glu241. Members of the R7 and R12 subfamilies typically lack this basic residue. Notably, while the RGS region that comes in contact with SwIII is well ordered in complexes involving R4 family members (Fig. 2.8B-C), the RGS10 α6 helix is disordered in its complex with $G\alpha_i$, and thus contacts with SwIII are nearly entirely lost (Fig. 2.8C). It is therefore quite possible that loss of productive interactions with SwIII mediated by the α6 region are responsible for the inability of some RGS subfamilies to recognize $G\alpha_q$. However, due to the poor sequence conservation and conformational heterogeneity of this region in R12 family members (R12 subfamily members also have a 1-residue deletion in the α6 helical region), it is not possible to easily test this hypothesis because conversion of SwIII contacts in RGS8 to those found in RGS10, and vice versa, is not possible by simple substitution.

One possible strategy would be to mutate the F125 and R128 positions of RGS8 to alanines. This would eliminate the stacking interacting from phenylalanine and the hydrogen bond formed by the arginine, thus decreasing the α6 interactions. If the mutations did effect a loss of $G\alpha_q$ binding in RGS8, then the model would be supported, but this test relies on a negative result and this could also be argued to be due to other factors, such as destabilization of the mutated RGS protein, which may also lead to a decrease in binding.

This model does not however explain how RGS proteins in the R7 and R12 subfamilies still retain activity for $G\alpha_i$ if they fail to make productive interactions with SwIII. These subfamilies may have optimized interactions with $G\alpha_{i/o}$ in other contact regions (e.g. αA and the Gα α-helical domain). This hypothesis is supported by increased GAP activity observed for RGS8 variants that have RGS10 substitutions in α7, and decreased GAP activity for RGS10 variants with RGS8 substitutions (Table 2.2). Previous studies have probed positions at this interface and also shown them to modulate RGS domain interactions and GAP activity for one Gα subfamily (45, 55, 60). Another possible explanation might be found in the SwI interface. $G\alpha_q$ has Pro185 whereas $G\alpha_i$ has Lys180. The $G\alpha_i$-Lys180 side chain buries more surface area with the RGS protein compared to Pro185 in $G\alpha_q$. Hence, if the interactions with SwIII are not strong, RGS proteins may be less active against $G\alpha_q$ as a result of also losing buried surface area with SwI. Indeed the specific activity of RGS4 is ~10 times lower than wild-type when using the

$G\alpha_i$-K180P variant as a substrate (61). Inversely, AlF_4^--activated $G\alpha_q$-P185K can be pulled-down by RGS2 in significantly greater amounts than wild-type $G\alpha_q$ (60).

In summary, the rules that dictate RGS domain selectivity for a given Gα subunit are complex. They involve leveraging beneficial versus negative interactions at different points of contact with the Gα subunits, as well as the ability of individual RGS proteins to undergo induced fit when required (45). However, the structure-function analysis reported here still points to the SwI and III interactions as being the key determinants of selectivity for $G\alpha_i$ versus $G\alpha_q$. Interactions with the α-helical domain can tune GAP activity (such as for RGS9 in the $G\alpha_{i/o}$ subfamily) or can even rescue RGS2 from loss of activity when it binds to $G\alpha_q$ (45). How is selectivity achieved for or against other Gα subfamilies? $G\alpha_s$ is not a substrate for any known RGS protein due to presence of Asp229 in SwII (Ser in $G\alpha_i$ and $G\alpha_q$) (41). $G\alpha_z$, a $G\alpha_{i/o}$ subfamily member, is the preferred substrate for RZ subfamily member RGS20, but the mechanism for this selectivity is unknown (62). A full understanding of the intricacies of how RGS proteins interact with Gα subunits is required if one seeks to design an RGS domain specific to a particular Gα subunit, or, conversely, a Gα subunit that is a specific substrate for a select subgroup of RGS proteins. Such would serve as useful tools to decipher the roles of individual RGS proteins in cellular signaling.

Chapter 3

Structure and Function of the $G\alpha_q$ Effector p63RhoGEF

Introduction

The canonical effector of the $G\alpha_{q/11}$ subunit family is PLCβ, but it has now been established that $G\alpha_{q/11}$ can also regulate several RhoGEFs. While it had been known since 1995 that GPCR signaling to Rho could be achieved through $G\alpha_{12/13}$ activation (63), it wasn't for another several years that $G\alpha_{q/11}$ was also linked to Rho signaling (64, 65). Today we know that at least three RhoGEFs are directly regulated by the $G\alpha_{q/11}$ family: p63RhoGEF, Trio and Kalirin (Duet) (Fig 3.1). They each contain a closely related DH/PH tandem motif activated by $G\alpha_q$, but the rest of their architecture differs.

The DH domain is responsible for the GEF activity of Dbl family members. The core of the α-helical DH domain consists of three regions (α1, α2 and α5) of highest sequence conservation (66). Two of these regions, α1 and α5, contact the Rho GTPase, particularly in its switch regions. The third region, α2, is opposite of the GTPase and appears to help stabilize the DH core (66). SwI (RhoA residues 29-40) and SwII (RhoA residues 59-77) are typically disordered until they bind GTP•Mg^{2+} (5). The rearrangement of a "catalytic" glutamine (RhoA Gln 63) must also occur for hydrolysis of GTP to GDP to proceed. The Dbl RhoGEF domain binds Rho in a conformation that discourages GDP binding by manipulating SwI to block the Mg^{2+} binding site (5). This allows GTP, which is in excess inside the cell, to bind in the now solvent exposed binding site. Several conserved residues in Dbl RhoGEF DH domains therefore must make contacts with the switch regions to cause this (p63RhoGEF residues Glu167 and Lys 297 with SwI, Asn334 with SwII) (5). Additionally, SwII of the GTPase contains conserved hydrophobic residues that allow it to nest into a complementary hydrophobic patch of the DH domain (5).

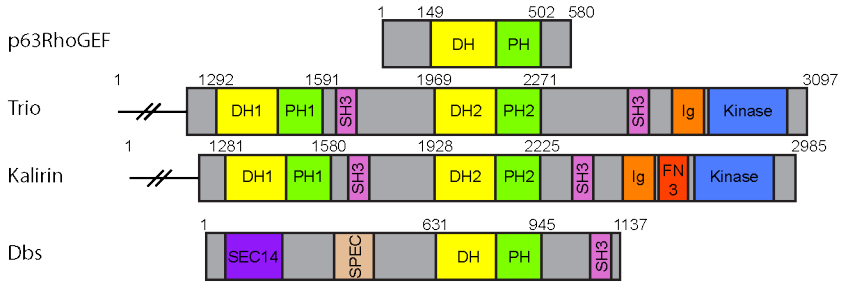

Figure 3.1 Dbl RhoGEFs. Shown is domain structure of $G\alpha_q$-regulated RhoGEFs and Dbs, the Dbl family member of highest homology from those of known structure. Lengths are to scale. Residue numbers are written above each map to indicate the beginning and end of each DH/PH tandem as well as the overall protein.

Almost all Dbl family members contain a PH domain directly C-terminal to the DH domain, and the role of this PH domain varies. In some family members, the PH domain is activating, such as in Dbs and the N-terminal DH/PH tandem of Trio (66, 67). In these RhoGEFs, the DH domain has lower activity when isolated, and exhibits higher nucleotide exchange activity on Rho when followed by the PH domain. It has been shown that this is due to contacts formed between the PH domain and the GTPase, therefore making the PH domain necessary for full binding ability and activity (66, 68). In other Dbl family members, the DH domain has low activity in the context of the full protein until becoming activated. This is true for members such as intersectin-1L and Vav1. The DH/PH tandem of intersectin-1L is similar to Dbs in that the DH domain has lower activity when isolated than in the tandem (69, 70). On the other hand, the full-length protein also has lower activity than the tandem (69, 70). This is because an SH3 domain N-terminal to the DH/PH tandem binds to the DH domain to inhibit it in the full protein (70). In Vav1, an acidic region N-terminal to the tandem binds to the DH domain in an analogous mechanism (71, 72). To further complicate manners in Vav1, a calponin homology domain N-terminal to the tandem binds to the PH domain as an additional autoinhibition mechanism (73). In yet another autoinhibitory mechanism, the Dbl family member Sos is autoinhibited by direct interactions between its PH and DH domains that prevent RhoA binding (74). Lastly, some PH domains appear to have little effect on the ability of the DH domain to serve as a GEF, and therefore are not required for the activity. One example is the $G\alpha_{12/13}$ activated RhoGEF named LARG. The DH domain of LARG shows little change in exchange activity compared to the DH/PH tandem *in vitro*(75). One also cannot forget to mention Tuba, the only known Dbl family member without a PH domain (76). Outside of the

Dbl family, PH domains are often regarded as phospholipid binding domains (77). However, phosphoinositide binding to the PH domain only plays a significant role in the activation of a few Dbl family members (78, 79). All of this shows that regulation of DH domains, either by their adjoining PH domains or other domains in the protein, is highly variable and the mechanism that is occurring cannot always be predicted from the structure of the tandem alone.

In p63RhoGEF, there are no known additional domains outside of the DH/PH tandem (Fig 3.1). This tandem has been found to be selective for RhoA, RhoB and RhoC (80-82). Structure prediction for the regions N- and C-terminal to the tandem also suggests no other secondary topology except for a conserved extension of the PH domain shared by p63RhoGEF, Trio and Kalirin (82). This extension has been found necessary for direct binding to and activation by $G\alpha_q$ (82, 83). It has also been shown that p63RhoGEF contains three cysteines at its N-terminus (Cys23, 25, 26) that are palmitoylated to target the protein constitutively to the plasma membrane (84). A splice variant of p63RhoGEF, called GEFT, has also been described in the literature (81, 85). It was originally identified to be specific for Rac and Cdc42 (85), although more convincing studies now show it to be Rho specific (81). Because GEFT is missing the first 106 amino acids present in p63RhoGEF, including the palmitoylation sites, it is localized to the cytoplasm of the cell (86). Mutations in p63RhoGEF that block its ability to be palmitoylated also can cause it to localize to the cytoplasm, and the isolated C-terminal DH/PH tandem of Trio has no preference for the membrane (67, 84). Altogether, this evidence indicates that the PH domain in this DH/PH family plays no role in localizing the protein to the membrane.

Compared to p63RhoGEF, Trio and Kalirin are more complex in their domain make-up (Fig 3.1). Both Trio and Kalirin contain an additional DH/PH tandem located N-terminal to the one bearing high homology to p63RhoGEF. These additional tandems exhibit high homology between each other and are specific for Rac1 and RhoG (67, 87). The N-terminal DH/PH employs a mechanism where both the DH and PH domains interact with the GTPase to activate it in a manner analogous to Dbs (68). This N-terminal tandem is not known to be regulated by a G protein. Both N- and C-terminal tandems in Trio and Kalirin have an SH3 domain downstream of them, with the second SH3 domain also being followed by an immunglobulin-like (Ig-like) domain. A putative protein kinase domain is located near the C-terminus in both proteins. Kalirin is unique from Trio in that it contains a fibronectin III domain between the Ig-like and kinase domains. The simplicity of p63RhoGEF in comparison to Trio and Kalirin makes it an ideal

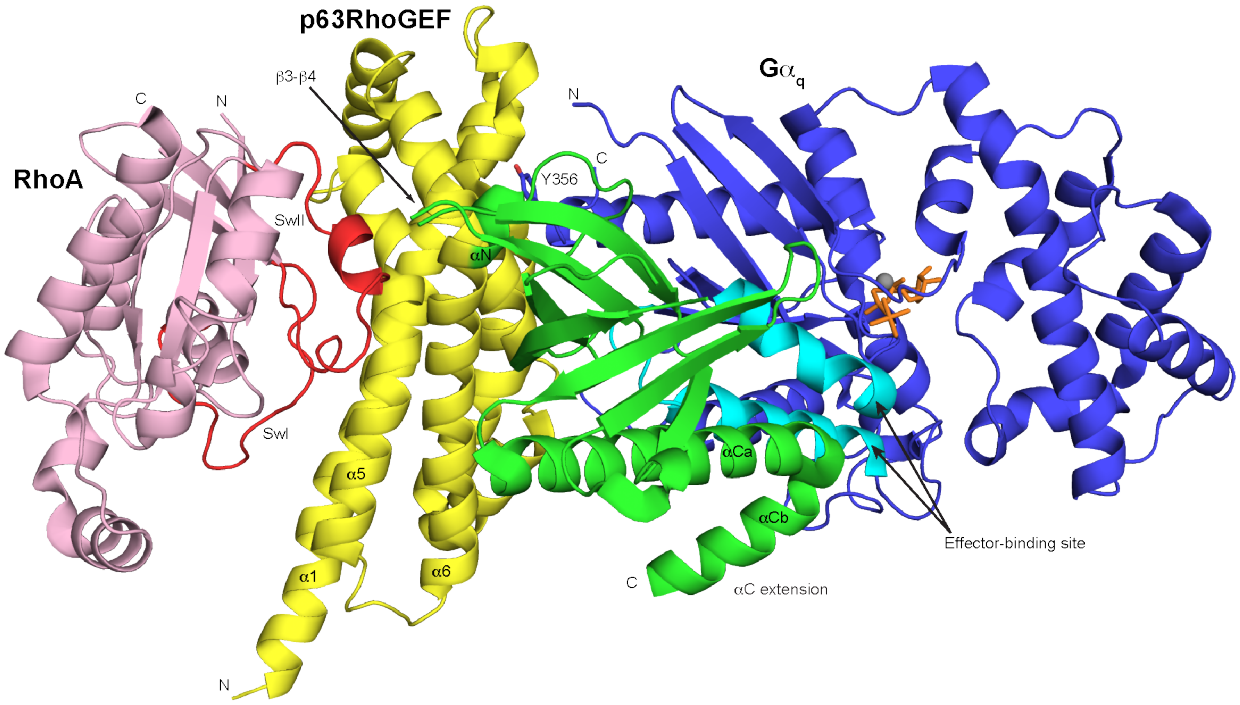

Figure 3.2 Crystal structure of the RhoA–p63RhoGEF–$G\alpha_q$ complex (2RGN). $G\alpha_q$ (blue) is activated by GDP–AlF_4 (orange sticks) and Mg^{2+} (gray sphere). The effector-binding site of $G\alpha_q$ (light blue) interacts the αC helix and extension of the PH domain of p63RhoGEF (green). It interacts with the DH domain of p63RhoGEF (yellow) using Tyr356. The DH domain contacts primarily the switch regions (red) of RhoA (pink). N- and C-termini are denoted N and C, respectively.

model for characterizing how the $G\alpha_{q/11}$ family interacts with these GEFs, and the high sequence identity in the DH/PH tandem (~60%) between the three RhoGEFs, as well as biochemical data, suggests that the activation mechanism will be similar for all three (67).

The ternary complex of the DH/PH tandem of p63RhoGEF in complex with aluminum fluoride-activated $G\alpha_q$ and apo-RhoA was previously solved to 3.5Å using x-ray crystallography (Fig 3.2) (83). From this structure it was observed that the DH/PH tandem of p63RhoGEF exhibits a typical overall fold. The DH domain bridges RhoA and $G\alpha_q$ in the ternary complex, and is the only domain to make contacts with RhoA. Mutational analysis shows that various residues on α2 and α3 of the DH domain are important for binding to and activation by $G\alpha_q$ (83). These residues mainly contact the α4-β6 and α3-β5 loop of $G\alpha_q$, as well as its C-terminus. Although the PH domain makes no contacts with RhoA in the active conformation, it does make extensive contacts with Gα. The C-terminal helix (αCα) of the PH domain and the conserved extension (αCβ) that is found in $G\alpha_q$-interacting RhoGEFs are used to bind the effector-binding

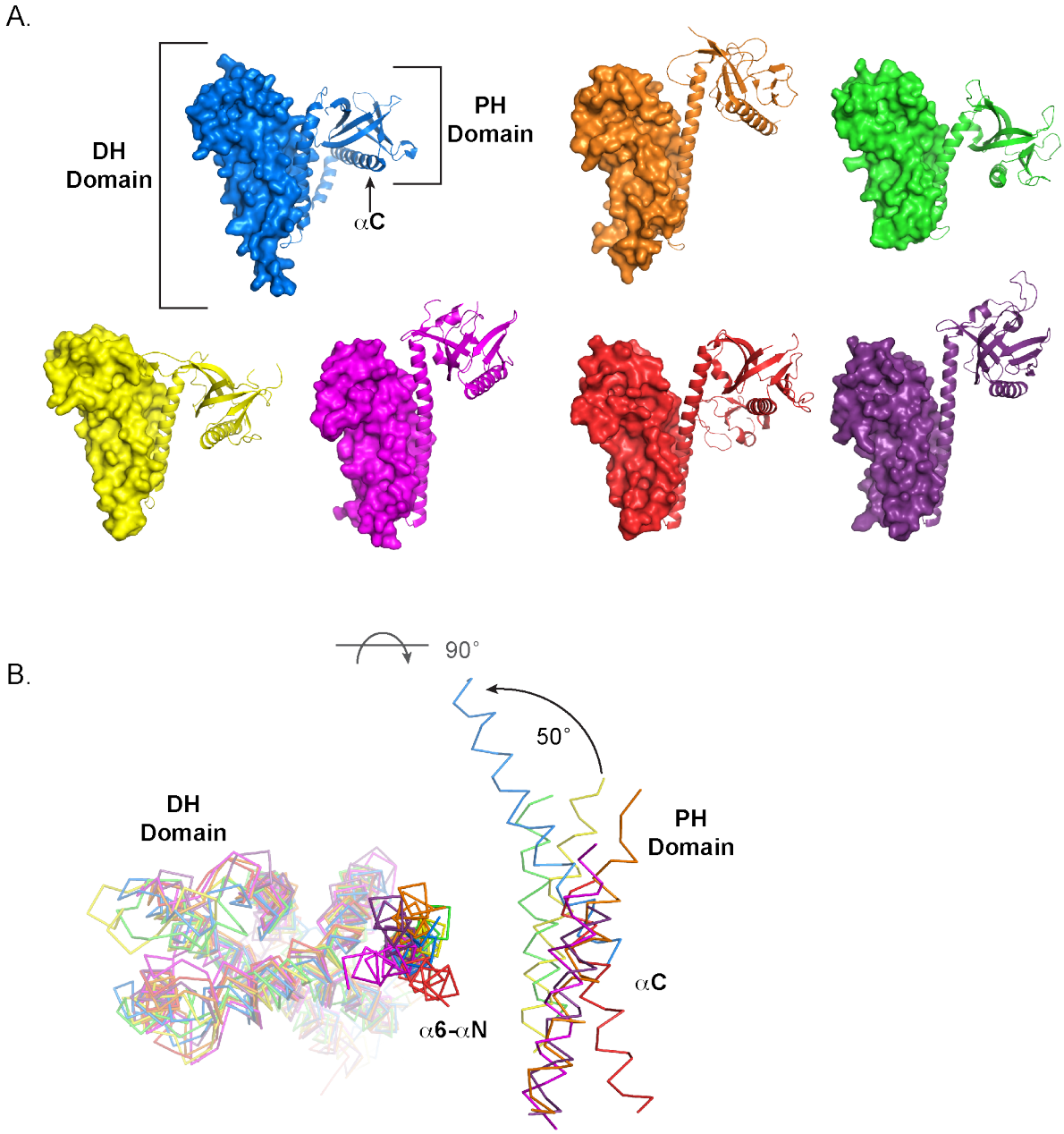

Figure 3.3 Variability in the α6-αN linker among Dbl family RhoGEFs. *A*, The DH/PH tandems of p63RhoGEF (2RGN, blue), Dbs (1LB1, yellow), LARG (1TXD, magenta), Vav1 (3KY9, red), N-terminal tandem of Trio (1NTY, green), p115RhoGEF (3ODO, purple), and intersectin (1KI1, orange) were arrayed for comparison. The DH domain is represented by a surface except for its α6 helix. A bend is often seen in the α6-αN helix. The PH domains can be displaced in an upward or downward direction. *B*, The PH domain in p63RhoGEF is rotated 50˚ away from that of Dbs. The DH domains of structures above were superimposed. For clarity, only the αN and αC helices are shown of the PH domain. The αC helix of p63RhoGEF is at a unique angle compared to other Dbl family members.

site of $G\alpha_q$ (83). Mutations in the PH domain extension at this interface are more detrimental to $G\alpha_q$ binding and activation than mutations in either the DH domain or core PH domain, underscoring the importance of this extension for activation (83). Nevertheless, full activation by $G\alpha_q$ requires the formation of interactions with both the DH and PH domains (88).

It has been shown that the DH/PH tandem of p63RhoGEF is autoinhibited, and that direct interaction with activated $G\alpha_q$ relieves this inhibition, allowing it to exchange nucleotide on Rho (83, 88, 89). While the exchange activity of the tandem increases by ~20-fold with the addition of activated $G\alpha_q$, the isolated DH domain of p63RhoGEF surprisingly exhibits ~45-fold greater exchange activity than the tandem (88). It is clear that the PH domain has no activating properties from this data, and thus cannot be functioning in a mechanism analogous to Dbs. When added *in trans*, the PH domain also does not inhibit the DH domain, thus ruling against a Sos-like mechanism of direct interaction between the two (88). Because the tandem shows similar levels of Rho activation in cells by western blot and also binding affinity to $G\alpha_q$ compared to longer variants of p63RhoGEF, it is assumed that the tandem is the smallest unit needed for full autoinhibition and GEF activity (83). Definitive tests of this point have previously not been feasible due to the inability to purify a full-length version of p63RhoGEF. However, it is unlikely that autoinhibition is primarily achieved through an element outside of the tandem. Because of these observations, it appears that p63RhoGEF is autoinhibited in a manner unlike any other previously described for Dbl family members.

To gain insight into the mechanism of p63RhoGEF regulation, the structure of its tandem was compared to those of other Dbl family members (Fig 3.3A-B). The most obvious difference is the position of the DH and PH domains with respect to each other. When the DH domains are superimposed, the entire PH domain of active p63RhoGEF is rotated around the long axis of the α6-αN helix, farther away from the DH domain. For example, the PH domain of p63RhoGEF is rotated approximately 50˚ more compared to the PH domain of Dbs, the Dbl family member with the highest primary sequence homology to p63RhoGEF among those of known structure (83). The same trend is seen with other Dbl family members of more distant relation to p63RhoGEF. It appears that the rotation of the PH domain of p63RhoGEF is at an extreme among known structures. It has been hypothesized that the DH/PH tandem of p63RhoGEF adopts a more typical rotational conformation in its basal state, but a difference in sequence in residues near the GTPase interaction surface results in an inability for RhoA to bind (83, 88). When $G\alpha_q$ binds to

the two domains, it pulls the PH domain around the α6-αN helix, and these inhibitory residues rotate away from the RhoA interaction surface to allow the GTPase to bind. The α6-αN region could therefore be the allosterical link between the PH domain and switch regions of Rho. In support of this, the structure of Dbs reveals that it uses residues in its α6-αN linker to contact the GTPase (1LB1). It is important to mention that Dbs only shares ~34% identity with p63RhoGEF in the DH/PH tandem and that Dbs differs from p63RhoGEF in several key aspects, such as having additional specificity for Cdc42 and possession of a PH domain that is activating in the context of the tandem (66, 90). The fact that the PH domain of Dbs works in an opposite fashion to that of p63RhoGEF is fortuitous, as it stands to reason that any differences between the two in the α6-αN linker region could be determinants of an inhibitory or activating mechanism by the PH domain. Several residues fitting this criteria were identified, but only two were found to increase the ability of basal p63RhoGEF to exchange nucleotide on RhoA when mutated to the residue found in Dbs (88). These residues were Gly340 and Arg341, located in the αN helix of the PH domain.

Comparison of a variety of Dbl RhoGEF DH/PH tandem structures also shows a pattern of bending in the α6-αN helix (Fig. 3.3A). The bend occurs at the end of α6 and varies in direction depending on the RhoGEF. The high variability in the angle of the helix among structures could be indicating that this helix is dynamic, but inspection of crystal structure B-factors is inconclusive. Attempts to crystallize the DH/PH tandem of p63RhoGEF have been unsuccessful, which may be explained by this proposed flexibility. Therefore, an alternative mechanism of activation is that the α6-αN helix exhibits increased dynamics when alone that impede interaction with RhoA until $G\alpha_q$ binds to, and stabilizes, an orientation that promotes RhoA interaction.

In order to determine how the DH/PH tandem of p63RhoGEF is autoinhibited, it is clear that a structure of basal, inactive p63RhoGEF for comparison with the active conformation would be most informative. Because attempts to crystallize the DH/PH tandem have been unsuccessful, NMR and SAXS were used in an attempt to determine the angle of the PH domain with respect to the DH domain in solution. In the event that these experiments show that a change in orientation between the two domains does not occur, investigations into the dynamics of the DH/PH, particularly in the linker region, were also performed using molecular dynamics.

These experiments should be sufficient to explain this new mode of regulation in a Dbl family RhoGEF and provide for a more complete understanding of $G\alpha_q$ signaling.

Methods

Expression Vectors

Expression of human p63RhoGEF variants in *E. coli* cells used the vectors $pMalC_2H_{10}T$ or pMCSG9 (Table 3.1). Both vectors express N-terminal MBP (maltose-binding protein) fusions, with a TEV (tobacco etch virus) protease cleavage site inserted between the MBP and protein of interest. The MBP contains an N-terminal 6xHis tag in pMCSG9, and a C-terminal 6xHis tag (before the cleavage site) in $pMalC_2H_{10}T$. Constructs of the p63RhoGEF full DH domain (residues 149-338), full PH domain (residues 334-502) and truncated PH domain (residues 334-470) were made in the $pMalC_2H_{10}T$ vector, leaving exogenous N-terminal residues GEFM after TEV cleavage. QuikChange mutagenesis was used to make C-terminal DH domain truncations [149-335, 149-337 (M336S)]. Full DH domain constructs containing an N-terminal 6xHis tag or 5xArg tag were also made, both containing the preceding exogenous residue G after TEV cleavage. An additional PH domain construct (residues 351-502) was made in pMCSG9. The full p63RhoGEF DH/PH tandem (residues 149-502) and the C-terminally truncated tandem (residues 149-470) were also expressed using pMCSG9, leaving exogenous N-terminal residues SNA after TEV cleavage. Single point mutants of the truncated tandem (R160A, E184A, Y220A, P330A or R341A) were prepared using QuikChange on the truncated tandem. A double mutant (V250C, T351C) was made using QuikChange on the full tandem. Constructs of p63RhoGEF containing the N-terminus (residues 1-502 or 1-580) had the palmitoylation sites mutated (C23/25/26S, designated $palm^-$) and were expressed in $pMalC_2H_{10}T$ with the N-terminal exogenous residues GEFGSSRVD remaining after TEV cleavage. QuikChange was used on these vectors to remove a peptide sequence spanning L121-L128 (LTLLTTLL).
All protein expression in insect cells used the vector pFastBac HT (Table 2.1), which expresses proteins with an N-terminal 6xHis tag that is cleavable by TEV protease. These constructs include p63RhoGEF variants containing residues 67-580, 67-502, 33-502, 1-580 (C23/25/26S) with and without residues 121-128, 1-502 (C23/25/26S) with and without residues 121-128, and 149-502. All contain N-terminal exogenous residues GAMGIRNSKAYVDM after TEV cleavage.

Full-length *Mus musculus* $G\alpha_q$ (residues 7-359) and an N-terminally truncated variant of *Mus musculus* $G\alpha_q$ (residues 35-359) were expressed using pFastBac HT. N-terminal exogenous residues after TEV cleavage are GA.

Human RhoA (residues 1-193) was expressed using the $pMalC_2H_{10}T$ vector, leaving exogenous residues GEF after TEV cleavage.

Expression of p63RhoGEF and Variants

Unlabeled p63RhoGEF was grown in Rosetta (DE3) cells by picking ~5 single colonies from a plate of freshly transformed cells and adding to 50 mL LB Miller broth containing 50 mg/L carbenicillin. This culture was shaken at ~215 rpm at 37˚C overnight. Then 10 mL of this culture was added to 1 liter of Terrific Broth.

Minimal media expression of labeled p63RhoGEF was started by picking 5 colonies from a plate of freshly transformed Rosetta (DE3) cells and adding to 50 ml of LB Miller Broth containing 50 mg/L carbenicillin. This culture was shaken at ~215 rpm at 37˚C until cells reached log phase growth (OD_{600} = 0.4-0.7). Cells were then centrifuged at 1800 × *g* for 10

																	Vector		
Exogenous Residues	1	33	67	120	121	129	149	334	335	337	338	351	470	502	580	Point Mutations	pMCSG9	pMalC2H10T	pFastBac HT
GEFM							x	x	x	x	x							x	
GEFM								x	x	x	x	x	x	x				x	
GEFM								x	x	x	x	x	x					x	
GEFM							x	x	x									x	
GEFM							x	x	x	x						M336S		x	
HHHHHHN							x	x	x	x	x							x	
RRRRRN							x	x	x	x	x							x	
SNA												x	x	x			x		
SNA							x	x	x	x	x	x	x	x			x		
SNA							x	x	x	x	x	x	x				x		
SNA							x	x	x	x	x	x	x			R160A	x		
SNA							x	x	x	x	x	x	x			E184A	x		
SNA							x	x	x	x	x	x	x			Y220A	x		
SNA							x	x	x	x	x	x	x			P330A	x		
SNA							x	x	x	x	x	x	x			R341A	x		
SNA							x	x	x	x	x	x	x	x		V250C,T351C	x		
GEFGSSRVD	x	x	x	x	x	x	x	x	x	x	x	x	x	x		C23/25/26S		x	
GEFGSSRVD	x	x	x	x	x	x	x	x	x	x	x	x	x	x	x	C23/25/26S		x	
GEFGSSRVD	x	x	x	x		x	x	x	x	x	x	x	x	x		C23/25/26S		x	
GEFGSSRVD	x	x	x	x		x	x	x	x	x	x	x	x	x	x	C23/25/26S		x	
GAMGIRNSKAYVDM			x	x	x	x	x	x	x	x	x	x	x	x	x				x
GAMGIRNSKAYVDM			x	x	x	x	x	x	x	x	x	x	x	x					x
GAMGIRNSKAYVDM		x	x	x	x	x	x	x	x	x	x	x	x	x					x
GAMGIRNSKAYVDM	x	x	x	x	x	x	x	x	x	x	x	x	x	x		C23/25/26S			x
GAMGIRNSKAYVDM	x	x	x	x	x	x	x	x	x	x	x	x	x	x	x	C23/25/26S			x
GAMGIRNSKAYVDM	x	x	x	x		x	x	x	x	x	x	x	x	x		C23/25/26S			x
GAMGIRNSKAYVDM	x	x	x	x		x	x	x	x	x	x	x	x	x	x	C23/25/26S			x
GAMGIRNSKAYVDM							x	x	x	x	x	x	x	x					x

Table 3.1 Constructs of p63RhoGEF variants for bacterial and insect cell expression. Each row represents a separate construct. Numbered column headers are residue numbers in p63RhoGEF. Exogenous N-terminal residues are denoted in the first column, and point mutation locations are denoted in the last white column. Blue shaded columns indicate the expression vector used. Yellow shaded boxes denote that the residue signified in the construct was included in the construct.

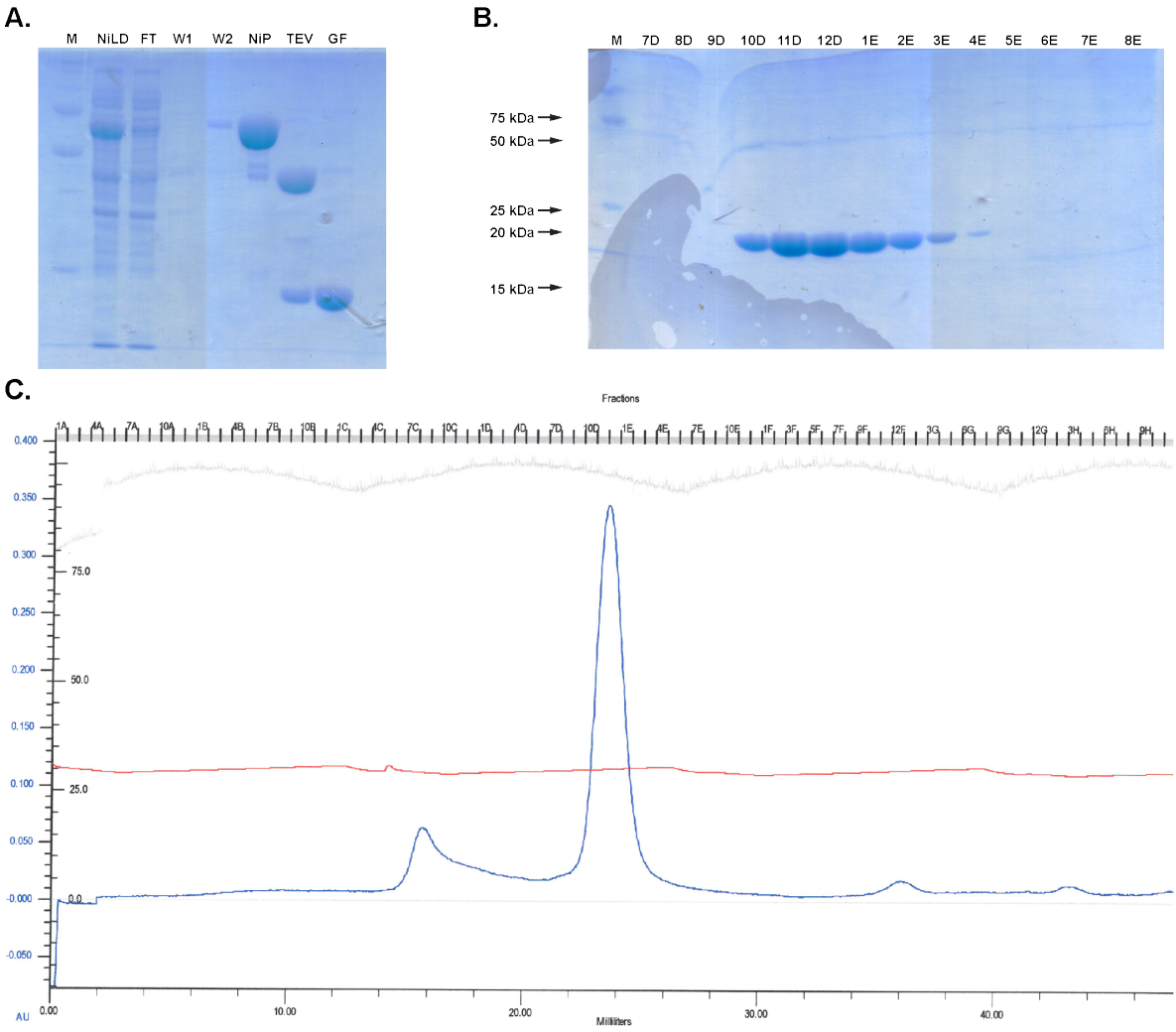

Figure 3.4 Purification of the DH domain of p63RhoGEF. *A*, SDS-PAGE gel containing fractions taken during purification. M, size marker; NiLD, lysate flowed over Ni-NTA column; FT, column flow through from lysate; W1 and W2, first and second wash flow throughs, respectively; NiP, final eluted fraction from column; TEV, sample after cleavage with TEV protease; GF, concentrated sample loaded onto size exclusion chromatography. *B*, SDS-PAGE gel containing fractions from size exclusion chromatography. Numbers correspond to chromatogram. *C*, Chromatogram from tandem S75 size exclusion columns. Blue is the UV-Vis trace, red is conductivity.

minutes. The supernatant was discarded and the cells resuspended in 300 mL of unlabeled M9 medium. M9 medium was prepared by autoclaving 8 g/L Na_2HPO_4, 4 g/L KH_2PO_4 and 0.5 g/L NaCl in water, and then adding 0.3 mM Na_2SO_4, 1 mg/L biotin, 1 mg/L thiamine, 1 mM $MgSO_4$, 0.3 mM $CaCl_2$, 1 g/L $(NH_4)_2SO_4$, 5g/L glucose, and 50 mg/L carbenicillin. This culture was shaken until log phase growth, then centrifuged and resuspended in 500 mL of M9 using labeled ingredients substituted for any unlabeled ingredients as needed. For 15N labeling, $^{15}(NH_4)_2SO_4$

or $^{15}NH_4Cl$ was used in place of $(NH_4)_2SO_4$. For ^{13}C labeling, either D-Glucose (U-$^{13}C_6$) for non-deuterated samples or D-Glucose (U-$^{13}C_6$; 1,2,3,4,5,6,6-D_7) for deuterated samples was used. Deuterated samples used D_2O in place of water for the labeled M9 medium and were filtered with a 0.2 μM filter after all ingredients were added instead of autoclaving.

All final *E. coli* cultures were allowed to grow until OD_{600} = ~0.9-1.0 before inducing with 0.2 mM IPTG. Cultures were then transferred to 20˚C before continuing to shake at 250 rpm for 16 hours. Cultures were then spun down at 3500 × *g* for 17 minutes. The supernatant was discarded and the pellets frozen and stored at -80˚C.

Expression of p63RhoGEF in High 5 cells used the insect cell vector pFastBacHT expressing p63RhoGEF. Constructs included residues 149-502, 149-580, 1-502, 1-580 and 67-502. Constructs including the N-terminus were mutated to C23/25/26S to eliminate palmitoylation. For purification, 6 liters of High Five™ cells (BTI-TN-5B1-4) expressing p63RhoGEF were pelleted at 3000 × *g* for 20 min.

Purification of p63RhoGEF and Variants

Cells were homogenized using a Dounce in Lysis Buffer (20 mM HEPES, pH 8.0, 150 mM NaCl, 0.1 mM EDTA, 10 mM β-mercaptoethanol, 7.6 μM leupeptin, 360 nM lima bean trypsin inhibitor, and 1 mM PMSF). Cells were then lysed using an EmulsiFlex-C3 homogenizer (Avestin). Cell debris was pelleted by centrifugation for 1 hour at 40,000 rpm (185,500 g) in a Type 45 Ti fixed angle rotor (Beckman-Coulter). Resulting supernatant was glass filtered and incubated for 1 hour at 4˚C on a rocker plate with 5 mL Ni-NTA affinity column resin pre-equilibrated with Wash 1 Buffer (20 mM HEPES, pH 8.0, 150 mM NaCl, 10 mM β-mercaptoethanol). The column was then flipped upright and the resin allowed to settle before slowly draining. The column was then washed with 100 mL of Wash 1 Buffer. The column was then washed with 100 mL of Wash 2 Buffer (20 mM HEPES, pH 8.0, 300 mM NaCl, 10 mM β-mercaptoethanol), followed by 100 mL of Wash 3 Buffer (20 mM HEPES, pH 8.0, 300 mM NaCl, 10 mM β-mercaptoethanol, 10 mM imidazole). The column was eluted using 25 mL of Elution Buffer (20 mM HEPES, pH 8.0, 150 mM NaCl, 10 mM β-mercaptoethanol, 200 mM imidazole). Protein was cleaved with 1-2% (w/w) TEV protease overnight while being dialyzed in 2 liters Dialysis Buffer (20 mM HEPES, pH 8.0, 150 mM NaCl, 1 mM DTT). The protein was then incubated for 1 hour at 4˚C on a rocker plate with 5-mL Ni-NTA affinity column resin pre-

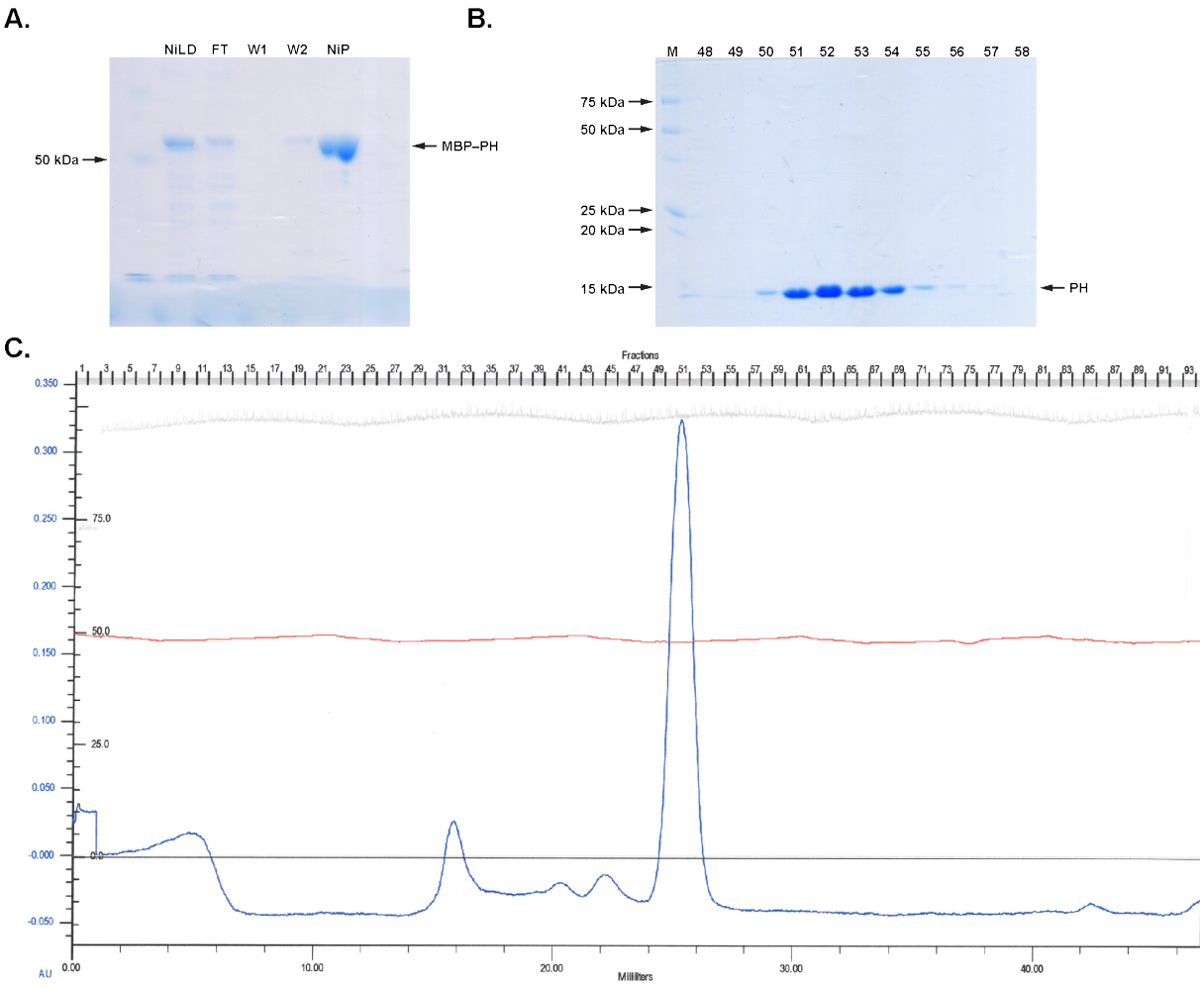

Figure 3.5 Purification of the PH domain of p63RhoGEF. *A*, SDS-PAGE gel containing fractions taken during purification. M, size marker; NiLD, lysate flowed over Ni-NTA column; FT, column flow through from lysate; W1 and W2, first and second wash flow throughs, respectively; NiP, final eluted fraction from column. *B*, SDS-PAGE gel containing fractions from size exclusion chromatography. Numbers correspond to chromatogram. *C*, Chromatogram from tandem S75 size exclusion columns. Blue is the UV-Vis trace, red is conductivity.

equilibrated with dialysis buffer. Resin was allowed to settle again as in the first column and then slowly eluted (Figs. 3.4A, 3.5A, 3.6A). The final flow through was then concentrated to 1 mL and flown over tandem Superdex 75 (single domain) or Superdex 200 (tandem domains) 10/300 GL (GE Life Sciences) gel filtration columns pre-equilibrated with Gel Filtration Buffer (20 mM HEPES, pH 8.0, 150 mM NaCl, 2 mM DTT). The eluted protein was monitored by UV-Vis absorbance and collected in 0.5 mL fractions (Figs. 3.4C, 3.5C, 3.6C). Fractions containing the

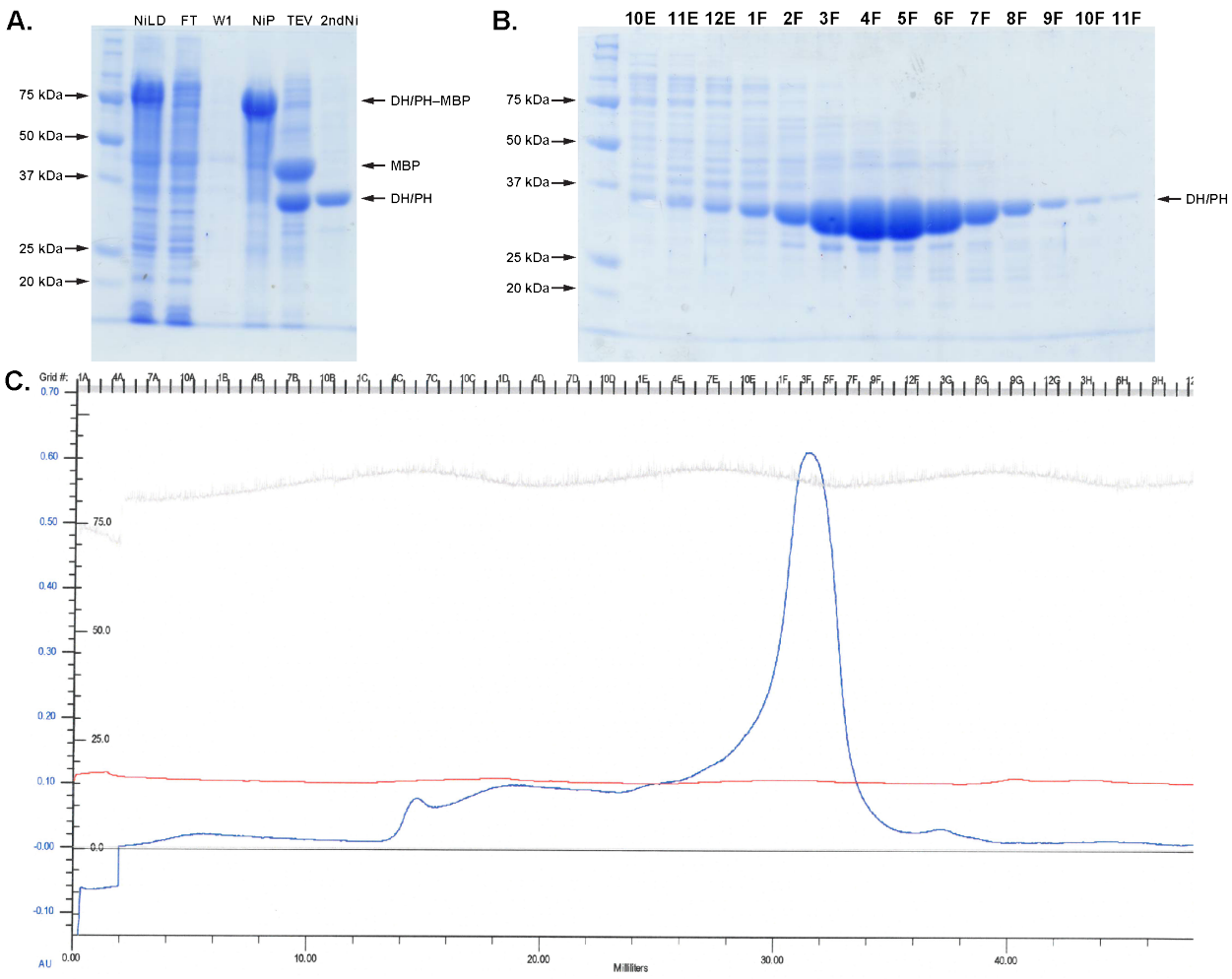

Figure 3.6 Purification of the DH/PH domain of p63RhoGEF. *A*, SDS-PAGE gel containing fractions taken during purification. M, size marker; NiLD, lysate flowed over Ni-NTA column; FT, column flow through from lysate; W1, first wash flow through; NiP, final eluted fraction from column; TEV, sample after cleavage with TEV protease; 2ndNi, eluted protein from second Ni-NTA column. *B*, SDS-PAGE gel containing fractions from size exclusion chromatography. Numbers correspond to chromatogram. *C*, Chromatogram from tandem S200 size exclusion columns. Blue is the UV-Vis trace, red is conductivity.

desired protein were determined using SDS-PAGE (Figs. 3.4B, 3.5B, 3.6B) and pooled before concentrating to 5-10 mg/mL using Amicon® Ultra 4 mL or 15 mL centrifugal filters.

Expression and Purification of Other Proteins

Full length $G\alpha_q$ (residues 7-359) was expressed and purified as previously described (Lyon 2011). The N-terminally truncated variant of $G\alpha_q$ (residues 35-359) was expressed and purified as previously described (48).

RhoA was expressed and purified as previously described (83).

Full length $G\alpha_q$ was purified by homogenizing cells as stated in Lysis Buffer (20 mM HEPES, pH 8.0, 100 mM NaCl, 10 mM β-mercaptoethanol, 7.6 μM leupeptin, 360 nM lima bean trypsin inhibitor, 1 mM PMSF, 0.1 mM EDTA, 3 mM $MgCl_2$, and 10 μM GDP, pH 8.0). It was then either lysed by sonication (50 times for 1 second) or lysed as above. Cell debris was pelleted and the supernatant filtered as stated above. It was flowed over a 5 mL Ni-NTA affinity column pre-equilibrated with Wash 1 Buffer (20 mM HEPES, pH 8.0, 100 mM NaCl, 10 mM β-mercaptoethanol, 1 mM $MgCl_2$, and 10 μM GDP, pH 8.0). The column was then washed with Wash 1 Buffer. Following that, the column was washed with Wash 2 Buffer (20 mM HEPES, pH 8.0, 300 mM NaCl, 10 mM β-mercaptoethanol, 1 mM $MgCl_2$, 10 μM GDP, pH 8.0, and 10 mM imidazole). The column was eluted with 25 mL Elution Buffer (20 mM HEPES, pH 8.0, 100 mM NaCl, 10 mM β-mercaptoethanol, 1 mM $MgCl_2$, 10 μM GDP, pH 8.0, and 150 mM imidazole). The protein concentration was determined using a Bradford assay. The elution was then diluted with 75 mL Low Salt Buffer (20 mM HEPES, pH 8.0, 1 mM DTT, 1 mM $MgCl_2$, 10 μM GDP, pH 8.0), passed through a 0.2 μM filter, and loaded onto a Mono Q 5/50 GL (GE Life Sciences) or an UNO Q anion exchange column (Bio-Rad). A 20 mL salt gradient into 500 mM NaCl was used, collecting 0.5 mL fractions. Fractions containing the protein were determined using SDS-PAGE, pooled and concentrated to 1 mL. This sample was then loaded onto tandem Superdex 200 10/300 GL (GE Life Sciences) gel filtration columns pre-equilibrated with Gel Filtration Buffer (20 mM HEPES, pH 8.0, 100 mM NaCl, 1 mM DTT, 1 mM $MgCl_2$, 10 μM GDP, pH 8.0). Protein was eluted using Gel Filtration Buffer into 0.5 mL fractions. Fractions containing protein were determined using SDS-PAGE and pooled for concentration to ~10 mg/mL.

Room Temperature Stability Studies

Stability studies were performed by concentrating and filtering protein to the desired concentration for NMR data collection. An initial aliquot was taken and mixed with SDS loading dye (final concentration 50 mM Tris-HCL pH 6.8, 100 mM DTT, 2% w/v SDS, 0.025% w/v bromophenol blue, 10% glycerol), denatured by heat and flash frozen at -80˚C. The remaining sample was then incubated at room temperature. Subsequent timepoints were taken in the same way as the initial aliquot and a final SDS-PAGE gel was used to assess protein degradation.

Flow Cytometry Protein Interaction Assays

Biotinylation of full-length $G\alpha_q$ and AlexaFluor labeling of GRK2 and p63RhoGEF variants were performed as previously described (83, 91). A 3:1 molar ratio of biotin to $G\alpha_q$ and a 2:1 ratio of biotin to p63RhoGEF variants was sufficient. A 3:1 molar ratio of amine to protein was used for AlexaFluor labeling of p63RhoGEF variants. Assays were performed as previously described (91), with some changes. Bead-coupling buffer was 20 mM HEPES pH 8.0, 100 mM NaCl, 10 mM MgCl2, 100 μM GDP, 0.1% Lubrol, 1% bovine serum albumin. Flow buffer was the same, except with the addition of 30 μM $AlCl_3$ and 10 mM NaF when activation was required. Plates were set up with 25 or 50 μL of beads coupled to $G\alpha_q$ added to 25 or 50 μL Flow buffer containing the proteins being tested, for total well volumes of 50 or 100 μL. Fluorescence was read using an Accuri C6 Flow Cytometer (BD Biosciences) equipped with a Intellicyt HyperCyt Autosampler plate reader (Agilent).

Formation of Complexes

Either p63RhoGEF 1-580 $palm^-$ or 1-502 $palm^-$ and full length $G\alpha_q$ were incubated together in the molar ratio 1.0:1.1 in Complex Buffer (20 mM HEPES, pH 8, 100 mM NaCl, 5 mM $MgCl_2$, 10 μM GDP, 10 mM NaF, 30 μM $AlCl_3$ and 2 mM DTT). The complex was incubated on ice for at least 30 minutes.

Ternary complexes were made similarly to previously described (83). Briefly, RhoA was incubated with 10 mM EDTA for 30 minutes before buffer exchanging into Gel Filtration Buffer (20 mM HEPES, pH 8.0, 100 mM NaCl, 1 mM DTT, 1 mM $MgCl_2$, 10 μM GDP, pH 8.0). A complex of p63RhoGEF and $G\alpha_q$ was buffer exchanged into Ternary Complex Buffer (20 mM HEPES, pH 8, 50 mM NaCl, 10 mM NaF, 30 μM $AlCl_3$ 1 μM EDTA, and 1 mM DTT). The RhoA was then added to this complex in a 1.25:1.0 molar ratio before incubating for 15 minutes on ice. The ternary complex was then isolated on tandem Superdex 200 10/300 GL (GE Life Sciences) gel filtration columns pre-equilibrated with Ternary Complex Buffer.

Complexes of DH domain of p63RhoGEF and RhoA were prepared as above, where the RhoA was added in excess to the DH domain before separation by size exclusion chromatography (Fig. 3.7A-B). The DH domain is 23 kDa and RhoA is 22 kDa. The DH domain migrates faster than RhoA on an SDS-PAGE gel (Fig 3.7C).

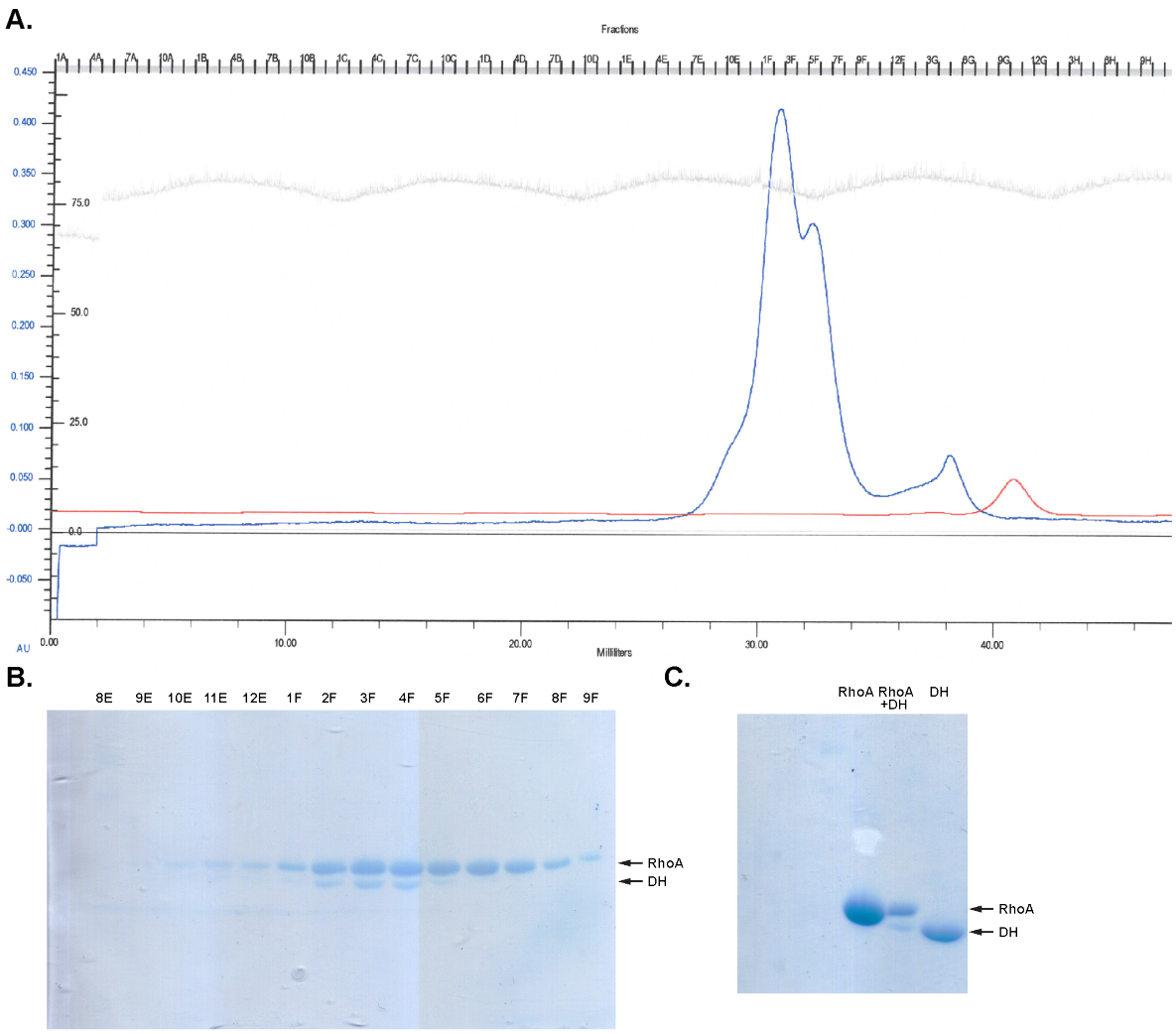

Figure 3.7 Formation of the DH-RhoA complex. *A*, Chromatogram of size exclusion chromatography purification of complex. *B*, SDS-PAGE gel of fractions from chromatography column. Numbers above lanes correspond to panel A. *C*, SDS-PAGE gel showing that the DH domain migrates faster than RhoA, even though its actual size is larger.

Differential Scanning Fluorimetry

Thermal denaturation assays were performed using differential scanning fluorimetry (DSF). In a total volume of 8 µL, 0.1 mg/mL protein and 0.1 mM 1-anilinonaphthalene-8-sulfonic acid (ANS) were diluted into ThermoFluor Buffer (20 mM HEPES, pH 8.0, 100 mM NaCl, 1 mM DTT, 10 µM GDP, 1 mM $MgCl_2$) containing 30 µM $AlCl_3$ and 10 mM NaF when AMF activation was required. Samples were measured in triplicate in black 384-well PCR plates (Thermo Scientific, AB-1384/K). The plate was centrifuged for 1 minute at 1000 g before adding 2 µL silicone oil to the top of each well. The plate was then centrifuged again at 1000 g for 1 minute before reading. An up/down cycle was used from 0 to 85˚C, advancing by 1˚ steps,

and holding the high temperature for 45 seconds and the low temperature for 30 seconds. Melting curves were analyzed by fitting to a Boltzmann model using ThermoFluor Acquire 3.0 software.

SAXS Sample Preparation and Data Collection

The DH domain (149-338), PH domain (334-470) and DH–PH tandem (149-470) were eluted from gel filtration column chromatography in 20 mM HEPES at pH 8.0, 2 mM DTT, and 300 mM NaCl (500 mM NaCl for PH domain). Sample concentrations of 1, 2.5 and 5 mg/mL were prepared using dilutions into excess gel filtration chromatography buffer. Excess chromatography buffer was used for SAXS background subtraction. Samples were centrifuged at 13,000 RPM (~16,000 g) at 10˚C for 20 minutes before data collection. X-ray scattering from the sample solutions was measured at 5-ID beamline (DuPont-Northwestern-Dow Collaborative Access Team, DND-CAT) at the Advanced Photon Source, Argonne National Laboratory. An x-ray beam of 9 keV energy (wavelength λ=1.3776 Å) was focused horizontally by a mirror and collimated vertically by three pinholes to a size of 250x250 μm^2 and intensity I~1x10^{12} photons/s flux at the sample position. Small-angle x-ray scattering (SAXS) images were recorded by MarCCD 165 (Rayonix) detector located 2.6 m downstream of the sample. A 5 mm beam stop with a built-in pin-diode protected the detector from the direct beam intensity. Simultaneously with SAXS, wide-angle x-ray scattering (WAXS) was recorded at 288 mm distance from the sample by a custom Roper detector (Roper Scientific). The detector had an opening in the middle allowing for SAXS and direct beam to go through (92). The combined SAXS/WAXS range accessible with the setup was q ~0.005 - 1.100 $Å^{-1}$ where $q=4\pi\sin\theta/\lambda$ is the reciprocal space vector and θ is the scattering angle. A quartz capillary of 1.6 mm in diameter (Charles Supper) served as a sample holder in the beam. In order to reduce radiation damage to the samples, the solutions were cooled to 10°C and then flowed through the capillary at a rate of 4 μL/s during the exposure time. Four x-ray exposures of 10 s each were performed for empty capillary, water, buffers, and samples of three different concentrations. Collected SAXS and WAXS images were preprocessed with software written by DND-CAT staff (92). The images were normalized on transmitted intensity, radially averaged, reduced on buffer scattering, merged at ~q=0.170 $Å^{-1}$ and put onto an absolute scale relative to water scattering, which was considered as a standard (93). Resulting scattering-intensity curves I(q), later called SAXS data or curves in the

manuscript, were further processed with the ATSAS 2.5 software package developed at EMBL, Hamburg, Germany (94).

SAXS Data Processing

The GNOM program (95) of the ATSAS package that utilizes an indirect-transform approach was used to evaluate the distance distribution function [P(r)], radius of gyration (R_g) and maximal diameter (D_{max}) for the scattering particles. The program was run in User mode with default parameters for a range of q cropped to 0.01 - 0.50 $Å^{-1}$. P(r) and scattering curves [I(q)] were calculated for various D_{max} and fit to the experimental data. Excellent fits were found, indicated by giving the highest total estimates for all parameters and stable R_g solutions in a region of a ~10 Å D_{max} variation (93). GNOM also provided the forward scattering intensity as an approximation of a Guinier plot [log(I) vs. (q^2)] to determine a zero-scattering angle, which was used to calculate the molecular weight of the particles (96).

P(r) functions and regularized scattering curves resulted from GNOM runs were used for *ab initio* reconstruction of the scattering particle envelope with the GASBOR program (97). The program uses a chain-like ensemble of dummy residues for the envelope reconstruction and was run in reciprocal space version, User mode, with no predicted symmetry or shape type, and with the number of residues supplied for each sample. Ten independent runs of GASBOR simulations were performed for each sample. The output shapes were subsequently aligned, averaged and filtered using the DAMAVER program run in auto-mode (98). Normalized special discrepancies (NSD) were examined to evaluate the shapes. The resulting averaged shape for the DH/PH tandem was superimposed with existing crystal structures (2RGN or 1LB1) using the Chimera (99) and PyMol (The PyMol Molecular Graphics System, Version 1.8 Schrödinger, LLC) software packages.

The coordinates of residues 149-470 of p63RhoGEF were extracted from the available PDB file (2RGN, Chain B) and used to calculate theoretical SAXS curves with the CRYSOL program (95) for comparison with the experimental SAXS curves. PDB files were made using PyMol (The PyMol Molecular Graphics System, Version 1.8 Schrödinger, LLC) and supplied to CRYSOL, which was run with default parameters. The χ values reflect the quality of the fit between calculated and experimental curves.

NMR spectroscopy and assignment of DH/PH tandem of p63RhoGEF

The $^{13}C,^{15}N$-labeled PH domain sample was prepared in 20 mM HEPES pH 8.0, 500 mM NaCl, 2 mM DTT, 2 mM TCEP and 5% D_2O. The $^{2}H^{15}N$-labeled DH domain sample was prepared in 20 mM HEPES pH 8.0, 100 mM NaCl, 2 mM DTT, 2 mM TCEP and 5% D_2O. The $^{2}H^{13}C^{15}N$-labeled DH/PH tandem and the $^{2}H^{15}N$-labeled (Arg or Lys selectively-unlabeled) samples were prepared in 20 mM HEPES pH 8.0, 150 mM NaCl, 2 mM DTT, 2 mM TCEP and 5% D_2O. A 5 mm symmetrical and D_2O-matched sample tube from Shigemi was used for data collection. Spectra were acquired at 30˚C on a 600 MHz Bruker Avance III spectrometer equipped with a cryoprobe, running Topspin version 2.1. Processing of data was done by NMRPipe and viewed using NMRDraw (100). Backbone assignment of the DH/PH was performed using the program Sparky and a series of triple-resonance experiments including CBCACONH, HNCACB and HNCA for the PH domain, and HNCO, HNCA, HNCACB, HNCACO, HNCOCACB, HNCOCA and NOESY for the tandem.

Measurement of residual dipolar couplings

Samples for residual dipolar couplings were made using ~160 μM $^{2}H^{15}N$-labeled DH/PH in 20 mM HEPES pH 8.0, 150 mM NaCl, 2 mM DTT, 2 mM TCEP and 5% D_2O. For aligned samples, charged polyacrylamide gels were prepared as described previously (101, 102). TROSY and HSQC spectra were collected for both isotropic and anisotropic samples to measure the $^{1}J_{NH}$ and $[^{1}J_{NH}+^{1}D_{NH}]$ couplings . Residual dipolar couplings were calculated by finding the difference between these. The experimental RDC values were compared to RDC values predicted by the DC program (PALES) in NMRPipe (100), using the p63RhoGEF DH/PH tandem (residues 149-470) of PDB code 2RGN (83).

Mass Spectrometry

Mass spectrometry analysis of p63RhoGEF (residues 149-502) was performed on a sample of p63RhoGEF in 20 mM HEPES pH 8.0, 150 mM NaCl and 2 mM TCEP and that had been incubated at 30˚C for one week was used. The sample was run on an Agilent Q-TOF HPLC-MS in positive ion electrospray mode.

Molecular Dynamics

In order to understand the contribution of each domain to the dynamics of the system as a whole, nine models were created and subjected to molecular dynamics simulation (PDB:2RGN): $G\alpha_q$–p63RhoGEF–RhoA (chains DEF), $G\alpha_q$ (Y356A)–p63RhoGEF–RhoA (chains DEF), $G\alpha_q$–p63RhoGEF (chains DE), p63RhoGEF (chain E), p63RhoGEF (I205N) (chain E), DH domain of p63RhoGEF (chain E, residues 149-338), p63RhoGEF–RhoA (chains EF), DH domain of p63RhoGEF (residues 149-338) with RhoA (chains EF), and Dbs (PDB:1LB1, chain G) (83, 103). Missing loops were modeled in with the prime tool (Schrödinger) and hydrogens were added and side chain positions optimized with MolProbity (104). Input files were prepared using the tleap utility of AMBER with ff99SB (105). Due to the size of the systems, implicit solvent model II of Onufriev, Bashford, and Case was used rather than explicit solvent (106). Moreover, implicit solvent models have been shown to greatly decrease the time required for conformational sampling compared to explicit-solvent simulations (107). For each system studied, 25 simulations were performed. The systems were initially minimized for 2500 steps, followed by heating to 300 K over 40 ps with a timestep of 2 fs and restraints of 2 kcal/mol-$Å^2$ on heavy atoms. Temperature was controlled via Langevin dynamics with a collision frequency of 1 ps^{-1}. The systems were then equilibrated over 115 ps as restraints were gradually removed. Following equilibration, production runs were carried out for 10 ns using the GPU-enabled version of pmemd, yielding 250 ns of total production time per system (105, 108, 109). Histogram plots of the last 2 ns from each simulation were made using 100 bins in Igor Pro using the Box algorithm with 5 points.

Results

SAXS Experiments of the p63RhoGEF DH/PH tandem

To determine if the DH and PH domains of p63RhoGEF are in a conformation that resembles the tandem of Dbs, SAXS was used to generate scattering curves for the tandem and isolated DH and PH domains of p63RhoGEF (Fig. 3.8A). The samples showed monodispersion as evaluated by inspection of the scattering curve and Guinier plot (Fig 3.8A-B). The forward scattering intensity ($I_{(0)}$), radius of gyration (Rg) and maximum diameter (Dmax) were calculated from the scattering curves using GNOM (Table 3.2). The $I_{(0)}$ was used to calculate molecular weights for the samples, which correlated well with their expected sizes. The total estimated

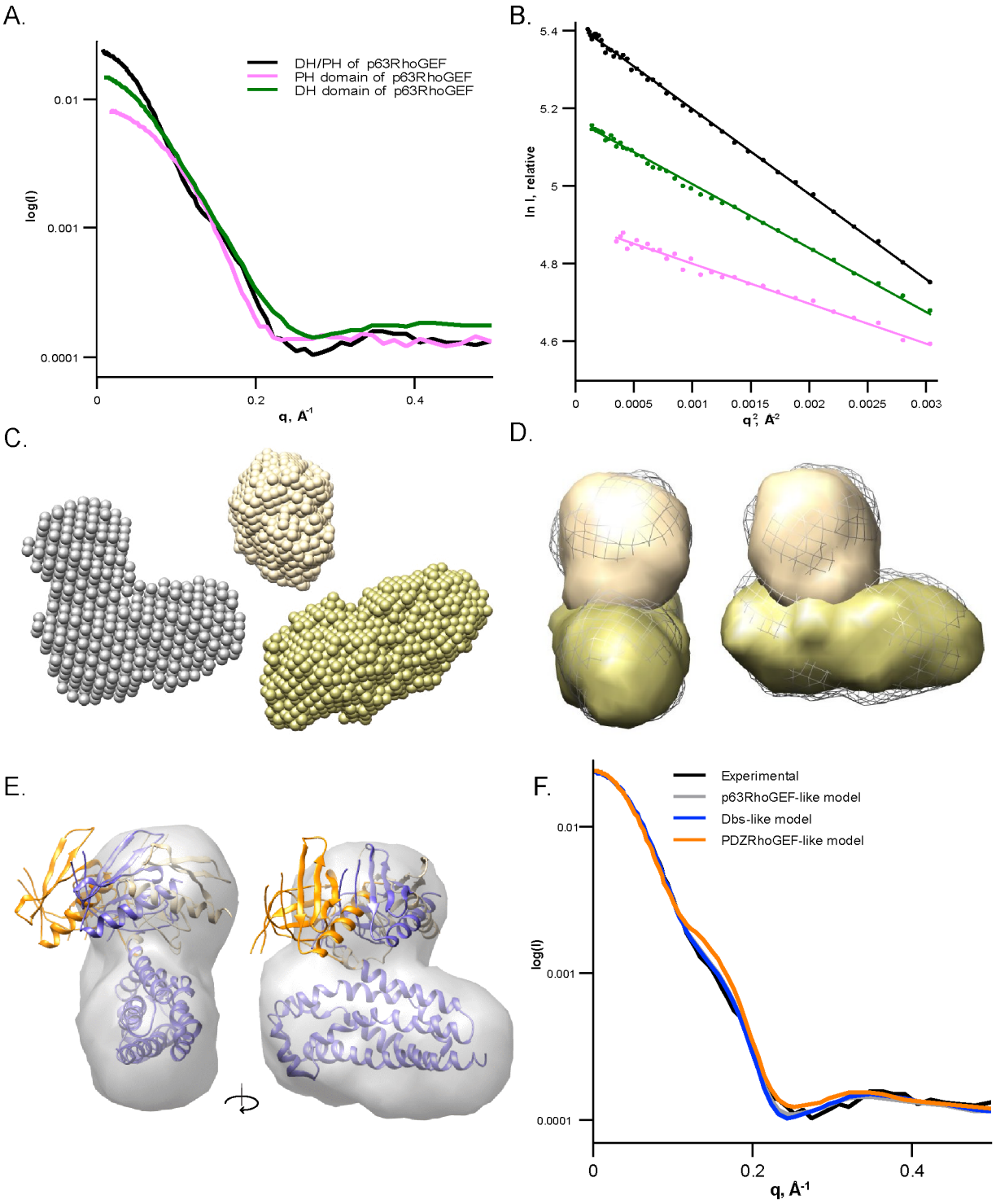
A.
DH/PH of p63RhoGEF
PH domain of p63RhoGEF
DH domain of p63RhoGEF
log(I)
0.01
0.001
0.0001
0
0.2
0.4
q, A-1
B.
ln I, relative
5.4
5.2
5
4.8
4.6
0
0.0005
0.001
0.0015
0.002
0.0025
0.003
q2, A-2
C.
D.
E.
F.
Experimental
p63RhoGEF-like model
Dbs-like model
PDZRhoGEF-like model
log(I)
0.01
0.001
0.0001
0
0.2
0.4
q, Å-1

Figure 3.8 SAXS scattering curve analysis. *A*, Scattering curves of the DH/PH tandem and individual domains were generated. Scattering of the DH/PH tandem variant (residues 149-470) was collected at 5 mg/mL, the PH domain (residues 334-470) was collected at 1 mg/mL, and the DH domain (residues 149-338) was collected at 2.5 mg/mL. *B*, Guinier plots of scattering data show linearity, indicating monodispersion. The DH/PH tandem is in black, the PH domain is in magenta, and the DH domain is in green. *C*, The shape reconstructions of the individual domains and tandem were calculated by GASBOR using dummy residues. In gray spheres is the DH/PH tandem, in light tan spheres is the PH domain, in yellow spheres is the DH domain. Each sphere represents a dummy residue. *D*, The envelopes of the individual domains were fit into the DH/PH tandem envelope. In light tan is the PH domain, in yellow is the DH domain, in gray wire is the DH/PH tandem. *E*, The DH/PH tandem of p63RhoGEF modeled in conformations resembling Dbs, PDZRhoGEF and active p63RhoGEF were fit into the experimental envelope of the p63RhoGEF tandem. In transparent gray is the DH/PH envelope, superimposed DH domains are in purple, the PH domain of the p63RhoGEF-like conformation is in light tan, the PH domain of the Dbs-like conformation is in purple and the PH domain of the PDZRhoGEF-like conformation is in orange. *F*, The scattering curves calculated by CRYSOL of the p63RhoGEF-like, Dbs-like and PDZRhoGEF-like models are compared to the experimental scattering curve for the DH/PH domain

values calculated for the tandem and both single domains are considered excellent fits. The Dmax values calculated by GNOM are also on the order for what may be predicted based on the crystal structure of the active conformation of the p63RhoGEF tandem (~74 Å for the DH domain, ~44 Å for the PH domain, ~76 Å for the tandem). These calculations therefore indicated that our experimental SAXS curves contained meaningful data.

Three-dimensional models based on the SAXS scattering curves were determined using GASBOR (Fig. 3.8C). The calculated shapes of the separate DH and PH domains corresponded well to what was found in the crystal structure of p63RhoGEF, with less than 2% of atoms lying outside their resulting envelopes. The separate domain envelopes could also be docked into the DH/PH envelope, as judged visually by the overall similarity in their shapes (Fig. 3.8D). For the DH/PH envelope, the DH/PH tandem from the p63RhoGEF crystal structure was used, as well as two alternative models. These models were made by superimposing the DH and PH domains of the p63RhoGEF crystal structure onto the corresponding domains from either the Dbs (1LB1) or PDZRhoGEF (1XCG) crystal structure to generate models of the p63RhoGEF tandem in a Dbs or PDZRhoGEF-like conformation. These three models were then docked into the DH/PH SAXS envelope, using the previously docked DH domain crystal structure in its envelope as a reference (Fig. 3.8E). The orientations of the PH domain with respect to the DH domain in the active p63RhoGEF and Dbs-like conformations appear to be equally well accommodated by this

Sample	Calculated MW (kDa)	GNOM MW (kDa)	Rg (Å)	Dmax (Å)	Total estimate
DH/PH tandem	38	40	26	80	0.902
DH domain	23	24	22	75	0.824
PH domain	16	14	16	50	0.901

Table 3.2 Analysis of SAXS scattering curves. Molecular weight (MW), Radius of gyration (Rg), maximum diameter (Dmax) and total estimate were calculated by GNOM. The total estimate is an indicator of the quality of the distribution function curve calculated by GNOM based on how well the calculated and experimental functions correlate with respect to several criteria (Svergun 1991). It is based on a scale of 0 to 1, where a value closer to 1 would describe a better quality of calculated distribution function.

model, whereas that of the PDZRhoGEF-like model does not fit well. This is judged by the obvious positioning of the PH domain in the PDZRhoGEF-like model outside of the envelope, while the other two models lie mostly inside the envelope (Fig. 3.8E).

Another analysis approach is to compare theoretical scattering curves of various conformations of the p63RhoGEF DH/PH tandem to what was found experimentally. Again, the DH and PH domains of p63RhoGEF were superimposed onto the corresponding domains from the crystal structure of either Dbs (1LB1) or PDZRhoGEF (1XCG), and theoretical scattering curves for the modeled arrangements (Dbs-like or PDZRhoGEF-like, respectively) were calculated by CRYSOL (Fig. 3.8F, Table 3.3). A scattering curve for the arrangement of the tandem found in the $G\alpha_q$-activated crystal structure was also calculated (p63RhoGEF-like). The p63RhoGEF and Dbs-like conformations had identical Rg values that were 1Å less than the experimental value, whereas that of the PDZRhoGEF-like conformation was 1Å larger than the experimental value. The Dmax values for the p63RhoGEF-like and Dbs-like models were within 1Å of the experimental value, while the PDZRhoGEF-like model yielded a value 4Å larger than the experimental value. The p63RhoGEF- and Dbs-like models show very similar χ values, differing by less than 8%. Expectedly, the PDZRhoGEF-like tandem conformation exhibits a much larger χ value, more than three times the value for either of the other models. From this analysis it is clear that the PDZRhoGEF-like tandem arrangement fits our experimental data least well, and both the Dbs-like and p63RhoGEF-like arrangements fit equally well.

Conformation	Rg, Å	Dmax, Å	χ
p63RhoGEF-like	24	80	0.371
Dbs-like	24	79	0.344
PDZRhoGEF-like	26	84	1.216

Table 3.3 Comparison of theoretical scattering curves. The DH and PH domains of p63RhoGEF were modeled into conformations resembling Dbs, PDZRhoGEF and active p63RhoGEF. Radius of gyration (Rg), maximum diameter (Dmax) and χ values for comparison with the experimental scattering curve were determined by CRYSOL. The χ value is a least squares minimization that reflects how well the calculated SAXS curves match the experimentally obtained curve, and lower values indicate a better fit between experimental and theoretical data (Svergun 1995).

Molecular Dynamics Simulations of p63RhoGEF

The dynamics of the α6-αN linker helix in p63RhoGEF were predicted using molecular dynamics simulations. Initial structures were taken from the ternary complex crystal structure (2RGN). The movements of the p63RhoGEF DH/PH tandem alone were compared to those when it was bound to either RhoA or $G\alpha_q$, or to both. The DH domain of the tandem was also simulated with and without RhoA bound. The most prominent change in these simulations was a hinging of the α6-αN helix, measured as an angle formed by alpha carbons of p63RhoGEF residues L319, P330 and M337 (L795, L806 and M813 in Dbs) (Fig. 3.9). The linker helix hinges in a direction away from the RhoA binding interface on the DH domain. An unhindered, static helix would be predicted to naturally favor an elongated conformation, having highest frequency at angles nearest 180˚. A constrained helix would have a decreased range of angles sampled, while any energetically favored angles would show an increased frequency relative to other, less favorable, angles. The DH domain of p63RhoGEF (residues 149-338), whether alone or in complex with RhoA, favored a large angle just short of 180˚. Because the PH domain is no longer attached, it was predicted that this linker helix would adopt the most elongated conformation. In simulations when the PH domain was not present, the curves show a decrease in frequency of lower angles (~120˚-150˚) compared to all other curves. The DH/PH tandem of p63RhoGEF in complex with RhoA, with or without $G\alpha_q$ bound, showed highest preference for an angle of ~150˚, but sampled angles regularly down to 130˚. This ~150˚ preference is smaller than the 164˚ hinge angle found in the crystal structure of p63RhoGEF. Interestingly, the DH/PH tandem of p63RhoGEF alone favored a wider angle of ~160˚ that is more similar to the crystal

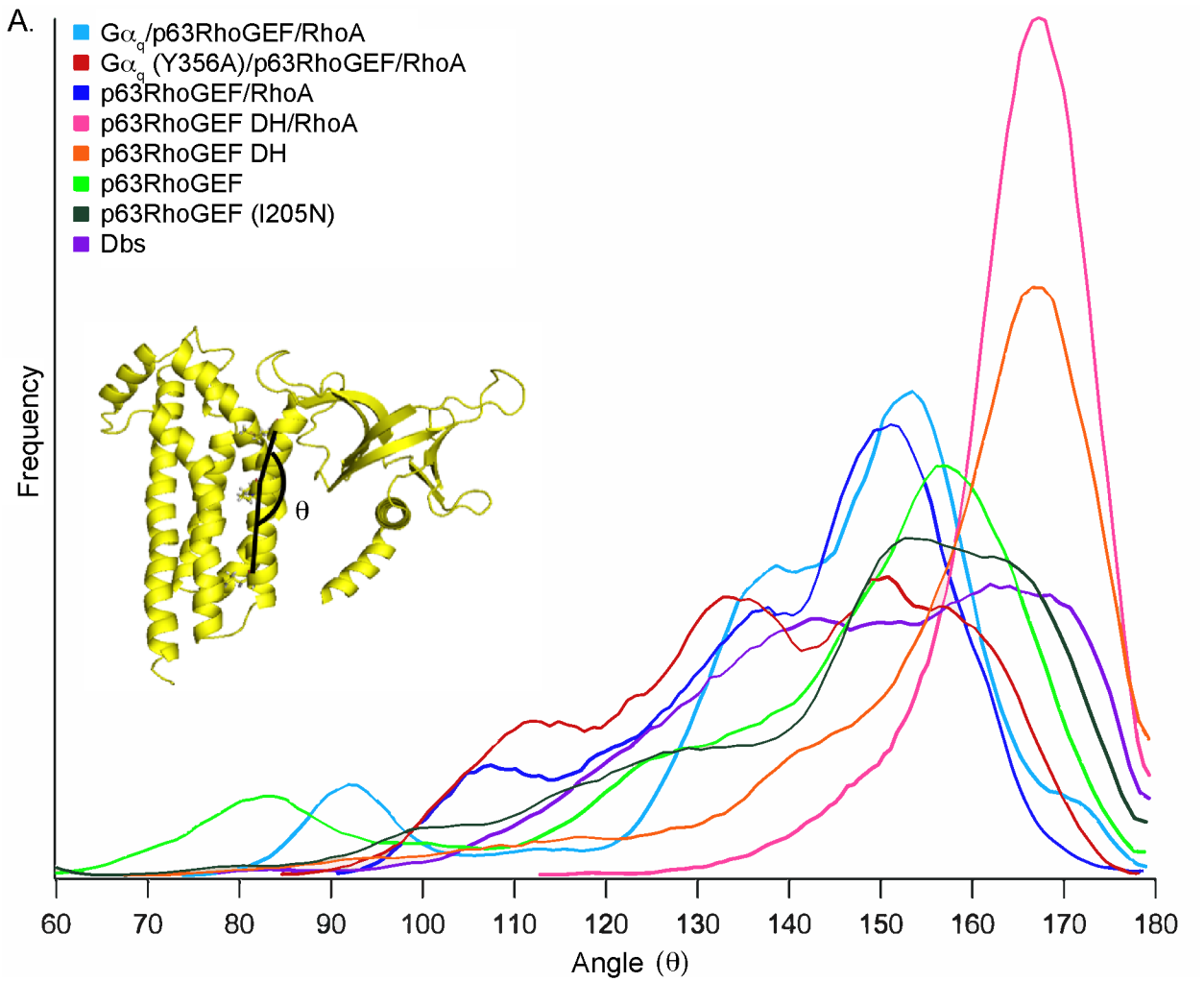

Figure 3.9 Molecular dynamics angle frequency histogram. The DH/PH domain shown in yellow indicates the location of residues L319, P330 and M337, whose alpha carbons form the measured angle.

structure angle. Simulations of Dbs revealed that it had less preference for a particular angle in comparison to p63RhoGEF. Dbs frequently sampled a similar range of angles to p63RhoGEF, with the addition of up to ~5˚ wider angles. This may be related to the fact that Dbs also adopts a larger angle in its crystal structure (173˚) in comparison to p63RhoGEF. Both Dbs and p63RhoGEF maintained their initial rotation of the PH domain around the linker helix with respect to the DH domain, contradictory to the proposed activation mechanism.

The dynamics of mutating two residues involved in contacts between the DH domain of p63RhoGEF (I205N) and the C-terminus of $G\alpha_q$ (Y356A) were also examined. The p63RhoGEF (I205N) mutant has decreased affinity for $G\alpha_q$ and decreased stimulation by $G\alpha_q$ (110). Either

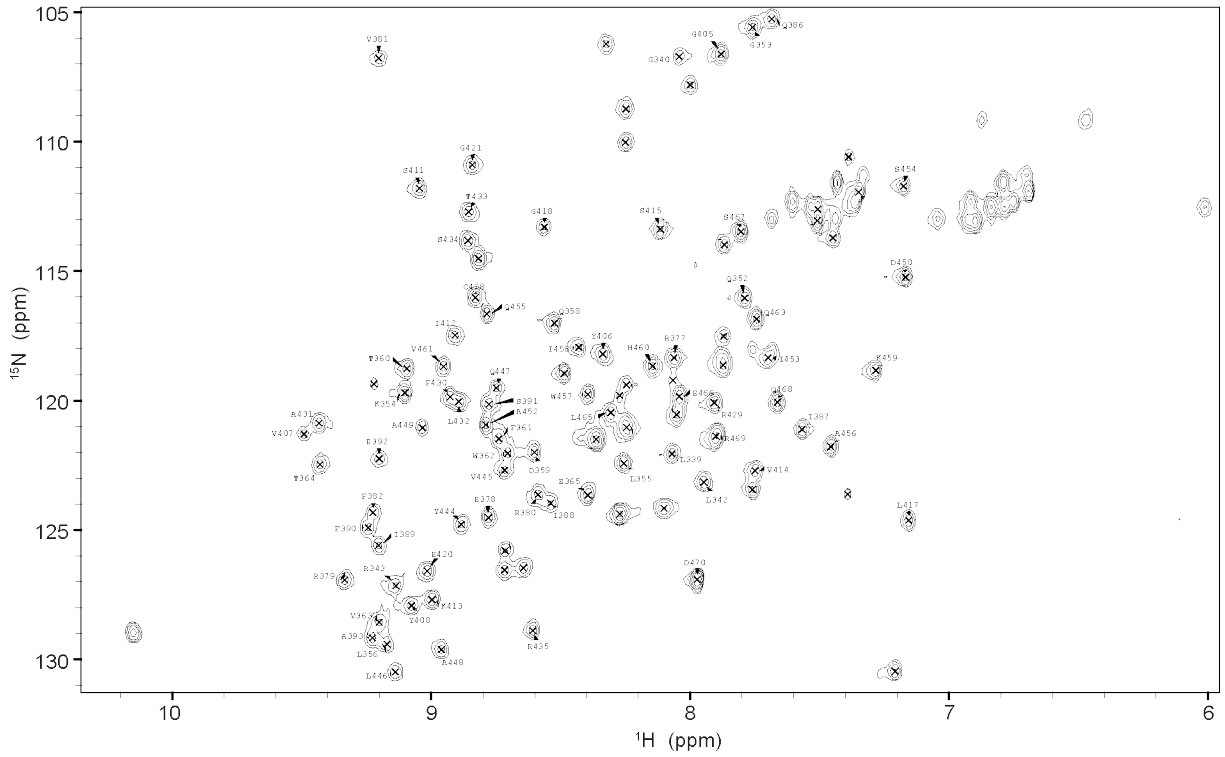

Figure 3.10 HSQC spectrum of the PH domain (residues 334-470). Assigned peaks are labeled according to residue number in full-length p63RhoGEF.

mutation results in a defect in GEF activity (88, 110). When bound to RhoA and $G\alpha_q$ (Y356A), simulations show that the most frequented angle of the p63RhoGEF linker helix is smaller than the angle when p63RhoGEF is alone. Furthermore, p63RhoGEF-RhoA-$G\alpha_q$ (Y356A) does not favor a particular angle to the extent that p63RhoGEF alone does, exhibiting almost equal preference for angles spanning ~132-156˚. The I205N mutant of p63RhoGEF differs from wild-type p63RhoGEF in that it favors the ~160˚ angle less over similar angles, resulting in a broader peak. Because the dynamics of the hinging of the linker helix when either mutation is made shift the histogram profile to show less favoring of a particular angle, their histograms become more similar to that of Dbs.

Determination of the Basal Conformation of p63RhoGEF by NMR

In an effort to determine a model of the basal, inactive conformation of p63RhoGEF, multi-dimensional NMR experiments were performed. At 40 kDa, the DH/PH tandem is a challenging target by current NMR standards, so we employed a strategy taken by others that

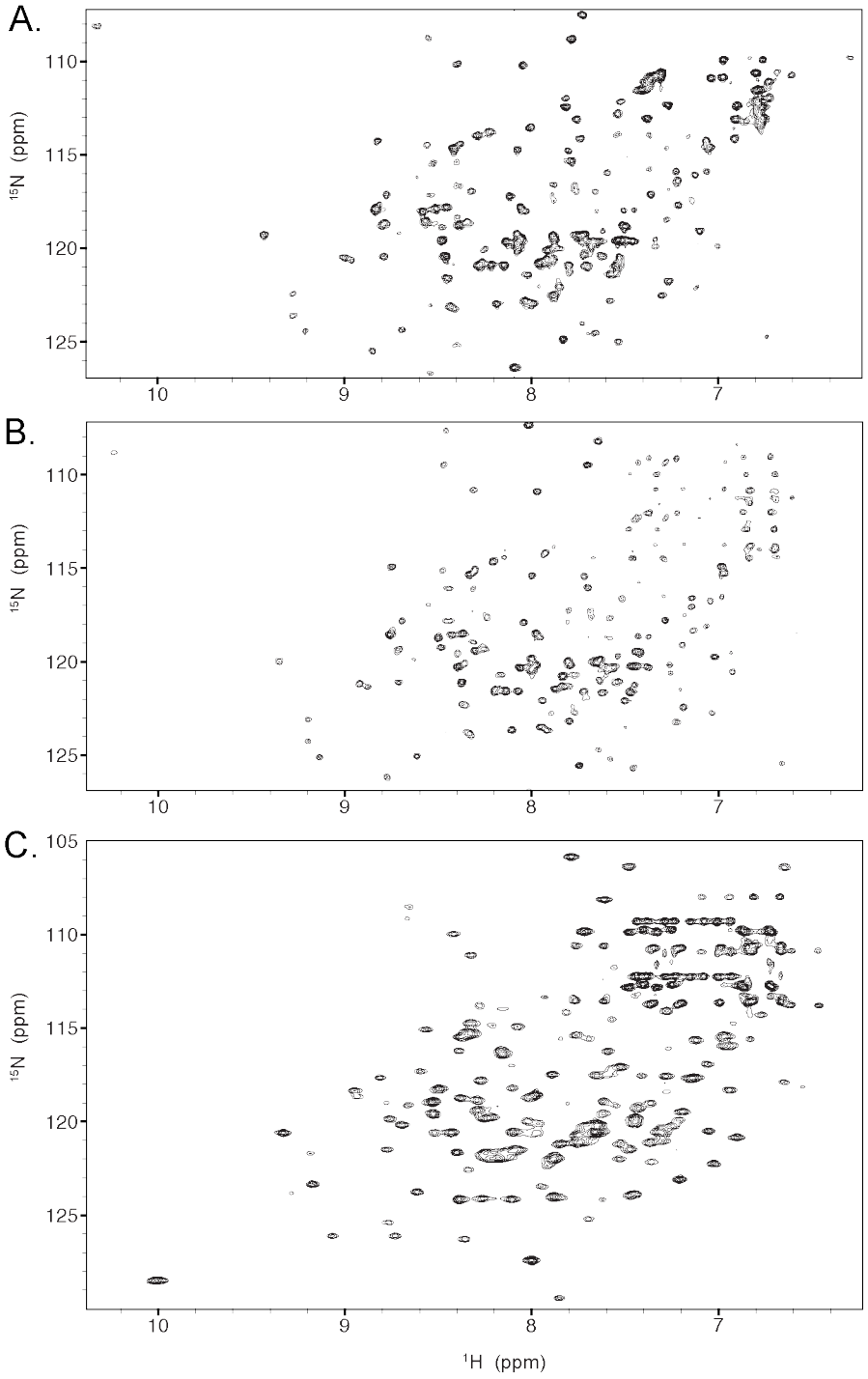

Figure 3.11 Spectra of DH domain (residues 149-338). *A*, HSQC spectrum of the DH domain alone. The DH domain is ^{15}N labeled. *B*, TROSY-HSQC of the DH domain alone. The DH domain is ^{2}H, ^{15}N labeled. *C*, TROSY-HSQC of the DH-RhoA complex where only the DH domain is labeled with ^{2}H, ^{15}N.

requires the assignment of isolated domains to aid in the assignment of the multi-domain construct (102). At 15 kDa, The PH domain (residues 334-470) was the smaller of the two domains and did not require deuteration. After ^{13}C and ^{15}N labeling, HSQC (Fig. 3.10), CBCACONH, HNCACB, HNCA and NOESY spectra were obtained. There are 141 total

residues in the PH domain variant, of which ~54% were assigned in the HSQC using the CBCACONH and HNCACB experiments.

The DH domain is slightly larger than the PH domain at 23 kDa. Although this size is still well within the limits of NMR experiments, the domain was poorly behaved in isolation. Initial experiments were similar to the PH domain, with ^{13}C and ^{15}N labeling (Fig. 3.11A). Poor spectra due to instability of the sample past two days prompted the additional use of deuteration to improve resolution and sensitivity of the experiments (Fig. 3.11B). Unfortunately, this still did not yield satisfactory spectra. A second approach was to design several C-terminally truncated mutants of the DH domain to increase sample stability. The original construct (149-338) was compared to a truncation, residues 149-335, and a truncation paired with a mutation, residues 149-337 with M336S. Comparison of 1D spectra over the course of several days indicated no improvement in stability with either truncation. The final strategy used to stabilize the DH domain was to prepare it as a complex with RhoA. Triple-labeled DH domain was bound to unlabeled, nucleotide-free RhoA and isolated by size-exclusion chromatography (Fig. 3.11C).

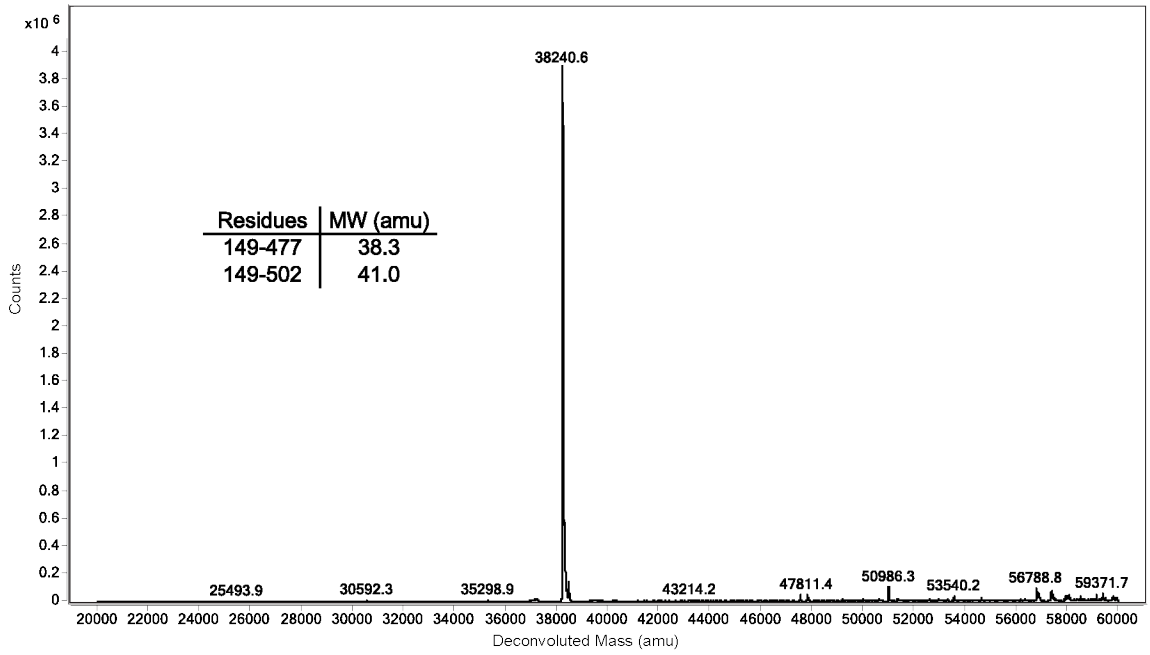

Figure 3.12 Electrospray ionization mass spectrometry deconvoluted mass. A sample of the DH/PH tandem (residues 149-502) was analyzed after a week of experiments. The expected mass for the tandem variant was ~3 kDa greater than what was observed. The observed mass corresponds to a variant spanning 149-477. Molecular weights listed include exogenous N-terminal residues.

The 2D spectra of this complexed DH domain showed some improvement over previous spectra, but it is questionable if the addition of RhoA would have any effects on the backbone conformation of the DH domain, making this approach less ideal. The DH-RhoA complex was not pursued further.

Several optimization steps were required for attaining satisfactory spectra for the DH/PH tandem. The most impactful change was C-terminal truncation of the original variant (residues 149-502). Sample stability of the 149-502 variant declined after several days and mass spectrometry showed a smaller mass than was expected (Fig. 3.12). Therefore a shorter construct was prepared, spanning residues 149-470. This construct was stable in experiments over the course of two weeks.

Expression problems involving slow growth and low ODs prompted experimentation with the expression protocol. The unlabeled M9 culture was found to be most successful at 500 mL, as 300 mL cultures often yielded long lag growth times after transfer into 500 mL of the

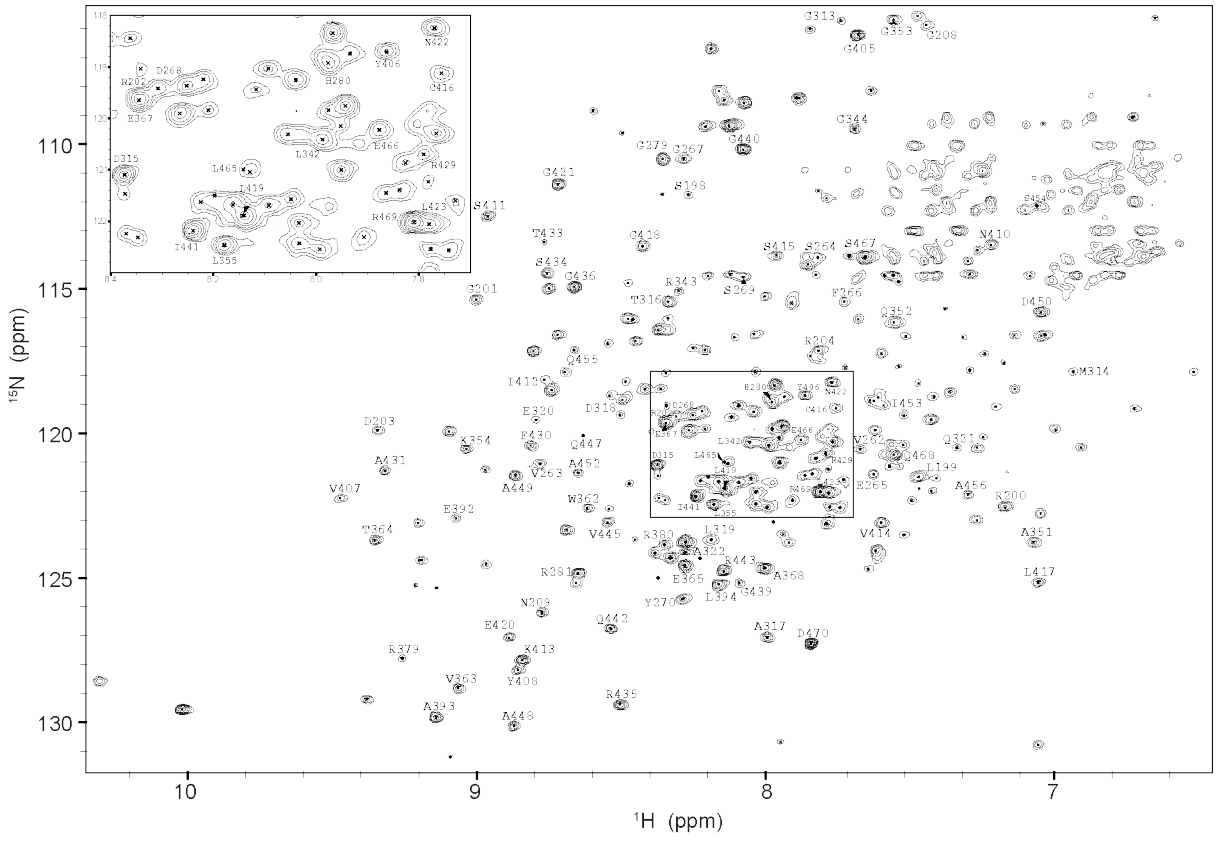

Figure 3.13 TROSY spectrum of the DH/PH tandem. Assigned peaks are labeled according to residue number in full-length p63RhoGEF. Inset is a portion of spectra enlarged for detail.

labeled M9 cultures. To maximize yields, log phase for the Rosetta DE3 cells in M9 was tested and it was found to be reasonable to induce cultures up to an OD_{600} of 1. It was also found that by doubling the buffering salts in the original M9 recipe (from 4 to 8 g/L Na_2HPO_4, and from 2 to 4 g/L KH_2PO_4), growth could be accelerated, perhaps due to increased maintenance of an optimal pH for growth. Induction times as short as 16 hours were also found to be sufficient for high yields.

Once expression was optimized, additional improvement of the purification process was also required. The salt concentration was optimal at 500 mM for the PH domain, but the DH domain and DH/PH tandem could tolerate lower concentrations (100 -150 mM). High salt concentrations result in decreased sensitivity of NMR experiments, so stability at lower salt will also allow for better spectra. Use of a cell homogenizer instead of sonication to lyse cells greatly increased protein yields. Depending on the affinity column resin brand and quality, the wash protocol needed to be adjusted. The Qiagen Ni-NTA agarose resin exhibited more nonspecific

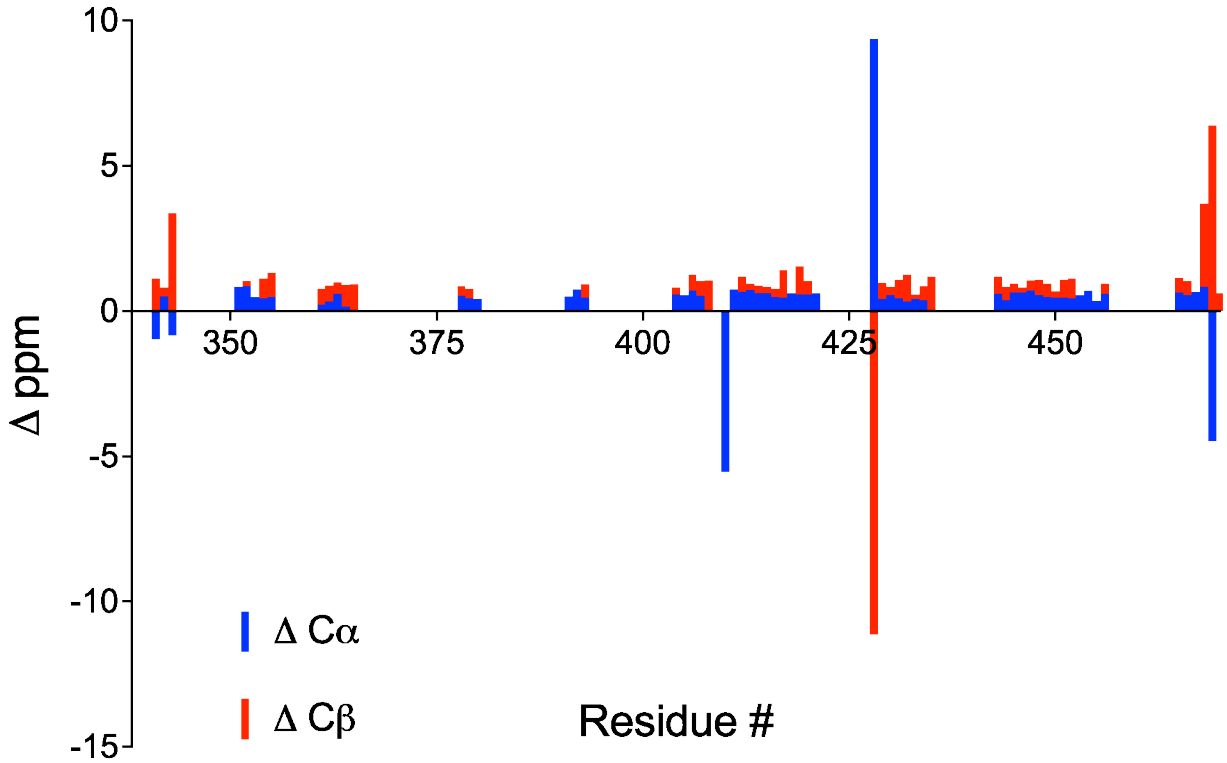

Figure 3.14 ^{13}C chemical shift variation between assigned PH and DH/PH peaks. Only Cα or Cβ peaks that were assigned in both samples are plotted. The residue number corresponds to full-length p63RhoGEF. The bars corresponding to Cys428 and Asn410 are not on either termini of the variant, but show a large difference in chemical shift.

A

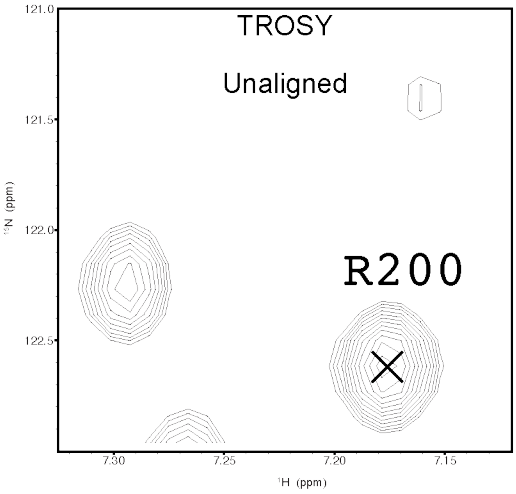
TROSY
Unaligned
R200
121.0
121.5
122.0
122.5
^{15}N (ppm)
7.30
7.25
7.20
7.15
^{1}H (ppm)

B

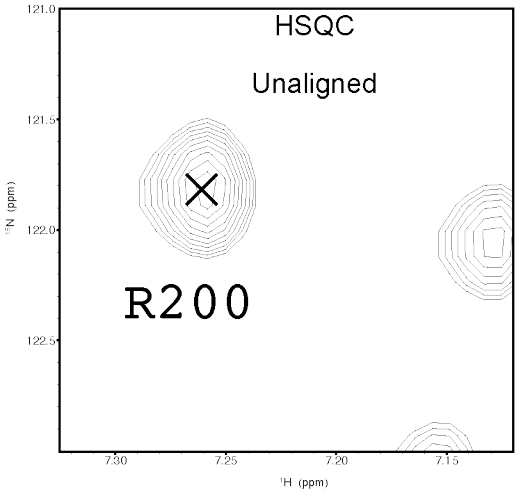
HSQC
Unaligned
R200
121.0
121.5
122.0
122.5
^{15}N (ppm)
7.30
7.25
7.20
7.15
^{1}H (ppm)

C

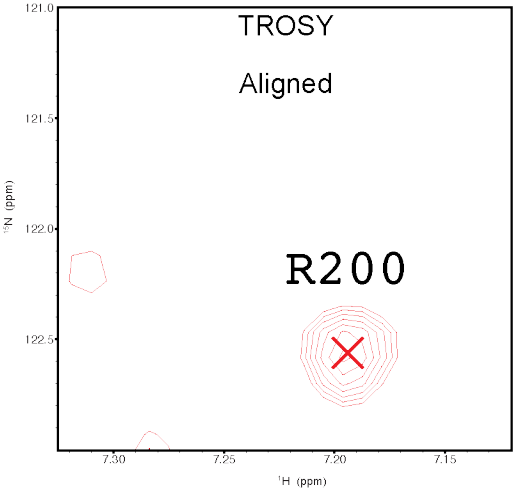
TROSY
Aligned
R200
121.0
121.5
122.0
122.5
^{15}N (ppm)
7.30
7.25
7.20
7.15
^{1}H (ppm)

D

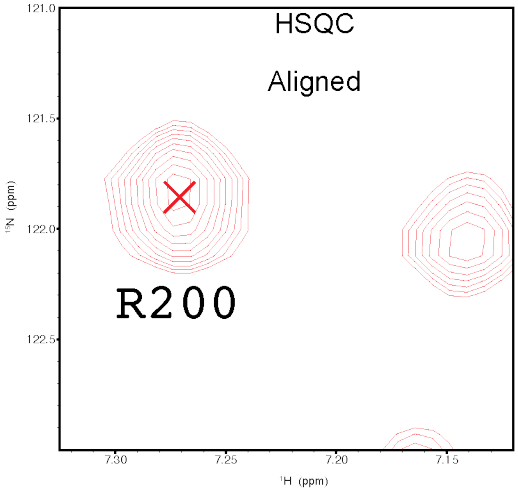
HSQC
Aligned
R200
121.0
121.5
122.0
122.5
^{15}N (ppm)
7.30
7.25
7.20
7.15
^{1}H (ppm)

E

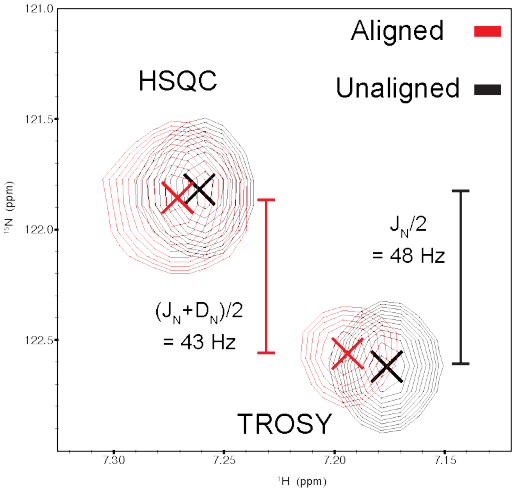
Aligned
Unaligned
HSQC
$J_N/2$
= 48 Hz
$(J_N+D_N)/2$
= 43 Hz
TROSY
121.0
121.5
122.0
122.5
^{15}N (ppm)
7.30
7.25
7.20
7.15
^{1}H (ppm)

Figure 3.15 Measurement and calculation of residual dipolar coupling values. Residue Arg200 is used as an example and its peak denoted by an X. *A*, Unaligned TROSY spectrum. *B*, Unaligned HSQC spectrum. *C*, Aligned TROSY spectrum. *D*, Aligned HSQC spectrum. *E*, Measurement scheme of RDC. Spectra from *A-D* have been superimposed. Aligned spectra are in red, unaligned spectra are in black. HSQC resides are upper left, TROSY residues are lower right. Distance measurements were taken between the HSQC and TROSY peaks for the aligned and unaligned spectra. The difference in these two distances gives D_N, the residual dipolar coupling from partial alignment. The same process can be repeated in the ^1H dimension to give D_{HN}.

protein binding than some other Ni-NTA resins, and so it required high salt and low imidazole washes before elution. Columns with less non-specific binding did not require these extra washes, as they would elute the tandem prematurely from the first affinity column. Cleavage by TEV was shown to be effective at concentrations as low as 1%, but dialyzing into a larger amount of buffer containing DTT appeared to be important for success at this step.

The resulting DH/PH tandem sample was triple-labeled (^{13}C, ^{15}N, ^2H) to obtain TROSY-HSQC, HNCA, HNCACB, HNCOCACB, HNCACO, HNCO and NOESY spectra. There are 325 residues expressed in the tandem construct (including 322 residues from the p63RhoGEF tandem), of which 29% have been currently assigned in the TROSY-HSQC (Fig. 3.13). A subset of residues assigned in the PH domain could be transferred to the DH/PH tandem. Other residues, either in the DH domain or that could not be initially recognized as from the PH domain, were also assigned. Predictably, comparison of assigned PH domain chemical shifts in the isolated PH domain and tandem show large deviations at the N terminus of the PH domain alone (Fig. 3.14). Surprisingly larger deviations were also found at the C-terminus. There are two residues, Cys428 and Asn410, which show large deviations in the middle of the PH domain as well.

Because NOESY distance constraints are limited to short distances and because limited contact between the DH and PH domains was anticipated, residual dipolar coupling (RDC) experiments were also used. In addition to long-range information on relative angles of bonds, RDC experiments can give information on the backbone dynamics of residues. HSQC and TROSY-HSQC spectra were obtained for the DH/PH tandem in solution and partially aligned in a charged gel matrix (Fig. 3.15 A-D). RDC values were calculated for both the nitrogen and hydrogen dimensions (Fig. 3.15E, Table 3.4). For most residues with calculated RDCs, large deviations from zero in the nitrogen dimension coincide with a large deviation in the hydrogen dimension and alternatively, a small deviation in the nitrogen dimension would coincide with a

small deviation in the hydrogen dimension (Table 3.4). For some residues, such as V263 or T316, this was not the case. This may be due to an inability to measure the peak location well, due to overlap of peaks or broad linewidths that make the center of the peak difficult to pinpoint.

Residue	N (Hz)	HN (Hz)
R200	11.9	-9.6
G201	-3.2	-1.2
N209	2.7	0.0
V262	10.7	-9.6
A317	1.5	0.0
L342	-2.1	-1.2
G344	4.6	-2.4
Q352	7.4	-6.0
G353	2.8	0.0
L355	0.6	0.0
V363	8.5	-8.4
N410	11.7	12.0
S415	5.5	-8.4
C416	15.2	1.2
L417	-1.3	3.6
G418	12.7	-10.8
G421	13.7	-12.0
N422	10.2	-4.8
S434	0.6	0.0
R435	-2.0	1.2
Q447	7.7	-4.8
D450	-1.9	3.6
Q455	4.6	-4.8
D470	5.6	-6.0

Table 3.4 RDC measurements for the DH/PH domain. Residues that had good agreement between values (within 3 Hz) calculated for ^{15}N and ^{1}H dimensions are reported. 1 ppm is equivalent to 600 Hz.

Conclusions

The initial goal of SAXS experiments was to obtain a low-resolution envelope of the DH/PH tandem that could be used to determine a relative rotation between the PH and DH domains. Whether the angle between the DH and PH domains changes between the basal and active states would give insight into how $G\alpha_q$ activates p63RhoGEF. Calculations by GNOM yielded expected values for each of the variants used (Table 3.2). The PH domain in both the previous crystal structure (16 kDa) and our SAXS experiment (14 kDa) is the smallest unit of the tandem, having a globular shape with an almost uniform radius. The DH domain is larger than the PH domain in both the previous crystal structure (23 kDa) and SAXS experiment (24 kDa)

and forms a more elongated shape that explains its longer Dmax (75 Å) compared to that of the PH domain (50 Å). The DH/PH tandem had a SAXS-determined molecular weight (40 kDa) that was similar to the cumulative calculated weights of the individual domains (38 kDa). The DH/PH Dmax (80 Å) is only slightly larger than that of the DH domain alone, which is reasonably the main determinant of its overall diameter. Total estimates were good for all three samples, but the DH domain unsurprisingly has a total estimate about 0.1 lower than the other variants, as it was later observed to be the least stable in NMR experiments as well.

Because the initial data processing of the SAXS curves indicated that the obtained data is of high quality, three-dimensional shape reconstructions were generated for the domains alone and in tandem (Fig. 3.8C). While this first analysis strategy yielded 3-dimensional data that appears to address our goal best, it is more difficult than the second analysis strategy to quantitatively judge our models within this analysis. The tandem envelope is formed from two lobes of equal length that intersect at ~90˚, creating a nearly symmetrical shape. The DH domain is ellipsoidal and the PH domain is a slightly elongated sphere, both consistent with the domain shapes found in the p63RhoGEF crystal structure and other previously determined DH and PH domains. The crystal structures of the Dbs and p63RhoGEF tandem both fit well inside the low-resolution shape (Fig. 3.8E). PDZRhoGEF has a three turn longer α6-αN linker helix than p63RhoGEF or Dbs, as well as a greater rotation than Dbs around the linker helix axis in comparison to p63RhoGEF. It served as a control in the calculations and, as expected, has a noticeably poorer fit within the tandem envelope.

A complementary and more quantitative comparison was performed through calculation of theoretical scattering curves from the three models of the DH/PH tandem (Table 3.3). From these curves it cannot be determined whether p63RhoGEF adopts a conformation closer to its prior crystal structure conformation (2RGN) or to that of Dbs (1LB1), but it is clear that any large rearrangement of the two domains is likely not occurring. Again, χ values indicate that the PDZRhoGEF-like model does not fit the experimental data as well as the Dbs-like and p63RhoGEF-like models. Both methods of analysis indicate that the rotation of the PH domain with respect to the DH domain in p63RhoGEF is likely somewhere in the range between the angle found in the crystal structures of p63RhoGEF and of Dbs. Unfortunately, at the resolution that SAXS experiments provide, the precise angle cannot be determined. In retrospect, the angle of the PH domain rotating around the linker helix with respect to the DH domain can be reduced

to a model of a sphere rotating around an ellipsoid and the angle at which this sphere rotates around the ellipsoid will have little effect on the overall structure of the model. Because SAXS experiments reflect the behavior of an ensemble of particles, the occurrence of multiple conformations or of a dynamic helix also cannot be dismissed. These changes would be unlikely to be on the order of a whole domain though, as the tandem envelope appears to reflect a single, defined conformation.

Molecular dynamics experiments were used to predict the dynamics of the linker helix. Interestingly, the MD experiments indicate that a consistent bending of the α6-αN helix occurs rather than a twist. Without a basal structure for p63RhoGEF, it is difficult to explain why the linker helix would display a certain range of hinge angles or why it would favor a particular angle. It is clear that addition of the PH domain has an influence on the range of angles sampled and the preferred angle of the linker helix. Therefore, the regulatory role of the PH domain in the tandem of p63RhoGEF may indeed be through alteration of its dynamics. Additional simulations investigating the linker dynamics of the isolated DH domain of Dbs could aid in examining this idea. If the linker helix dynamics are indeed related to the activation mechanism of p63RhoGEF, eliminating the PH domain of Dbs would be predicted to have a differing effect on the sampled angles, because Dbs operates through a different mechanism of activation (66). The MD simulations appear to contradict our SAXS results, as the observed hinging movement would move the PH domain in a way that would produce a new overall envelope. This may be because the DH/PH prefers a single hinge angle, as does the isolated DH domain (Fig. 3.9). SAXS molecular envelope reconstructions may show the $G\alpha_q$ (Y356A)-p63RhoGEF complex to be dynamic, as it is does not prefer a particular linker helix hinge angle and would likely be more heterogeneous in overall conformation. A scattering curve of a model of the DH/PH with a hinged helix could be calculated using CRYSOL and compared with our experimental data. The possibility of hinging could be supported if its χ value is at least as low as that of the Dbs-like model.

A higher resolution method such as NMR is therefore needed to determine the orientation of the tandem domains and examine what changes are undergone between the basal and activated forms of p63RhoGEF. The original strategy of assigning the individual domains and transferring these assignments onto the DH/PH tandem could not be carried out completely. The PH domain is stable and the resulting spectra were substantially assigned, but the low stability of the DH

domain was a major hurdle to obtaining satisfactory spectra. HSQC and TROSY-HSQC spectra for the DH domain show dispersed peaks and good signal to noise, but this signal decreases appreciably in less than a week. Because signal to noise increases with longer NMR experiments, sample stability is important for high quality NMR experiments, especially for three-dimensional experiments that must be run for several days to achieve sufficient signal. Additionally, poorly folded protein may also cause peak broadening and decreased peak dispersion. Improved stability of the DH domain was achieved by binding it to unlabeled RhoA. Again, TROSY-HSQC experiments showed dispersed peaks and good signal to noise, and this was maintained for one week. Because NMR chemical shifts for a given nuclei in a protein are affected by the electronic environment of that particular nuclei, and introducing a binding partner may affect the conformation of the DH domain, a portion of chemical shift values of the DH domain in complex may not coincide with what is found in the DH/PH tandem or free DH domain. Therefore, even though 2D spectra of the complex show improvement, we chose not to pursue additional 3D experiments unless it is determined they are required for DH/PH assignment and that sufficient overlap with DH/PH chemical shifts is also established.

Transfer of PH domain residue assignments to the DH/PH tandem was largely successful. While overlap of the 2D spectra was not always obvious, the Cα and Cβ chemical shifts were very reliable for matching between the samples. At the N-terminus of the isolated PH domain, larger chemical shift deviations relative to the tandem are seen. This is understandable, as whether this helix is attached or unattached to the DH domain could cause changes in its conformation. It is more surprising that the C-terminus also has larger deviations in chemical shifts, as this area would be predicted to be similar in either sample. This may be suggestive of long-range interactions between the DH and PH domains, but might also be caused by differences in sample conditions, such as the increased concentration of salt in the PH domain sample. The two residues showing larger deviations in the middle of the PH domain (Cys428 and Asn410) both have residues assigned immediately following them that do not have larger deviations. This may indicate that these residues have been misassigned or that there are backbone conformational changes occurring at these positions. Unfortunately, neither of these residues has an assigned residue immediately preceding it and so it is hard to say which of these two cases is true.

Successful completion of the NMR experiments will yield structural and dynamical data of the basal conformation of p63RhoGEF, and will resolve how $G\alpha_q$ activation occurs. The SAXS experiments suggest that a single conformation exists in the basal state, which supports the hypothesis that $G\alpha_q$ forms interactions with both the DH and PH domains to bridge the tandem and rotate the domains from a single basal conformation to another single conformation capable of RhoA activation. The MD simulations suggest the linker is dynamic and exists in several conformations, supporting an alternative hypothesis that the linker helix dynamics are reduced when $G\alpha_q$ binds to the tandem. The actual mechanism may be either of these scenarios or a combination. Completion of these NMR experiments will help explain how this significant step in $G\alpha_q$ effector signaling occurs.

Chapter 4

Conclusion

Described in this thesis are two studies concerning the function of the G protein $G\alpha_q$. Chapter 2 describes a story of $G\alpha_q$ regulation by RGS proteins. X-ray crystallography structures of RGS8 in complex with $G\alpha_q$ or $G\alpha_i$ were compared to investigate how selectivity between RGS proteins and Gα subunits is achieved. Residues in the α-helical domain of the Gα subunit were tested as determinants of selectivity and were not found to modulate the selectivity of RGS8 or RGS10 as predicted. Interactions between the α6 helix of the RGS and the SwIII region of Gα as determinants of selectivity were posed as an alternative hypothesis. Because α6 includes a single residue deletion in the R12 family members that makes sequence alignment difficult with the R4 family, mutations that could be made to alter selectivity from that like one family to the other are not straightforward. Alternatively, it may be possible to simply ablate the ability of an R4 family member to interact with $G\alpha_q$. In future studies, R128A and F125A mutants of RGS8 should eliminate key interactions between α6 of the RGS and SwIII of Gα.

Within the context of selectivity, one could choose to delve deeper into this mechanism and determine how some RGS proteins show selectivity for individual members of a Gα subfamily. For example, the RZ family of RGS proteins show selectivity for $G\alpha_z$, a member of the G_i family (39). Investigating RGS selectivity for Gα subunits within a given Gα subfamily may also explain the apparent redundancy of RGS proteins. Fine-tuned and unique preferences of RGS proteins may be important to ensure processes are regulated correctly. Interestingly, many RGS proteins show a smaller range of selectivity *in vitro* than *in vivo*. In surface plasmon resonance studies of purified protein, RGS2 shows robust activity on $G\alpha_q$ and essentially no activity on $G\alpha_{i1}$ (37). However, in cellular and lipid-based assays, RGS2 does show activity on $G\alpha_i$ (111, 112). Why this difference in activity occurs is likely stemming from additional interactions provided by the RGS protein outside of its RGS domain, and so further study of

RGS protein function should not limit itself to isolated RGS domains. Most members of the R4 subfamily have no known domain homology outside of their RGS domain, and therefore it is not always obvious what other elements may be affecting protein function. It does seem clear that RGS proteins are not redundant. While cell-specific expression may explain some overlap in functional abilities, it has been shown in the cardiovascular system that several RGS proteins are expressed together in a single cell type (113). This indicates that having only one RGS does not suffice.

Chapter 3 of this thesis describes an ongoing story of how $G\alpha_q$ signals through an effector. While it is well established that $G\alpha_q$ signals through p63RhoGEF to activate RhoA, it is not known how exactly $G\alpha_q$ is able to relieve the autoinhibition of p63RhoGEF to do this. We proposed two possible mechanisms, the first being rotation of the PH domain around the linker helix and the second being stabilization of an otherwise dynamic linker helix. To distinguish between these two hypotheses, a basal structure of p63RhoGEF must be determined for comparison with the previously determined structure of active p63RhoGEF in complex with $G\alpha_q$ and RhoA. Our continuing NMR studies hope to achieve this goal. In addition, SAXS and MD simulations were used to investigate the rotation of the PH domain and the dynamics of the linker helix in an effort to provide support for one of the proposed mechanisms. These experiments, however, show support for both proposed mechanisms. Furthermore, the MD simulations contradict rotation of the PH domain, again underscoring the need for a basal structure of p63RhoGEF. If the basal structure shows that the orientation of the PH domain with respect to the DH domain is similar to that of Dbs, then activation of p63RhoGEF is likely through $G\alpha_q$ bridging the two domains of the tandem to pull them into the correct position for RhoA binding. If the basal conformation of p63RhoGEF is similar to its active conformation, then reduction of dynamics in the linker helix likely plays a key role in the activation mechanism. The chemical shifts and RDCs gathered in our NMR experiments can be used to further investigate dynamics. The Random Coil Index (RCI) method can be used to evaluate protein dynamics on the picosecond to nanosecond timescale using the experimental chemical shifts and protein sequence (114). This technique is particularly useful for larger proteins, where traditional relaxation rate measurements can be difficult to calculate due to increased peak overlap and low signal-to-noise. Estimates of order parameters can easily be calculated from the assigned chemical shifts through the RCI server online and these RCI values have been shown to

agree well with model-free order parameters (114, 115). RDC measurements can also yield information on dynamics via calculation of similar types of order parameters, but these measurements can describe dynamics up to a ms timescale. It should be noted that calculation of order parameters from RDCs may be more difficult than those from the RCI method.

Once the mechanism of p63RhoGEF has been established, it would be wise to establish that the same mechanism is occurring in the other related $G\alpha_q$-regulated Dbl RhoGEFs, kalirin and Trio. Like p63RhoGEF, kalirin and Trio have both been shown to be activated by $G\alpha_q$, but their individual activation mechanisms have not been examined (83, 110). Additionally, determining the mechanism of $G\alpha_q$ activation will hopefully shed light on the interaction between $G\alpha_{16}$ and p63RhoGEF. $G\alpha_{16}$ is a member of the $G\alpha_{q/11}$ family, and p63RhoGEF has been shown to compete with other effectors for $G\alpha_{16}$ (116). Suprisingly, $G\alpha_{16}$ does not promote RhoA activation with p63RhoGEF. Sequence analysis of $G\alpha_{16}$ shows it has an isoleucine instead of the tyrosine (Y356 in $G\alpha_q$) at its C-terminus that interacts with the DH domain of p63RhoGEF. However, this tyrosine does not fully account for the inability of $G\alpha_{16}$ to activate p63RhoGEF, as mutating Y356 in $G\alpha_q$ still leaves ~50% of the maximal RhoA activation intact (88). Knowing the mechanism by which $G\alpha_q$ activates p63RhoGEF could help explain why $G\alpha_{16}$ is deficient in this ability.

Future experiments could make use of the assigned NMR spectrum for drug design. Relatively simple HSQC experiments can be used to show small-molecule binding through peak shifts, and our assignments can be used to find the small-molecule binding site. Although protein-protein interactions are a notoriously difficult drug-target, some successes has been reported, particularly using NMR-based approaches (117, 118). Recently, it was found that a group of hypertensive patients showed increased mRNA and protein expression levels of p63RhoGEF, whereas a group of hypotensive individuals showed decreased levels (119). Furthermore, an antihypertensive drug that blocks the angiotensin type 1 receptor (AT1R), olmesartan, was found to significantly decrease p63RhoGEF protein levels in hypertensive patients and this also correlated with a normalization in blood pressure (120). By targeting drugs for hypertension to the AT1R or $G\alpha_q$, unintended effects on other important downstream signaling effectors, such as PLC-β, could cause unwanted side effects. Developing a drug that

instead targets p63RhoGEF could therefore reduce unintended effects that may cause side effects in patients.

Recent work has identified three cysteine residues on the N-terminus of p63RhoGEF that are important for palmitoylation and membrane localization (84). Mutation of these three cysteines to serine yields a mutant that is deficient in palmitoylation, thereby allowing for expression of soluble, full-length p63RhoGEF. Some preliminary work has made use of this p63RhoGEF variant to show involvement of the N-terminus of p63RhoGEF in $G\alpha_q$ binding. While greater competition with GRK2 binding is seen when the p63RhoGEF variant includes its N-terminal region, it is unclear why. Furthermore, another group has reported that the C-terminus of p63RhoGEF contains a putative PDZ domain, a domain type known for facilitating protein-protein interactions (121). Therefore, future studies of p63RhoGEF should also focus on elements outside the DH/PH tandem. While secondary structure prediction programs and conserved domain databases return no results for residue sequences outside the p63RhoGEF DH/PH tandem, unrecognized features may still exist. N-terminal residues important for increased competition with GRK2 should be located and the nature of the interaction should be determined. Structural studies such as circular dichroism could also easily indicate if persistent secondary structure exists in either the N- or C-terminal regions.

Structural characterization of $G\alpha_q$-effector and $G\alpha_q$-regulator interactions has yielded many structures of complexes as well as single proteins. With the completion of the work described in this dissertation, the activation mechanisms of the two main effectors of $G\alpha_q$ (PLCβ and p63RhoGEF) will have been described through structures of each effector alone and in complex with $G\alpha_q$. In addition, both a canonical and a noncanonical RGS complex with $G\alpha_q$ have now been shown, to complement other previously determined structures like GRK2-$G\alpha_q$ and $G\alpha_q$-Gβγ. Some structural gaps do still exist, such as a $G\alpha_q$ heterotrimer in complex with a GPCR. These types of structures are large and involve membrane proteins, and so are much more difficult targets than Gα-effector complexes. For the most part, the various stages of $G\alpha_q$ signaling have been deconstructed into well-characterized, but isolated, parts. Cryo-electron microscopy has taken great strides in recent years, and can now deliver atomic resolution that rivals crystallography. While crystallography has been very good at characterizing the "parts" of signaling processes, it now may finally be time to start assembling these parts into the networks that they truly are. A lofty goal of cell signaling research would be to take any input signal and

be able to completely describe the resulting cascade. The structural biologist's part in this is to create the movie for the narrative.

Appendix A
Assignments of the PH domain of p63RhoGEF (residues 338-470)

	CA (ppm)	CB (ppm)	HN (ppm)	N (ppm)
T338	64.09	69.30	-	-
L339	56.48	41.77	8.072	122.0
G340	45.94	-	8.043	106.7
R341	56.19	31.13	7.868	118.5
L342	54.42	42.64	7.944	123.2
R343	55.68	32.29	9.134	127.1
A351	52.19	19.01	-	-
Q352	53.96	27.21	7.789	116.0
G353	44.05	-	7.756	105.5
K354	57.14	33.70	9.102	119.7
L355	54.91	40.98	8.260	122.3
L356	52.21	42.28	9.176	129.4
G357	45.24	-	-	-
Q358	54.35	30.95	8.524	116.9
D359	54.25	47.11	8.599	122.0
T360	61.85	70.03	9.095	118.8
F361	56.37	44.53	8.740	121.5
W362	58.24	29.45	8.706	122.0
V363	61.58	34.38	9.198	128.5
T364	60.69	71.05	9.435	122.5
E365	53.56	30.61	8.395	123.6
G376	45.09	-	-	-
R377	54.24	32.86	8.064	118.4
E378	57.37	30.33	8.780	124.5
R379	53.60	34.29	9.333	127.0
R380	54.53	29.84	8.584	123.5
V381	60.77	32.26	9.201	106.7
F382	56.78	42.26	9.228	124.4
E385	60.37	31.93	-	-
Q386	55.27	30.23	7.689	105.1
I387	61.22	42.27	7.572	121.1
I388	59.93	39.93	8.537	123.9

	CA (ppm)	CB (ppm)	HN (ppm)	N (ppm)
I389	60.78	42.19	9.200	125.6
F390	57.11	40.77	9.241	124.9
S391	57.73	69.17	8.778	120.1
E392	54.64	34.31	9.196	122.2
A393	52.70	19.00	9.227	129.2
P404	63.45	32.21	-	-
G405	44.75	-	7.880	106.5
Y406	56.81	42.59	8.340	118.1
V407	60.47	34.40	9.488	121.3
Y408	61.04	39.73	9.076	127.9
N410	47.37	-	-	-
S411	57.67	66.78	9.048	111.7
I412	61.25	42.85	8.914	117.4
K413	57.55	32.92	8.997	127.7
V414	66.06	31.68	7.749	122.7
S415	60.17	62.90	8.119	113.3
C416	58.21	29.49	7.867	118.6
L417	55.23	45.38	7.153	124.7
G418	44.48	-	8.559	113.2
L419	54.10	47.08	8.246	121.1
E420	55.45	31.98	9.014	126.6
G421	44.52	-	8.845	110.9
P427	63.57	32.89	-	-
C428	61.35	28.49	8.833	115.9
R429	55.08	35.40	7.905	120.0
F430	56.06	41.08	8.931	119.9
A431	49.64	22.16	9.433	120.8
L432	52.52	44.41	8.897	119.9
T433	59.06	70.97	8.861	112.8
S434	55.43	65.60	8.862	113.8
R435	-	31.27	8.605	128.9
R443	55.61	33.14	-	-
Y444	56.45	40.55	8.887	124.8
V445	62.65	31.95	8.715	122.7
L446	56.31	42.19	9.135	130.4
Q447	54.21	31.66	8.749	119.4
A448	50.37	22.55	8.963	129.6
A449	53.32	19.11	9.035	121.0
D450	50.57	44.31	7.167	115.2
P451	64.36	31.79	-	-

	CA (ppm)	CB (ppm)	HN (ppm)	N (ppm)
A452	55.08	18.29	8.792	115.5
I453	64.17	38.64	7.701	118.3
S454	61.90	-	7.174	111.7
Q455	58.78	28.12	8.786	116.6
A456	55.14	18.05	7.457	121.7
W457	63.59	28.02	8.394	119.7
I458	65.91	38.09	8.430	117.9
K459	59.65	31.99	7.281	118.9
H460	58.82	31.55	8.148	118.6
V461	67.10	30.65	8.954	118.6
A462	55.88	17.77	8.368	121.4
Q463	59.26	28.31	7.742	116.8
I464	65.13	37.98	8.053	120.4
L465	57.64	41.55	8.310	120.4
E466	58.56	29.61	8.041	119.7
S467	59.87	63.86	7.803	113.4
Q468	56.20	31.75	7.668	120.0
R469	51.14	36.57	7.896	121.3
D470	-	42.28	7.971	126.9

Table A.1 Chemical shifts of assigned residues for the HSQC experiment of the PH domain of p63RhoGEF (residues 338-470). Shifts are reported in ppm, dashed lines indicate no resonance assigned.

Appendix B
Assignments of the DH/PH tandem of p63RhoGEF (residues 149-470)

	CA (ppm)	CB (ppm)	CO (ppm)	HN (ppm)	N (ppm)
E197	-	-	175.9	-	-
S198	59.91	62.32	172.0	8.271	111.7
L199	53.18	42.45	173.2	7.477	121.5
R200	58.17	28.51	175.3	7.179	122.6
G201	45.37	-	175.0	9.005	115.4
R202	56.60	30.24	174.1	8.312	119.4
D203	57.25	38.66	174.8	9.346	119.9
R204	58.06	-	177.1	7.820	117.1
F207	59.57	39.69	172.6	-	-
G208	47.29	-	172.0	7.450	105.9
N209	52.64	35.40	174.2	8.777	126.2
H261	59.50	-	175.1	-	-
V262	66.23	30.47	176.3	7.670	120.6
V263	67.43	30.38	175.9	8.785	121.1
S264	61.24	62.59	173.7	7.822	113.9
E265	58.32	29.13	175.3	7.636	121.4
F266	58.63	40.81	174.7	7.728	115.4
G267	46.86	-	171.4	8.292	110.5
D268	55.87	40.56	174.6	8.258	119.4
S269	58.42	62.60	173.1	8.082	114.6
Y270	61.17	38.57	174.5	8.293	125.8
L278	54.34	-	174.8	-	-
G279	44.57	-	177.0	8.361	110.5
H280	53.89	31.84	172.6	7.976	118.9
R281	56.96	29.26	175.5	8.656	124.9
A312	51.83	-	173.7	-	-
G313	44.83	-	172.2	7.744	105.7
M314	52.82	31.88	173.2	6.935	117.9
D315	54.47	40.53	175.6	8.379	121.1
T316	61.04	68.14	172.2	8.341	115.4
A317	56.34	17.54	166.3	7.996	127.1
D318	56.82	38.83	176.1	8.497	118.8

	CA (ppm)	CB (ppm)	CO (ppm)	HN (ppm)	N (ppm)
L319	57.35	-	175.8	8.193	123.7
E320	59.75	28.05	177.2	8.799	119.5
Q321	58.42	-	175.6	7.342	120.5
A322	54.97	-	176.4	8.284	124.1
R341	57.15	30.02	174.7	-	-
L342	53.93	41.84	177.0	7.994	120.4
R343	56.51	28.92	175.2	8.308	115.1
G344	43.78	-	170.2	7.696	109.5
T350	-	-	172.5	-	-
A351	51.37	18.36	174.5	7.075	123.8
Q352	53.11	26.19	172.4	7.558	116.2
G353	43.57	-	170.8	7.558	105.7
K354	56.72	32.58	174.0	9.040	120.5
L355	54.43	39.66	-	8.182	122.5
F361	56.16	43.77	171.7	-	-
W362	57.92	28.59	174.0	8.621	122.6
V363	60.99	33.40	173.3	9.071	128.8
T364	60.54	70.17	170.9	9.356	123.7
E365	-	29.70	-	8.286	124.4
P366	63.53	30.89	174.6	-	-
E367	55.88	29.02	173.9	8.348	119.6
A368	52.73	18.30	175.9	8.007	124.7
E378	56.86	29.48	175.4	-	-
R379	53.18	33.53	171.2	9.264	127.8
R380	54.13	-	172.6	8.352	123.9
S391	57.24	68.90	168.7	-	-
E392	53.91	33.61	172.4	9.075	122.9
A393	52.25	18.09	174.7	9.145	129.8
L394	54.43	42.48	176.0	8.167	125.2
P404	62.89	31.42	173.9	-	-
G405	44.22	-	168.7	7.687	106.2
Y406	56.12	41.35	172.0	7.869	118.7
V407	59.96	33.37	173.0	9.443	122.3
Y408	-	38.68	-	8.863	128.2
K409	54.65	-	172.2	-	-
N410	52.90	40.25	170.2	7.228	113.5
S411	56.93	66.27	170.6	8.970	112.5
I412	60.60	41.66	173.2	8.770	118.1
K413	56.83	31.99	176.0	8.847	127.8
V414	65.45	30.82	174.0	7.609	123.1

	CA (ppm)	CB (ppm)	CO (ppm)	HN (ppm)	N (ppm)
S415	59.57	62.07	172.7	7.966	113.9
C416	57.74	28.74	170.9	7.761	119.1
L417	54.77	43.98	172.8	7.059	125.2
G418	43.88	-	168.5	8.424	113.5
L419	53.53	45.55	173.1	10.210	121.9
E420	54.88	30.96	172.9	8.887	127.1
G421	43.92	-	169.6	8.722	111.4
N422	53.20	36.70	173.6	7.778	118.2
L423	55.81	40.55	-	7.782	122.1
C428	51.99	39.61	171.3	-	-
R429	54.67	34.45	172.6	7.794	120.7
F430	55.53	40.26	168.5	8.818	120.4
A431	49.22	21.10	173.9	9.290	121.9
L432	52.20	43.17	173.3	-	-
T433	58.66	70.41	171.0	8.770	113.4
S434	55.06	64.76	171.8	8.761	114.5
R435	54.91	30.09	174.0	8.508	129.4
G436	44.22	-	171.0	8.663	114.9
E438	60.37	-	170.9	-	-
G439	44.69	-	172.1	8.094	125.2
G440	44.55	-	170.5	8.078	110.2
I441	59.50	39.29	173.6	8.241	122.2
Q442	54.19	30.37	171.3	8.541	126.8
R443	55.02	31.96	170.4	8.151	124.8
Y444	56.09	39.72	172.0	-	-
V445	62.03	31.02	-	8.555	123.1
L446	55.69	41.39	171.2	-	-
Q447	53.53	30.62	173.0	8.633	120.1
A448	49.83	21.49	174.1	8.875	130.1
A449	52.84	18.17	174.1	8.873	121.5
D450	50.13	43.64	172.3	7.050	115.8
P451	63.91	30.71	174.4	-	-
A452	54.65	17.17	167.5	8.653	121.4
I453	63.63	-	175.6	7.589	119.0
S454	61.21	-	174.2	7.058	112.1
Q455	58.44	-	175.9	8.664	117.1
A456	54.55	17.11	177.3	7.300	122.1
L465	57.02	40.42	177.2	8.139	121.0
E466	58.02	28.59	175.4	7.881	120.2
S467	59.22	63.28	172.0	7.663	113.9

	CA (ppm)	CB (ppm)	CO (ppm)	HN (ppm)	N (ppm)
Q468	55.38	28.07	173.1	7.562	120.7
R469	55.60	30.18	172.5	7.814	122.0
D470	-	41.68	166.5	7.846	127.3

Table B.1 Chemical shifts of assigned residues for the HSQC-TROSY experiment of p63RhoGEF (residues 149-470). Shifts are reported in ppm, dashed lines indicate no resonance assigned.

Appendix C

The N-terminus of p63RhoGEF in $G\alpha_q$ Binding

Previous work with p63RhoGEF has shown that full-length, wild-type variants (residues 1-580) are difficult to purify because this variant exists mainly in the membrane fraction of lysed cells. Aittaleb *et al.* showed that p63RhoGEF is constitutively localized to membranes through palmitoylation of three cysteine residues at its N-terminus (residues 23, 25 and 26) (84). Because of this discovery, it was surmised that full-length p63RhoGEF could be purified through elimination of these palmitoyl groups. The three cysteine palmitoylation sites were mutated to serines, thereby inhibiting palmitoylation (palm$^-$). Expression of full-length, palm$^-$ p63RhoGEF in both High Five and BL21 (DE3) cells yielded protein mainly in soluble fractions that could be easily purified. Variants of palm$^-$ p63RhoGEF were then tested in a flow cytometry protein interaction assay (FCPIA) to assess their competitive binding with GRK2 on $G\alpha_q$ (Fig. C.1A) (122). $G\alpha_q$ variants were biotinylated and immobilized on beads. Fluorescently labeled GRK2 was pre-bound to $G\alpha_q$. GRK2 was then competed off of $G\alpha_q$ using either unlabeled GRK2 or variants of p63RhoGEF. While the DH/PH tandem (residues 149-502) of p63RhoGEF competes with GRK2 less than GRK2 itself, both variants of p63RhoGEF that include its N-terminus (residues 1-502 palm$^-$ and residues 1-580 palm$^-$) appeared to compete off GRK2 with higher potency than the DH/PH. The difference in EC_{50} values between either palm$^-$ variant and DH/PH was significant (Fig. C.1B).

Structure prediction programs did not indicate any obvious structural elements in the N-terminus that may account for this increased affinity with $G\alpha_q$. A small, conserved region of sequence in the N-terminus of p63RhoGEF (residues 121-128, "LTLLTTLL") had been previously noted to resemble the sequence of an amphipathic helix (84). This sequence was deleted from the palm$^-$ variants to test if the increase in binding was subsequently lost. Preliminary FCPIA assays suggest that the increased binding is unaffected by deletion of this sequence. The palm$^-$, ΔLTLLTTLL variant spanning residues 1-502 was tested in direct binding (N=2) and competitive binding (N=2) FCPIA assays. The ΔLTLLTTLL palm$^-$ variant does not

appear to bind $G\alpha_q$ less than the previously tested palm$^-$ variants.

Direct binding to full-length (7-359) and ΔN (35-359) $G\alpha_q$ was also performed with palm$^-$ p63RhoGEF (1-502) to test whether the N-terminus of $G\alpha_q$ was involved in this additional interaction. Preliminary direct binding FCPIA assays (N=3) indicate that the N-terminus of $G\alpha_q$ is not necessary for the increased binding between p63RhoGEF and $G\alpha_q$. Dissociation constants of palm$^-$ p63RhoGEF with ΔN or full-length $G\alpha_q$ were not significantly different.

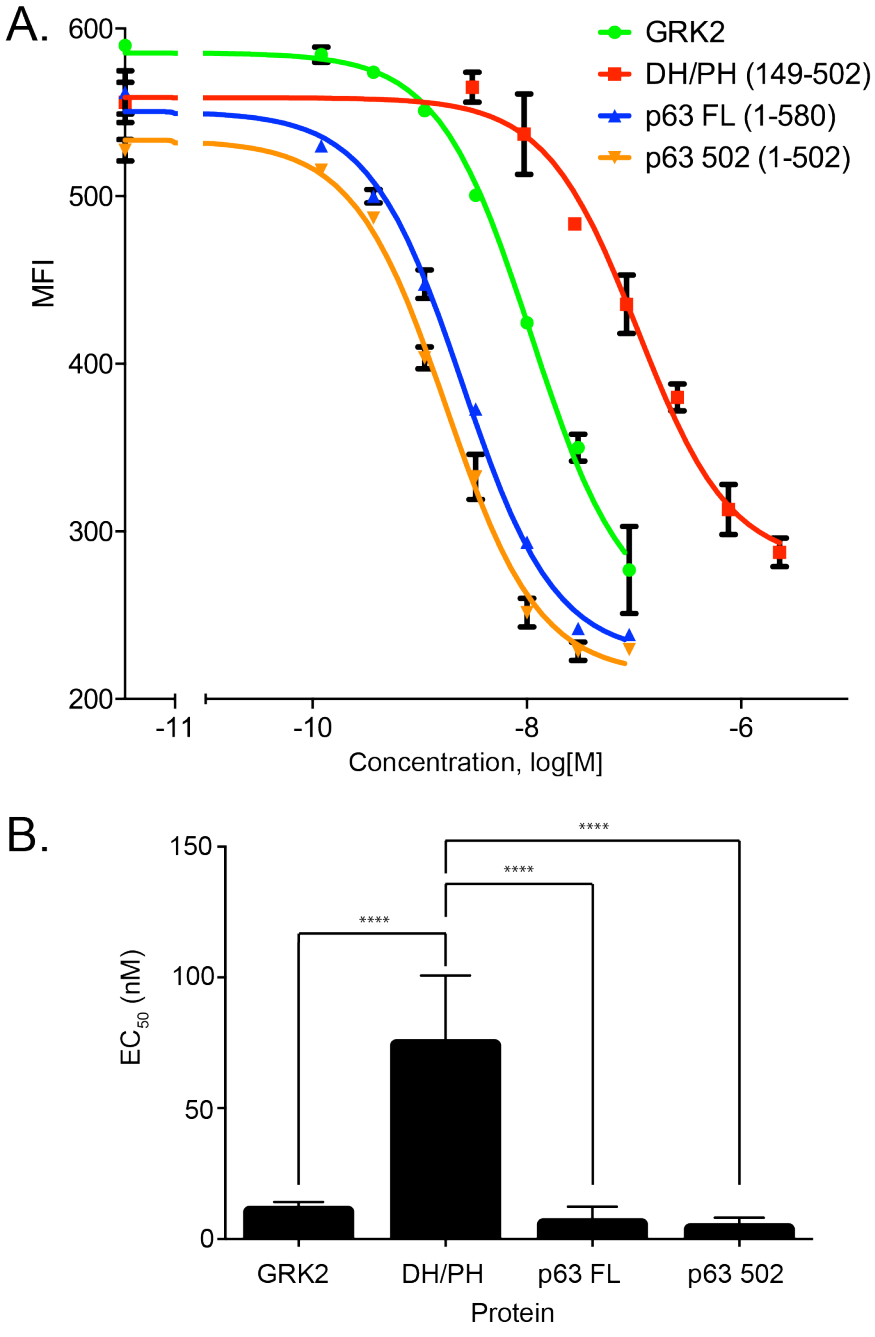

Figure C.1 Competitive binding assay using palm$^-$ p63RhoGEF variants. *A*, Unlabeled GRK2 (green), the DH/PH tandem of p63RhoGEF (red), full-length, palm$^-$ p63RhoGEF (blue), or palm$^-$, ΔC-terminus p63RhoGEF (yellow) were used to compete fluorescently labeled GRK2 off of immobilized $G\alpha_q$. *B*, EC_{50} values calculated from competitive binding assay. Error bars represent standard deviation of the mean. Statistical significance calculated in Prism by ordinary one-way ANOVA and Tukey's multiple comparisons test. P****< 0.0001.

From this work, it appears that an element in the region of residues 1-148 of p63RhoGEF is able to increase the binding affinity for $G\alpha_q$. This element also appears to interact with $G\alpha_q$ between residues 35-359. One future direction of this project could include the addition of the N-terminus of p63RhoGEF as a peptide to $G\alpha_q$ in a binding assay. If binding is observed, particularly with a dose-response, then this would further support that the increased binding affinity is not an artifact. Binding with $G\alpha_i$ could also be tested. Specificity for $G\alpha_q$ could be demonstrated if the N-terminus of p63RhoGEF does not show binding to $G\alpha_I$, and this would further support that this increased binding is not a non-specific artifact.

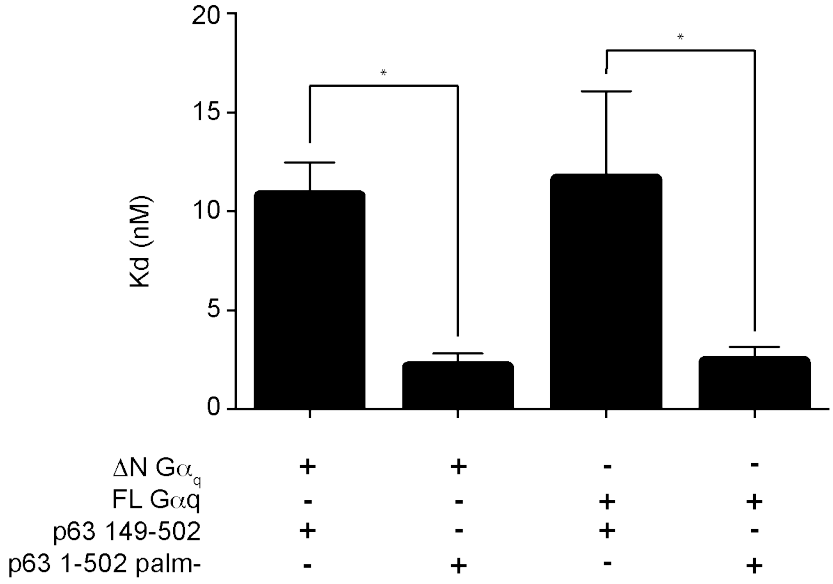

Figure C.2 Direct binding between $G\alpha_q$ and p63RhoGEF variants. Either ΔN $G\alpha_q$ (residues 35-359) or FL $G\alpha_q$ (residues 7-359) were bound to p63RhoGEF DH/PH (residues 149-502) or p63RhoGEF palm- (residues 1-502). Error bars represent standard deviation of the mean. Statistical significance calculated in Prism by ordinary one-way ANOVA and Tukey's multiple comparisons test. P* ≤ 0.05.

References

1. Siderovski, D. P., and Willard, F. S. (2005) The GAPs, GEFs, and GDIs of heterotrimeric G-protein alpha subunits. *Int. J. Biol. Sci.* **1**, 51–66
2. Lipatova, Z., Hain, A. U., Nazarko, V. Y., and Segev, N. (2015) Ypt/Rab GTPases: Principles learned from yeast. *Critical Reviews in Biochemistry and Molecular Biology*. **50**, 203–211
3. Maracci, C., and Rodnina, M. V. (2016) Review: Translational GTPases. *Biopolymers*. **105**, 463–475
4. Scarfone, I., and Piatti, S. (2015) Coupling spindle position with mitotic exit in budding yeast: The multifaceted role of the small GTPase Tem1. *Small GTPases*. **6**, 1–6
5. Rossman, K. L., Der, C. J., and Sondek, J. (2005) GEF means go: turning on RHO GTPases with guanine nucleotide-exchange factors. *Nat. Rev. Mol. Cell Biol.* **6**, 167–180
6. Sahai, E., and Marshall, C. J. (2002) RHO-GTPases and cancer. *Nat. Rev. Cancer*. **2**, 133–142
7. Loirand, G., Sauzeau, V., and Pacaud, P. (2013) Small G proteins in the cardiovascular system: physiological and pathological aspects. *Physiol. Rev.* **93**, 1659–1720
8. Govek, E.-E., Newey, S. E., and Van Aelst, L. (2005) The role of the Rho GTPases in neuronal development. *Genes Dev.* **19**, 1–49
9. Sprang, S. R. (1997) G protein mechanisms: insights from structural analysis. *Annu. Rev. Biochem.* **66**, 639–678
10. Sprang, S. R. (2016) Invited review: Activation of G proteins by GTP and the mechanism of Gα-catalyzed GTP hydrolysis. *Biopolymers*. **105**, 449–462
11. Li, G., and Zhang, X. C. (2004) GTP hydrolysis mechanism of Ras-like GTPases. *Journal of Molecular Biology*. **340**, 921–932
12. Gadea, G., and Blangy, A. (2014) Dock-family exchange factors in cell migration and disease. *Eur. J. Cell Biol.* **93**, 466–477
13. Ron, D., Tronick, S. R., Aaronson, S. A., and Eva, A. (1988) Molecular cloning and characterization of the human dbl proto-oncogene: evidence that its overexpression is sufficient to transform NIH/3T3 cells. *EMBO J.* **7**, 2465–2473
14. Aittaleb, M., Boguth, C. A., and Tesmer, J. J. G. (2010) Structure and function of heterotrimeric G protein-regulated Rho guanine nucleotide exchange factors. *Mol. Pharmacol.* **77**, 111–125
15. Kobilka, B. K. (2007) G protein coupled receptor structure and activation. *Biochim. Biophys. Acta*. **1768**, 794–807
16. Salon, J. A., Lodowski, D. T., and Palczewski, K. (2011) The significance of G protein-coupled receptor crystallography for drug discovery. *Pharmacol. Rev.* **63**, 901–937
17. Reiter, E., and Lefkowitz, R. J. (2006) GRKs and beta-arrestins: roles in receptor silencing, trafficking and signaling. *Trends Endocrinol. Metab.* **17**, 159–165
18. Wall, M. A., Coleman, D. E., Lee, E., Iñiguez-Lluhi, J. A., Posner, B. A., Gilman, A. G., and Sprang, S. R. (1995) The structure of the G protein heterotrimer Giα1β1γ2. *Cell*. **83**,

1047–1058
19. Vögler, O., Barceló, J. M., Ribas, C., and Escribá, P. V. (2008) Membrane interactions of G proteins and other related proteins. *Biochim. Biophys. Acta*. **1778**, 1640–1652
20. Dror, R. O., Mildorf, T. J., Hilger, D., Manglik, A., Borhani, D. W., Arlow, D. H., Philippsen, A., Villanueva, N., Yang, Z., Lerch, M. T., Hubbell, W. L., Kobilka, B. K., Sunahara, R. K., and Shaw, D. E. (2015) Structural basis for nucleotide exchange in heterotrimeric G proteins. *Science*. **348**, 1361–1365
21. Sprang, S. R., Chen, Z., and Du, X. (2007) Structural basis of effector regulation and signal termination in heterotrimeric Galpha proteins. *Adv. Protein Chem.* **74**, 1–65
22. Higashijima, T., Ferguson, K. M., Sternweis, P. C., Smigel, M. D., and Gilman, A. G. (1987) Effects of Mg2+ and the beta gamma-subunit complex on the interactions of guanine nucleotides with G proteins. *J. Biol. Chem.* **262**, 762–766
23. Wall, M. A., Posner, B. A., and Sprang, S. R. (1998) Structural basis of activity and subunit recognition in G protein heterotrimers. *Structure/Folding and Design*. **6**, 1169–1183
24. Gilman, A. G. (1987) G proteins: transducers of receptor-generated signals. *Annu. Rev. Biochem.*
25. Kozasa, T., Jiang, X., Hart, M. J., Sternweis, P. M., Singer, W. D., Gilman, A. G., Bollag, G., and Sternweis, P. C. (1998) p115 RhoGEF, a GTPase activating protein for Galpha12 and Galpha13. *Science*. **280**, 2109–2111
26. Chidiac, P., and Ross, E. M. (1999) Phospholipase C-beta1 directly accelerates GTP hydrolysis by Galphaq and acceleration is inhibited by Gbeta gamma subunits. *J. Biol. Chem.* **274**, 19639–19643
27. Ross, E. M., and Wilkie, T. M. (2000) GTPase-activating proteins for heterotrimeric G proteins: regulators of G protein signaling (RGS) and RGS-like proteins. *Annu. Rev. Biochem.* **69**, 795–827
28. Bodmann, E.-L., Rinne, A., Brandt, D., Lutz, S., Wieland, T., Grosse, R., and Bünemann, M. (2014) Dynamics of Gαq-protein-p63RhoGEF interaction and its regulation by RGS2. *Biochem. J.* **458**, 131–140
29. Shankaranarayanan, A., Thal, D. M., Tesmer, V. M., Roman, D. L., Neubig, R. R., Kozasa, T., and Tesmer, J. J. G. (2008) Assembly of high order G alpha q-effector complexes with RGS proteins. *J. Biol. Chem.* **283**, 34923–34934
30. Trahey, M., and McCormick, F. (1987) A cytoplasmic protein stimulates normal N-ras p21 GTPase, but does not affect oncogenic mutants. *Science*. **238**, 542–545
31. Lacal, J. C., Srivastava, S. K., Anderson, P. S., and Aaronson, S. A. (1986) Ras p21 proteins with high or low GTPase activity can efficiently transform NIH3T3 cells. *Cell*. **44**, 609–617
32. Trahey, M., Milley, R. J., Cole, G. E., Innis, M., Paterson, H., Marshall, C. J., Hall, A., and McCormick, F. (1987) Biochemical and biological properties of the human N-ras p21 protein. *Mol. Cell. Biol.* **7**, 541–544
33. Arshavsky, V. Y., Antoch, M. P., Lukjanov, K. A., and Philippov, P. P. (1989) Transducin GTPase provides for rapid quenching of the cGMP cascade in rod outer segments. *FEBS Letters*. **250**, 353–356
34. Watson, N., Linder, M. E., Druey, K. M., Kehrl, J. H., and Blumer, K. J. (1996) RGS family members: GTPase-activating proteins for heterotrimeric G-protein alpha-subunits. *Nature*. **383**, 172–175

35. Dohlman, H. G., Apaniesk, D., Chen, Y., Song, J., and Nusskern, D. (1995) Inhibition of G-protein signaling by dominant gain-of-function mutations in Sst2p, a pheromone desensitization factor in Saccharomyces cerevisiae. *Mol. Cell. Biol.* **15**, 3635–3643
36. Koelle, M. R., and Horvitz, H. R. (1996) EGL-10 Regulates G Protein Signaling in the C. elegans Nervous System and Shares a Conserved Domain with Many Mammalian Proteins. *Cell*. **84**, 115–125
37. Soundararajan, M., Willard, F. S., Kimple, A. J., Turnbull, A. P., Ball, L. J., Schoch, G. A., Gileadi, C., Fedorov, O. Y., Dowler, E. F., Higman, V. A., Hutsell, S. Q., Sundström, M., Doyle, D. A., and Siderovski, D. P. (2008) Structural diversity in the RGS domain and its interaction with heterotrimeric G protein alpha-subunits. *Proc. Natl. Acad. Sci. U.S.A.* **105**, 6457–6462
38. Heximer, S. P., Srinivasa, S. P., Bernstein, L. S., Bernard, J. L., Linder, M. E., Hepler, J. R., and Blumer, K. J. (1999) G protein selectivity is a determinant of RGS2 function. *J. Biol. Chem.* **274**, 34253–34259
39. Wang, J., Ducret, A., Tu, Y., Kozasa, T., Aebersold, R., and Ross, E. M. (1998) RGSZ1, a Gz-selective RGS Protein in Brain STRUCTURE, MEMBRANE ASSOCIATION, REGULATION BY GαzPHOSPHORYLATION, AND RELATIONSHIP TO A Gz GTPase-ACTIVATING PROTEIN SUBFAMILY. *J. Biol. Chem.* **273**, 26014–26025
40. De Vries, L., Elenko, E., and Hubler, L. (1996) *GAIP is Membrane-Anchored by Palmitoylation and Interacts with the Activated (GTP-Bound) Form of Gα i Subunits on JSTOR*, Proceedings of the …, 10.1046/j.1471-4159.2000.0752103.x/full
41. Natochin, M., and Artemyev, N. O. (1998) A single mutation Asp229 --> Ser confers upon Gs alpha the ability to interact with regulators of G protein signaling. *Biochemistry*. **37**, 13776–13780
42. Tesmer, J. J., Berman, D. M., Gilman, A. G., and Sprang, S. R. (1997) Structure of RGS4 bound to AlF4--activated G(i alpha1): stabilization of the transition state for GTP hydrolysis. *Cell*. **89**, 251–261
43. Popov, S., Yu, K., Kozasa, T., and Wilkie, T. M. (1997) The regulators of G protein signaling (RGS) domains of RGS4, RGS10, and GAIP retain GTPase activating protein activity in vitro. *PNAS*. **94**, 7216–7220
44. Franklin J Moy, Pranab K Chanda, Mark I Cockett, Wade Edris, Philip G Jones, Kim Mason, Simon Semus, A., Robert Powers (2000) NMR Structure of Free RGS4 Reveals an Induced Conformational Change upon Binding Gα‡. *Biochemistry*. **39**, 7063–7073
45. Nance, M. R., Kreutz, B., Tesmer, V. M., Sterne-Marr, R., Kozasa, T., and Tesmer, J. J. G. (2013) Structural and Functional Analysis of the Regulator of G Protein Signaling 2-Ga. *Structure/Folding and Design*. **21**, 438–448
46. Kimple, A. J., Soundararajan, M., Hutsell, S. Q., Roos, A. K., Urban, D. J., Setola, V., Temple, B. R. S., Roth, B. L., Knapp, S., Willard, F. S., and Siderovski, D. P. (2009) Structural determinants of G-protein alpha subunit selectivity by regulator of G-protein signaling 2 (RGS2). *J. Biol. Chem.* **284**, 19402–19411
47. Skiba, N. P., Yang, C. S., Huang, T., Bae, H., and Hamm, H. E. (1999) The alpha-helical domain of Galphat determines specific interaction with regulator of G protein signaling 9. *J. Biol. Chem.* **274**, 8770–8778
48. Taylor, V. G., Bommarito, P. A., and Tesmer, J. J. G. (2016) Structure of the Regulator of G Protein Signaling 8 (RGS8)−Gαq Complex: Molecular Basis for Gα Selectivity. *J. Biol. Chem.* **291**, jbc.M115.712075–5145

49. Lee, E., Linder, M. E., and Gilman, A. G. (1994) Expression of G-protein alpha subunits in Escherichia coli. *Meth. Enzymol.* **237**, 146–164
50. Kleuss, C., Raw, A. S., Lee, E., Sprang, S. R., and Gilman, A. G. (1994) Mechanism of GTP hydrolysis by G-protein alpha subunits. *PNAS*. **91**, 9828–9831
51. Sievers, F., Wilm, A., Dineen, D., Gibson, T. J., Karplus, K., Li, W., Lopez, R., McWilliam, H., Remmert, M., Söding, J., Thompson, J. D., and Higgins, D. G. (2011) Fast, scalable generation of high‐quality protein multiple sequence alignments using Clustal Omega. *Molecular Systems Biology*. **7**, 539–539
52. Winn, M. D., Ballard, C. C., Cowtan, K. D., Dodson, E. J., Emsley, P., Evans, P. R., Keegan, R. M., Krissinel, E. B., Leslie, A. G. W., McCoy, A., McNicholas, S. J., Murshudov, G. N., Pannu, N. S., Potterton, E. A., Powell, H. R., Read, R. J., Vagin, A., and Wilson, K. S. (2011) Overview of the CCP4 suite and current developments. *Acta Crystallogr. D Biol. Crystallogr.* **67**, 235–242
53. Krissinel, E., and Henrick, K. (2004) Secondary-structure matching (SSM), a new tool for fast protein structure alignment in three dimensions. *Acta Crystallogr. D Biol. Crystallogr.* **60**, 2256–2268
54. Krissinel, E., and Henrick, K. (2007) Inference of Macromolecular Assemblies from Crystalline State. *Journal of Molecular Biology*. **372**, 774–797
55. Kosloff, M., Travis, A. M., Bosch, D. E., Siderovski, D. P., and Arshavsky, V. Y. (2011) Integrating energy calculations with functional assays to decipher the specificity of G protein-RGS protein interactions. *Nat. Struct. Mol. Biol.* **18**, 846–853
56. Zeng, W., Xu, X., Popov, S., Mukhopadhyay, S., Chidiac, P., Swistok, J., Danho, W., Yagaloff, K. A., Fisher, S. L., Ross, E. M., Muallem, S., and Wilkie, T. M. (1998) The N-terminal domain of RGS4 confers receptor-selective inhibition of G protein signaling. *J. Biol. Chem.* **273**, 34687–34690
57. Hague, C., Bernstein, L. S., Ramineni, S., Chen, Z., Minneman, K. P., and Hepler, J. R. (2005) Selective inhibition of alpha1A-adrenergic receptor signaling by RGS2 association with the receptor third intracellular loop. *J. Biol. Chem.* **280**, 27289–27295
58. Santhappan, R., Crowder, A. T., Gouty, S., Cox, B. M., and Côté, T. E. (2015) Mu opioid receptor activation enhances regulator of G protein signaling 4 association with the mu opioid receptor/G protein complex in a GTP‐dependent manner. *Journal of Neurochemistry*. **135**, 76–87
59. Salim, S., Sinnarajah, S., Kehrl, J. H., and Dessauer, C. W. (2003) Identification of RGS2 and type V adenylyl cyclase interaction sites. *J. Biol. Chem.* **278**, 15842–15849
60. Day, P. W., Tesmer, J. J. G., Sterne-Marr, R., Freeman, L. C., Benovic, J. L., and Wedegaertner, P. B. (2004) Characterization of the GRK2 binding site of Galphaq. *J. Biol. Chem.* **279**, 53643–53652
61. Posner, B. A., Mukhopadhyay, S., Tesmer, J. J., Gilman, A. G., and Ross, E. M. (1999) Modulation of the affinity and selectivity of RGS protein interaction with G alpha subunits by a conserved asparagine/serine residue. *Biochemistry*. **38**, 7773–7779
62. Tu, Y., Wang, J., and Ross, E. M. (1997) Inhibition of brain Gz GAP and other RGS proteins by palmitoylation of G protein alpha subunits. *Science*. **278**, 1132–1135
63. Buhl, A. M., Johnson, N. L., Dhanasekaran, N., and Johnson, G. L. (1995) G alpha 12 and G alpha 13 stimulate Rho-dependent stress fiber formation and focal adhesion assembly. *J. Biol. Chem.* **270**, 24631–24634
64. Chikumi, H., Vázquez-Prado, J., Servitja, J.-M., Miyazaki, H., and Gutkind, J. S. (2002)

Potent Activation of RhoA by Gαq and Gq-coupled Receptors. *J. Biol. Chem.* **277**, 27130–27134
65. Vogt, S., Grosse, R., Schultz, G., and Offermanns, S. (2003) Receptor-dependent RhoA activation in G12/G13-deficient cells: genetic evidence for an involvement of Gq/G11. *J. Biol. Chem.* **278**, 28743–28749
66. Rossman, K. L., Worthylake, D. K., Snyder, J. T., Siderovski, D. P., Campbell, S. L., and Sondek, J. (2002) A crystallographic view of interactions between Dbs and Cdc42: PH domain-assisted guanine nucleotide exchange. *EMBO J.* **21**, 1315–1326
67. Bellanger, J. M., Estrach, S., Schmidt, S., Briançon Marjollet, A., Zugasti, O., Fromont, S., and Debant, A. (2003) Different regulation of the Trio Dbl-Homology domains by their associated PH domains. *Biology of the Cell*. **95**, 625–634
68. Chhatriwala, M. K., Betts, L., Worthylake, D. K., and Sondek, J. (2007) The DH and PH Domains of Trio Coordinately Engage Rho GTPases for their Efficient Activation. *Journal of Molecular Biology*. **368**, 1307–1320
69. Zamanian, J. L., and Kelly, R. B. (2003) Intersectin 1L guanine nucleotide exchange activity is regulated by adjacent src homology 3 domains that are also involved in endocytosis. *Mol. Biol. Cell*. **14**, 1624–1637
70. Ahmad, K. F., and Lim, W. A. (2010) The minimal autoinhibited unit of the guanine nucleotide exchange factor intersectin. *PLoS ONE*. **5**, e11291
71. Abe, K., Whitehead, I. P., O'Bryan, J. P., and Der, C. J. (1999) Involvement of NH(2)-terminal sequences in the negative regulation of Vav signaling and transforming activity. *J. Biol. Chem.* **274**, 30410–30418
72. Aghazadeh, B., Lowry, W. E., Huang, X. Y., and Rosen, M. K. (2000) Structural basis for relief of autoinhibition of the Dbl homology domain of proto-oncogene Vav by tyrosine phosphorylation. *Cell*. **102**, 625–633
73. Yu, B., Martins, I. R. S., Li, P., Amarasinghe, G. K., Umetani, J., Fernandez-Zapico, M. E., Billadeau, D. D., Machius, M., Tomchick, D. R., and Rosen, M. K. (2010) Structural and Energetic Mechanisms of Cooperative Autoinhibition and Activation of Vav1. *Cell*. **140**, 246–256
74. Soisson, S. M., Nimnual, A. S., Uy, M., Bar-Sagi, D., and Kuriyan, J. (1998) Crystal structure of the Dbl and pleckstrin homology domains from the human Son of sevenless protein. *Cell*. **95**, 259–268
75. Jaiswal, M., Gremer, L., Dvorsky, R., Haeusler, L. C., Cirstea, I. C., Uhlenbrock, K., and Ahmadian, M. R. (2011) Mechanistic insights into specificity, activity, and regulatory elements of the regulator of G-protein signaling (RGS)-containing Rho-specific guanine nucleotide exchange factors (GEFs) p115, PDZ-RhoGEF (PRG), and leukemia-associated RhoGEF (LARG). *J. Biol. Chem.* **286**, 18202–18212
76. Salazar, M. A., Kwiatkowski, A. V., Pellegrini, L., Cestra, G., Butler, M. H., Rossman, K. L., Serna, D. M., Sondek, J., Gertler, F. B., and De Camilli, P. (2003) Tuba, a novel protein containing bin/amphiphysin/Rvs and Dbl homology domains, links dynamin to regulation of the actin cytoskeleton. *J. Biol. Chem.* **278**, 49031–49043
77. Lemmon, M. A. (2008) Membrane recognition by phospholipid-binding domains. *Nat. Rev. Mol. Cell Biol.* **9**, 99–111
78. Das, B., Shu, X., Day, G.-J., Han, J., Krishna, U. M., Falck, J. R., and Broek, D. (2000) Control of Intramolecular Interactions between the Pleckstrin Homology and Dbl Homology Domains of Vav and Sos1 Regulates Rac Binding. *J. Biol. Chem.* **275**,

15074–15081
79. Welch, H. C. E., Coadwell, W. J., Ellson, C. D., Ferguson, G. J., Andrews, S. R., Erdjument-Bromage, H., Tempst, P., Hawkins, P. T., and Stephens, L. R. (2002) P-Rex1, a PtdIns(3,4,5)P3- and Gbetagamma-regulated guanine-nucleotide exchange factor for Rac. *Cell*. **108**, 809–821
80. Souchet, M., Portales-Casamar, E., Mazurais, D., Schmidt, S., Léger, I., Javré, J.-L., Robert, P., Berrebi-Bertrand, I., Bril, A., Gout, B., Debant, A., and Calmels, T. P. G. (2002) Human p63RhoGEF, a novel RhoA-specific guanine nucleotide exchange factor, is localized in cardiac sarcomere. *J. Cell. Sci.* **115**, 629–640
81. Lutz, S., Freichel-Blomquist, A., Rümenapp, U., Schmidt, M., Jakobs, K. H., and Wieland, T. (2004) p63RhoGEF and GEFT are Rho-specific guanine nucleotide exchange factors encoded by the same gene. *Naunyn Schmiedebergs Arch. Pharmacol.* **369**, 540–546
82. Rojas, R. J., Yohe, M. E., Gershburg, S., Kawano, T., Kozasa, T., and Sondek, J. (2007) Galphaq directly activates p63RhoGEF and Trio via a conserved extension of the Dbl homology-associated pleckstrin homology domain. *J. Biol. Chem.* **282**, 29201–29210
83. Lutz, S., Shankaranarayanan, A., Coco, C., Ridilla, M., Nance, M. R., Vettel, C., Baltus, D., Evelyn, C. R., Neubig, R. R., Wieland, T., and Tesmer, J. J. G. (2007) Structure of Galphaq-p63RhoGEF-RhoA complex reveals a pathway for the activation of RhoA by GPCRs. *Science*. **318**, 1923–1927
84. Aittaleb, M., Nishimura, A., Linder, M. E., and Tesmer, J. J. G. (2011) Plasma membrane association of p63 Rho guanine nucleotide exchange factor (p63RhoGEF) is mediated by palmitoylation and is required for basal activity in cells. *J. Biol. Chem.* **286**, 34448–34456
85. Guo, X., Stafford, L. J., Bryan, B., Xia, C., Ma, W., Wu, X., Liu, D., Songyang, Z., and Liu, M. (2003) A Rac/Cdc42-specific exchange factor, GEFT, induces cell proliferation, transformation, and migration. *J. Biol. Chem.* **278**, 13207–13215
86. Goedhart, J., van Unen, J., Adjobo-Hermans, M. J. W., and Gadella, T. W. J., Jr (2013) Signaling efficiency of Gαq through its effectors p63RhoGEF and GEFT depends on their subcellular location. *Scientific Reports*. **3**, 2284
87. Debant, A., Serra-Pagès, C., Seipel, K., O'Brien, S., Tang, M., Park, S. H., and Streuli, M. (1996) The multidomain protein Trio binds the LAR transmembrane tyrosine phosphatase, contains a protein kinase domain, and has separate rac-specific and rho-specific guanine nucleotide exchange factor domains. *PNAS*. **93**, 5466–5471
88. Shankaranarayanan, A., Boguth, C. A., Lutz, S., Vettel, C., Uhlemann, F., Aittaleb, M., Wieland, T., and Tesmer, J. J. G. (2010) Galpha q allosterically activates and relieves autoinhibition of p63RhoGEF. *Cell. Signal.* **22**, 1114–1123
89. Lutz, S., Freichel-Blomquist, A., Yang, Y., Rümenapp, U., Jakobs, K. H., Schmidt, M., and Wieland, T. (2005) The guanine nucleotide exchange factor p63RhoGEF, a specific link between Gq/11-coupled receptor signaling and RhoA. *J. Biol. Chem.* **280**, 11134–11139
90. Whitehead, I. P., Lambert, Q. T., Glaven, J. A., Abe, K., Rossman, K. L., Mahon, G. M., Trzaskos, J. M., Kay, R., Campbell, S. L., and Der, C. J. (1999) Dependence of Dbl and Dbs Transformation on MEK and NF-κB Activation. *Mol. Cell. Biol.* **19**, 7759–7770
91. Gu, S., He, J., Ho, W.-T., Ramineni, S., Thal, D. M., Natesh, R., Tesmer, J. J. G., Hepler, J. R., and Heximer, S. P. (2007) Unique Hydrophobic Extension of the RGS2

Amphipathic Helix Domain Imparts Increased Plasma Membrane Binding and Function Relative to Other RGS R4/B Subfamily Members. *J. Biol. Chem.* **282**, 33064–33075
92. Weigand, S., Stillwell, B., Guise, W. E., and Quintana, J. (2009) Flexibility and high throughput: supporting SAXS users at a joint industrial academic beamline. *Adv X-Ray Anal*
93. Orthaber, D., Bergmann, A., Glatter, O., IUCr (2000) SAXS experiments on absolute scale with Kratky systems using water as a secondary standard. *J Appl Crystallogr*. **33**, 218–225
94. Petoukhov, M. V., Franke, D., Shkumatov, A. V., Tria, G., Kikhney, A. G., Gajda, M., Gorba, C., Mertens, H. D. T., Konarev, P. V., and Svergun, D. I. (2012) New developments in the ATSAS program package for small-angle scattering data analysis. *J Appl Crystallogr*. **45**, 342–350
95. Svergun, D. I. (1992) Determination of the regularization parameter in indirect-transform methods using perceptual criteria. *J Appl Crystallogr*
96. Mylonas, E., and Svergun, D. I. (2007) Accuracy of molecular mass determination of proteins in solution by small-angle X-ray scattering. *J Appl Crystallogr*
97. Svergun, D. I., Petoukhov, M. V., and Koch, M. H. J. (2001) Determination of Domain Structure of Proteins from X-Ray Solution Scattering. *Biophysical Journal*. **80**, 2946–2953
98. Volkov, V. V., and Svergun, D. I. (2003) Uniqueness of ab initio shape determination in small-angle scattering. *J Appl Crystallogr*
99. Pettersen, E. F., Goddard, T. D., Huang, C. C., Couch, G. S., Greenblatt, D. M., Meng, E. C., and Ferrin, T. E. (2004) UCSF Chimera—A visualization system for exploratory research and analysis. *Journal of Computational Chemistry*. **25**, 1605–1612
100. Delaglio, F., Grzesiek, S., Vuister, G. W., Zhu, G., Pfeifer, J., and Bax, A. (1995) NMRPipe: A multidimensional spectral processing system based on UNIX pipes. *J. Biomol. NMR*. **6**, 277–293
101. Cierpicki, T., and Bushweller, J. H. (2004) Charged gels as orienting media for measurement of residual dipolar couplings in soluble and integral membrane proteins. *J. Am. Chem. Soc.* **126**, 16259–16266
102. Cierpicki, T., Bielnicki, J., Zheng, M., Gruszczyk, J., Kasterka, M., Petoukhov, M., Zhang, A., Fernandez, E. J., Svergun, D. I., Derewenda, U., Bushweller, J. H., and Derewenda, Z. S. (2009) The solution structure and dynamics of the DH-PH module of PDZRhoGEF in isolation and in complex with nucleotide-free RhoA. *Protein Sci.* **18**, 2067–2079
103. Snyder, J. T., Worthylake, D. K., Rossman, K. L., Betts, L., Pruitt, W. M., Siderovski, D. P., Der, C. J., and Sondek, J. (2002) Structural basis for the selective activation of Rho GTPases by Dbl exchange factors. *Nat. Struct. Biol.* **9**, 468–475
104. Chen, V. B., Arendall, W. B., Headd, J. J., Keedy, D. A., Immormino, R. M., Kapral, G. J., Murray, L. W., Richardson, J. S., and Richardson, D. C. (2009) MolProbity: all-atom structure validation for macromolecular crystallography. *Acta Cryst (2010). D66, 12-21 [doi:10.1107/S0907444909042073]*. **66**, 1–10
105. Case, D. A., Darden, T. A., Cheatham, T. E., III, Simmerling, C. L., Wang, J., Duke, R. E., Luo, R., Walker, R. C., Zhang, W., Merz, K. M., Roberts, B., Hayik, S., Roitberg, A., Seabra, G., Swails, J., Götz, A. W., Kolossváry, I., Wong, K. F., Paesani, F., Vanicek, J., Wolf, R. M., Liu, J., Wu, X., Brozell, S. R., Steinbrecher, T., Gohlke, H., Cai, Q., Ye,

X., Hsieh, M. J., Cui, G., Roe, D. R., Mathews, D. H., Seetin, M. G., Salomon-Ferrer, R., Sagui, C., Babin, V., Luchko, T., Gusarov, S., Kovalenko, A., and Kollman, P. A. (2012) *AMBER 12*, University of California, San Francisco

106. Onufriev, A., Bashford, D., and Case, D. A. (2004) Exploring protein native states and large-scale conformational changes with a modified generalized born model. *Proteins: Structure, Function, and Bioinformatics*. **55**, 383–394
107. Anandakrishnan, R., Drozdetski, A., Walker, R. C., and Onufriev, A. V. (2015) Speed of Conformational Change: Comparing Explicit and Implicit Solvent Molecular Dynamics Simulations. *Biophysical Journal*. **108**, 1153–1164
108. Götz, A. W., Williamson, M. J., Xu, D., Poole, D., Le Grand, S., and Walker, R. C. (2012) Routine Microsecond Molecular Dynamics Simulations with AMBER on GPUs. 1. Generalized Born. *Journal of chemical …*. **8**, 1542–1555
109. Salomon-Ferrer, R., Götz, A. W., Poole, D., Le Grand, S., and Walker, R. C. (2013) Routine Microsecond Molecular Dynamics Simulations with AMBER on GPUs. 2. Explicit Solvent Particle Mesh Ewald. *Journal of chemical …*. **9**, 3878–3888
110. Williams, S. L., Lutz, S., Charlie, N. K., Vettel, C., Ailion, M., Coco, C., Tesmer, J. J. G., Jorgensen, E. M., Wieland, T., and Miller, K. G. (2007) Trio's Rho-specific GEF domain is the missing Galpha q effector in C. elegans. *Genes Dev.* **21**, 2731–2746
111. Ingi, T., Krumins, A. M., Chidiac, P., Brothers, G. M., Chung, S., Snow, B. E., Barnes, C. A., Lanahan, A. A., Siderovski, D. P., Ross, E. M., Gilman, A. G., and Worley, P. F. (1998) Dynamic regulation of RGS2 suggests a novel mechanism in G-protein signaling and neuronal plasticity. *J. Neurosci.* **18**, 7178–7188
112. Cladman, W., and Chidiac, P. (2002) Characterization and comparison of RGS2 and RGS4 as GTPase-activating proteins for m2 muscarinic receptor-stimulated G(i). *Mol. Pharmacol.* **62**, 654–659
113. Wieland, T., and Mittmann, C. (2003) Regulators of G-protein signalling: multifunctional proteins with impact on signalling in the cardiovascular system. *Pharmacol. Ther.* **97**, 95–115
114. Berjanskii, M. V., and Wishart, D. S. (2005) A simple method to predict protein flexibility using secondary chemical shifts. *J. Am. Chem. Soc.* **127**, 14970–14971
115. Berjanskii, M. V., and Wishart, D. S. (2007) The RCI server: rapid and accurate calculation of protein flexibility using chemical shifts. *Nucleic Acids Res.* **35**, W531–7
116. Yeung, W. W. S., and Wong, Y. H. (2009) The RhoA-specific guanine nucleotide exchange factor p63RhoGEF binds to activated Galpha(16) and inhibits the canonical phospholipase Cbeta pathway. *Cell. Signal.* **21**, 1317–1325
117. Wu, B., Zhang, Z., Noberini, R., Barile, E., Giulianotti, M., Pinilla, C., Houghten, R. A., Pasquale, E. B., and Pellecchia, M. (2013) HTS by NMR of combinatorial libraries: a fragment-based approach to ligand discovery. *Chem. Biol.* **20**, 19–33
118. Betz, M., Saxena, K., and Schwalbe, H. (2006) Biomolecular NMR: a chaperone to drug discovery. *Curr Opin Chem Biol*. **10**, 219–225
119. Calò, L. A., Davis, P. A., Pagnin, E., Dal Maso, L., Maiolino, G., Seccia, T. M., Pessina, A. C., and Rossi, G. P. (2014) Increased level of p63RhoGEF and RhoA/Rho kinase activity in hypertensive patients. *Journal of Hypertension*. **32**, 331–338
120. Ravarotto, V., Pagnin, E., Maiolino, G., Fragasso, A., Carraro, G., Rossi, B., and Calò, L. A. (2015) The blocking of angiotensin II type 1 receptor and RhoA/Rho kinase activity in hypertensive patients: Effect of olmesartan medoxomil and implication with

cardiovascular-renal remodeling. *Journal of Renin-Angiotensin-Aldosterone System*. **16**, 1245–1250

121. García-Mata, R., and Burridge, K. (2007) Catching a GEF by its tail. *Trends Cell Biol.* **17**, 36–43

122. Blazer, L. L., Roman, D. L., Muxlow, M. R., and Neubig, R. R. (2010) *Use of Flow Cytometric Methods to Quantify Protein-Protein Interactions*, John Wiley & Sons, Inc., Hoboken, NJ, USA, 10.1002/0471142956.cy1311s51